Queen Mary University of London

Application of global and regional myocardial deformation using cardiovascular magnetic resonance: an assessment of feature tracking *in vivo* and using numerical simulation

Haifa Matar H Almutairi, MSc

Supervisors: Prof. S E Petersen, Dr. M E Miquel M and Dr. R Boubertakh

Thesis submitted for the degree of Doctor of Philosophy University of London December, 2017

Centre for Advanced Cardiovascular Imaging NIHR Cardiovascular Biomedical Research Unit at Bart's William Harvey Research Institute Queen Mary University of London

Table of Contents

Declaration

This work has not previously been accepted in substance for any degree and is not being concurrently submitted in candidature for any degree.

Signed ..... (candidate)
Date .....

STATEMENT 1
This thesis is the result of my own investigations, except where otherwise stated. Other sources are acknowledged by giving explicit references. A bibliography is appended.

Signed ..... (candidate)
Date .....

Abstract

Cardiovascular diseases are responsible for approximately a third of all death worldwide, with hypertension being a major risk factor for many of those. Hypertension can lead to left ventricle hypertrophy and diastolic and systolic dysfunction. Myocardial deformation parameters have been shown to have high sensitivity at the early stage of contractile dysfunction. They can be derived from myocardial tagging, considered to be the gold-standard method, or from routinely acquired cine images using feature tracking (FT) techniques.

This work aimed to validate FT as a post processing technique. Three FT software packages were used to measure strain parameters in healthy subjects and hypertensive patients in order to assess agreement. Intra- and inter-observer reproducibility was also investigated. The CVI42 software was found to have the best reproducibility. Good agreement across the three software packages and both groups was also observed for circumferential strain calculated from mid-ventricle short axis and longitudinal strain parameters. CVI42 was also compared to the reference tagging analysis by applying both techniques to a healthy and hypertensive patient cohort. Although tagging could discriminate between the two populations (longitudinal strain), no statistically significant differences were found by CVI42. The final validation step was to generate simulation models mimicking simplified cardiac views to compare the experimental results against a true gold-standard for which strain values are known. Two commercial FT software packages were used to analyze the simulated cine images with increasing complexity levels. Both showed inaccurate tracking and high errors compared to analytical values. This indicated that more realistic and complex numerical models should be investigated.

Although FT is a relatively new and promising technique, the results demonstrated that it still requires going through standardization to better understand inter-vendor variability.

Acknowledgments

I am indebted to my supervisors, Professor Steffen Petersen, Dr. Marc Miquel and Dr. Redha Boubertakh for their constructive critiques, encouragement and invaluable support during the course of this thesis. The time they spent helping me to develop quality research skills meant a lot and was highly beneficial during the entire duration of the programme.

I would like to thank my colleagues Filip Zemrak and Mohammed Kanji for providing me with patients' data that was helpful when carrying out my study on CMR image analysis. I would also like to thank Jackie Cooper, the statistician at our centre, for her advice on statistics.

Thanks must go to all my colleagues in the Advanced Cardiovascular Imaging Unit at the William Harvey Heart Centre, who all contributed to my research in many ways.

Special thanks go to the government of Saudi Arabia, who provided me with this valuable opportunity to expand my academic knowledge by undertaking a novel doctorate research degree in cardiac magnetic resonance imaging. Their ongoing support is helping to overcome the difficulties faced by Saudi female citizens. Today, as Saudi women, we all are keen to prove that we deserve to be first-class citizens, equal to men, and with full citizenship rights. As part of my personal commitment, the benefits of my studies will be utilised towards national development.

Finally, very special thanks to my father's soul Matar and my mother Ezwa, who surrounded me with their care and unconditional love and expressed their strong belief in me; their prayers will continue to influence my life. I hope to keep making them proud every day of my life. Special thanks to my sons Faisal and Bandar for their patience and love; they are the main reason I shall carry on with my research to make them proud of me as I'm proud of them. They are the candles in my life, who light my way to a brighter future. They were my strength when I was weak and my happiness when I was sad; how could I carry on living without them? Thanks to all my family members, who always make me feel that there are loving people in my life, who care so much for me.

Collaborations

- Dr Filip Zemrak provided 26 hypertensive patients data in chapter 5.
- Dr Mohammed Khanji provided data from the HAPPY London project

Publications

Conferences

1- A comparison of cardiac motion analysis software packages: application to left ventricular deformation analysis in hypertensive patients. Haifa M Almutairi, Filip Zemrak, Thomas A Treibel, Daniel Sado, Redha Boubertakh, Marc E Miquel, and Steffen E Petersen. Poster presentation, *European Society of Cardiology (EuroCMR) and Society of Cardiovascular Magnetic Resonance* (SCMR) 18th Annual Scientific Session, joint scientific session in February 2015. Nice, France.

2- A comparison of cardiac motion analysis software packages: application to left ventricular deformation analysis in healthy subjects. Haifa M Almutairi, Mohammed Y Khanji, Redha Boubertakh, Marc E Miquel, Steffen E Petersen. Poster presentation, *Society of cardiovascular magnetic resonance* (SCMR) 19th Annual Scientific Session in January 2016, Los Angeles, CA, USA

3- A comparison of cardiac motion analysis software packages: application to left ventricular deformation analysis in hypertensive patients. Haifa M Almutairi, Mohammed Y Khanji, Redha Boubertakh, Marc E Miquel, Steffen E Petersen. Accepted for oral presentation at *European Society of Cardiology*, Florence, Italy, May 2016

Review article

Myocardial deformation assessment using cardiovascular magnetic resonance-feature tracking technique. Haifa M Almutairi, Redha Boubertakh, Marc E Miquel and Steffen E Petersen. 90 (1080) pp: 20170072 (2017)

List of Acronyms

FT	Feature tracking
CMR	Cardiac Magnetic Resonance
MRI	Magnetic Resonance Imaging
ECG	Electrocardiography
LVH	Left ventricle hypertrophy
NMR	Nuclear magnetic resonance
RF	Radio frequency
B_0	Static magnetic field
B_1	Excitation pulse
FID	Free induction decay
T_1	Relaxation time
T_2	Spin-spin relaxation
TE	Echo time
TR	Repetition time
ESV	End systolic volume
EDV	End diastolic volume
SV	Stroke volume
EF	Ejection Fraction (EF)
GRE	Gradient echo
bSFFP	Balance steady state free precession
SNR	Signal to noise
RO	Readout
PE	Phase encoding
SS	Slice selection

CVD	Cardiovascular disease
2D	Two dimension
3D	Three dimension
SR	Strain rate
RV	Right ventricle
LV	Left ventricle
LA	Left atrial
COA	Coarctation of the aorta
CV	Coefficient of variation
DMD	Duchenne muscular dystrophy
AS	Aortic Stenosis
TOF	Tetralogy of Fallot
STE	Speckle tracking echocardiography
2DE	2D Echocardiography analysis
CS	Circumferential strain
RS	Radial strain
LS	Longitudinal strain
CSR	Circumferential strain rate
GRS	Global radial strain
GLS	Global longitudinal strain
SCS	Systolic circumferential strain
VLX	Vertical long axis
HLA	Horizontal long axis
ICC	Intra-class correlation
SD	Standard deviation
IQR	Interquartile range

Endo	Endocardial
Epi	Epicardial,
SAX	Short axis
LAX	Long axis
2ch	2-chamber
4ch	4-chamber
NA	Not available
ND	Not defined
BMI	Body mass index
BSA	Body surface area
BP	Blood pressure
EF	Left ventricle ejection fraction
PCA	Principal components analysis
ROC	Receiver operating characteristic
CSPAMM	Spatial modulation of magnetization
CSPAMM	Complementary spatial modulation of magnetization
EACVI	European Association of Cardiovascular Imaging
ASE	American Society of Echocardiography

List of Tables

List of Figures

Chapter 1: Thesis Overview

1.1 Thesis objectives

There is an increased understanding that myocardial deformation parameters have the capability of detecting early contractile dysfunction in a number of cardiovascular diseases (1)(2). Feature tracking (FT) is a promising post-processing technique introduced recently to derive myocardial deformation parameters (3). FT relies on the analysis of routinely acquired functional Cardiac Magnetic Resonance (CMR) images to calculate these regional deformation parameters. This technique is time effective and a number of commercial and research software packages are available, making it a potential clinical tool.

An increasing numbers of studies using FT are published and the ability of deformation parameters to distinguish between healthy subjects and cardiovascular disease patients has been demonstrated (4)(5). However, high variability and low reproducibility has been reported for some deformation parameters when measured by different FT software (6)(7).

To fully harvest the clinical potential of FT, it is necessary to ensure that software packages are reproducible in the measurements they produce and that inter-vendor variability is investigated. Ideally, the results should be compared to current clinical gold standards and/or ground truth numerical simulations.

The aims of this PhD is to assess inter-vendor agreement and the quality of the measurement produced by commercially available and research FT software packages.

This is first achieved by comparing global and regional deformation parameters derived from the FT packages in healthy and patient populations. As Magnetic Resonance Imaging (MRI) tagging is an established method to obtain myocardial deformation parameters (8), FT packages are compared to tagging in healthy and hypertensive patients. The final aim is to develop ground truth simulation models and compare FT packages using those models.

1.2 Thesis plan

This thesis contains a further seven chapters. The **second chapter** provides brief background information on cardiac anatomy and physiology and the necessary information to understand how the CMR images, used in the subsequent chapters, are acquired. The **third chapter** is an introduction to FT and a comprehensive review of articles using or validating FT published to date. It should give the reader a clear understanding of the key findings, the advantages, disadvantages and limitations of studies published in this field. The review focusses on applications of feature tracking to both healthy subjects and cardiovascular disease patients. It also includes comparative studies with tagging technique or echocardiography. This chapter clearly highlights the lack of validation studies, either using *in-vivo* data or computer simulation. Furthermore, it also demonstrates the need for standardization of the parameters if they are to be used as viable indices to guide clinical decisions. The **fourth chapter** describes the common methods used in comparing global and regional deformation parameters derived from different software packages as well as outlining in detail the approaches of different software package used in the remainder of the dissertation. Descriptive information regarding the type and choice of statistical tests used to assess the agreement and reproducibility of feature tracking software packages are exhaustively discussed. The next

three chapters are designed to address some of the validation issues highlighted by chapter 3. In **chapter 5,** three FT packages are compared using data from 26 hypertensive patients and 28 healthy subjects. Both global and regional deformation parameters are calculated from functional CMR images. Further to the software packages comparison, the reproducibility of the three FT software packages was also investigated by assessing the inter-observer and intra-observer variability. To extend the comparison to a healthy population, and compare FT against the established tagging method, data from the HAPPY London study (9), are analysed in **chapter six.** In addition, the correlation between deformation parameters with diastolic and systolic blood pressure is evaluated. The differences between global and regional deformation parameters relevant to gender and hypertension are also assessed. The clear differences between software found in both chapter 5 and 6 justified the need for a ground truth numerical phantom. In **chapter seven,** five short and long axis simulations models of increasing complexity are designed; uniform short and long axis models, radial short and long axis models and finally a checkerboard short axis model. The five models are analyzed using two commercial FT software packages and results compared to the known theoretical values that are calculable using theoretical motion and deformation equations. Finally, **chapter eight** summarises the major findings of the entire thesis, discusses its limitations and highlights possible areas of for further research.

Chapter 2: Cardiac Magnetic Resonance Imaging

2.1 Introduction

The feature tacking methodology studied in this thesis makes use of cardiac magnetic resonance (CMR) images. Consequently, this chapter provides the reader with background information on how such images are acquired. It is by no means a detailed account of cardiac MRI physics and the interested reader can find more details for example in references (10)(11)(12).

Unlike most other organs that are “static”, cardiac imaging has first to deal with cardiac motion. This is most commonly achieved by using an ECG trigger. Consequently, the first part of this chapter introduces succinctly cardiac anatomy and physiology. Once again the interested reader can find more details in (13)(14).

2.2 Cardiac Anatomy

The heart is a muscular organ weighing about 300g with its size likened to a human fist, and it is located within the middle and left of the mediastinum. The human heart is surrounded and protected by a double-membraned sac known as the pericardium sac.

The heart is cone-shaped and tilted forward to the left. The tip of the cone is called apex of the heart, at the bottom, the apex lies to the left of the midline of the heart. The top of the human heart is known as the base, where the great vessels enter the heart and lies posterior to the sternum as shown in (Figure 2.1). The human heart is divided into four

chambers namely, upper left and right atria; and lower left and right ventricle. The right atrium and ventricle are often grouped as the right heart while the left atrium and ventricle are also referred to left heart (14). The two smaller atria are located at the base of the heart, whereas, the two larger ventricles are located at the apex. Fibrous tissue separates the atria from the ventricles and within these tissues are the four cardiac valves are located. A muscular septum separates the right heart from the left heart.

The heart is also composed of valves, which prevent back flow of blood through the chambers. Between the right atrium and ventricle is the tricuspid valve while the bicuspid valve is located between the left atrium and left ventricle. The wall of the heart contains three layers of muscle; the innermost endocardial tissue, which is the thick myocardial layer, and outer pericardium, that covered in fibrous layer, to the pericardium. The innermost layer of the endocardium has a lining of endothelial cells which represents the thin endocardial layer. The outer epicardial surface contains the major coronary blood vessels and is separated from the pericardium by a thin layer of fluid (15).

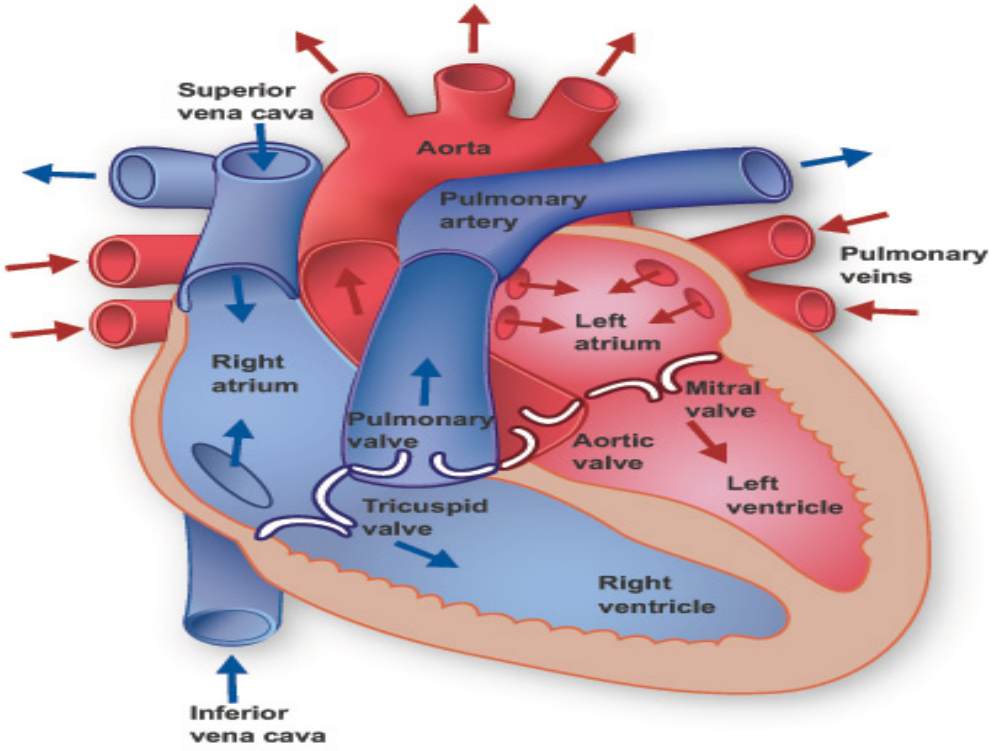

Figure 2.1: Anterior view of the heart showing the anatomical features (16).

2.3 Cardiac Cycle

The cardiac motion is a periodic contraction and relaxation of the cardiac muscles to pump blood out of the ventricles into the circulatory system (13). The cardiac cycle is composed of systole (contraction and ejection) and diastolic (relaxation and filling) phases and since the human heart is comprised of four chambers, the cycle consists of atrial systole, atrial diastole, ventricular systole and ventricular diastole (17).

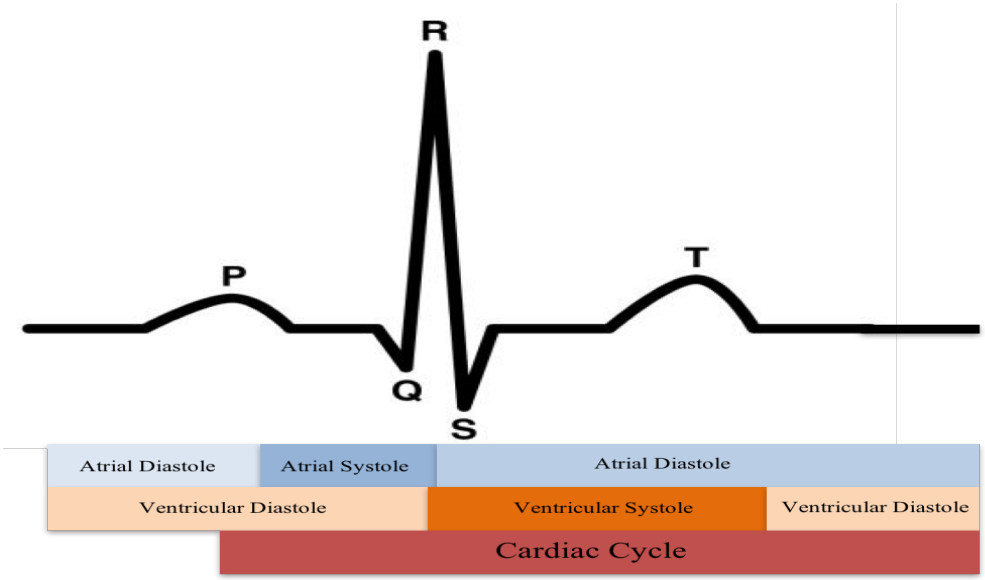

Figure 2.2: Relationship between the cardiac cycle and ECG: At first there is atria and ventricular relaxation (diastole). Atria contraction (systole) immediately follows depolarisation of the atruim as represented by the P-wave in the ECG and continues until the QRS- complex starts, with the atrium now undergoing relaxation. The QRS-complex represents ventricular depolaristaion closely followed by ventricular contraction (systole). Repolarisation of the ventricles marks the start of ventricular relaxation and is represented by the T-wave in the ECG.

Atrial Systole and Diastole: This phase involves the atrial muscles contraction and pressure rise within the atria leading to the pumping of blood into the ventricles through the open tricuspid and bicuspid valves. Atrial systole ends prior to ventricular systole, as the atrial muscle returns to diastole.

Ventricular Systole: In this phase, there is rapid ventricle contraction also known as

(ventricular systole). At first ventricular blood pressure increases as the muscles within the ventricle contracts leading to rise in the blood pressure within the chamber, the blood pressure quickly builds up above the atria which are undergoing relaxation in the diastolic phase at that time. This increase in blood pressure results in backward flow of blood towards the atria, causing the tricuspid and mitral valves to close. The ventricular systole begins to increase pressure within the ventricle to a threshold required to open the semilunar valves. This leads to pumping of blood from the ventricles of the heart into systemic circulation by pushing open the pulmonary and aortic semilunar valves. (15)(18).

Ventricular Diastole: In this phase, the muscles of the ventricles undergo relaxation, pressure within the remaining blood in the chamber begins to drop. A fall in ventricular pressure below the pressure in both pulmonary trunk and aorta leads to back flow of blood towards the heart leading to closure of the semilunar valves and prevents blood from going into system circulation. Following ventricular muscle relaxation, blood pressure within the ventricles drop even further. It gets to a point where it drops below the atrial pressure leading flow of blood from atria into the ventricles pushing open the mitral and tricuspid valve. Further drop in pressure within the ventricle leads to flow of blood from the major veins into the relaxed atria and subsequently into the ventricles. At this stage when both chambers are in diastole, the atrioventricular valves are open and the semilunar valves are closed marks the complete phase of the cardiac cycle (15).

Different cardiac views in this thesis were used including three short axis views (basal, mid-ventricle, apical) as well as two-chamber and four chamber views as shown in Figure 2.3.

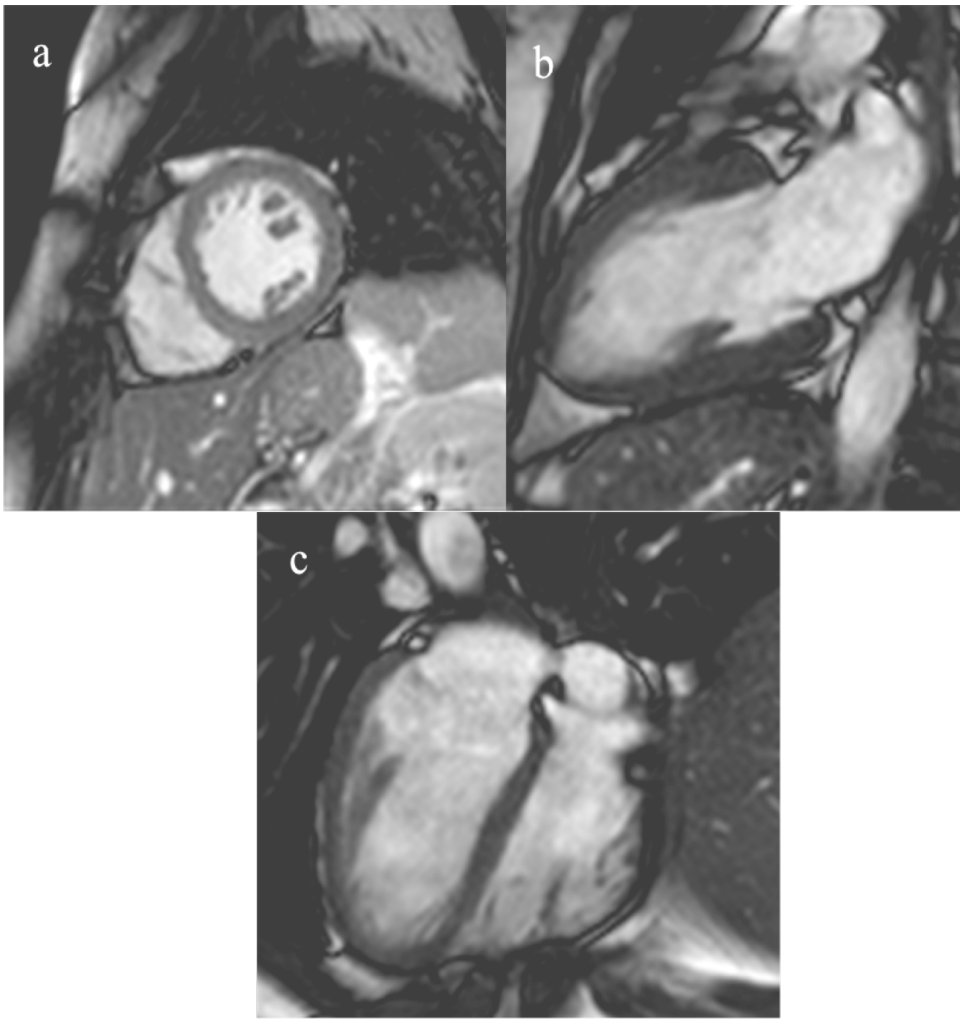

Figure 2.3: Typical SSFP images for mid-ventricle short axis view (a), two-chamber long axis view (b) and four-chamber long axis view (c).

2.3 Hypertension

Hypertension is a major growing public health concern since it affects more than 1 billion people worldwide every year (19). Hypertension is an important risk factor for numerous cardiac diseases and the consequences of hypertension includes myocardial infarction, strokes, heart failure and coronary heart disease (19)(20). Hypertension accounts for increase incidents of global death (21). The relationship between blood pressure and its resultant complications is linear over a wide range of blood pressure, and there seems to be no clear threshold for the increased risk (22). The risk of complications in healthy

subjects as a result of high blood pressures require both researchers and clinicians to lay more emphasis on how to prevent or manage hypertensive conditions, hence early detection, treatment, and control of this condition should be prioritised (20). Hypertension is defined as over 140/90 mmHg as the systolic blood pressure is >140 mmHg or the diastolic blood pressure is > 90 mmHg (23). Spiking blood pressure consistently increase the risk of developing hypertensive cardiovascular diseases however, hypertension occurs when the blood pressure in the arteries is persistently raised.

2.3.1 Effects on heart structure (remodelling):

The structure of the heart is easily influenced by pressure and volume loads (21). Clinically diagnosed hypertensive heart disease are often characterised by changes in myocardial structure such as the more common left ventricular hypertrophy. At the onset of hypertension, the heart tries to overcome the increased afterload by the left ventricle induced by neurohormornal activation (24). This initially will lead to compensation (myocardial wall stress and enlargement) to deal with the pressure. However, persistent afterload and more neurohormonal activation eventually lead to progressive loss of cardiac muscle (adverse remodelling). At this stage patients present with heart failure symptoms in situations where it is too late to reverse the remodelling that has already occurred. The raised pressure load, as experienced in hypertension, is mainly caused by the increased peripheral blood vessel resistance and reduced atrial compliance (21).

2.3.2 Effects on cardiac Function:

Hypertension leads to physiological disorders such as diastolic dysfunction. The onset and progression of left ventricle hypertrophy (LVH) is affected mainly by blood pressure, however, there are other contributing factors such as obesity, salt intake and age (20). LVH has been reported to be a strong independent risk factor of mortality for patients

diagnosed with hypertensive heart disease (21).

LV concentric hypertrophy often result in decrease in LV diastolic filling and compliance (21). Moreover, systolic function changes which occurs during hypertensive condition are defined by lower left ventricle ejection fractions.

The irreversible remodelling during LV hypertrophy leads to heart failure which can disrupt fluid and electrolyte balance within the extracellular fluid which causes either pulmonary or pedal edema depending on the severity.

2.4 Basic general MRI physics

2.4.1 Origin of Spin

Magnetic resonance imaging is based on the nuclear magnetic resonance principle observed in atoms that possess an overall spin. Although, different atoms can be imaged, hydrogen (^{1}H) is the one used in almost all clinical applications due to its natural abundance in the human body in the form of water and lipid molecules. A hydrogen nucleus consists of a single proton that can be thought of as spinning on its own axis. Protons are positively charged resulting in a magnetic dipole moment and the proton to act like a tiny magnet.

When placed a static magnetic field (B_0) the proton dipoles align almost parallel or almost anti-parallel with the field (Figure 2.4), this is referred to as “spin up” or “spin down” (25).

In quantum mechanical terms, the spins toward the external magnetic field are in low energy state, while protons which spins against the external magnetic field are in high energy state. There is a slight excess of spins in the spin-up state resulting in a small net magnetisation (M_0) in the direction of the magnetic field (z-axis) (26), known as the

longitudinal magnetisation. As the protons precess out of phase with each other thus resulting in a zero net magnetisation in the transverse (xy) plane (transverse magnetisation).

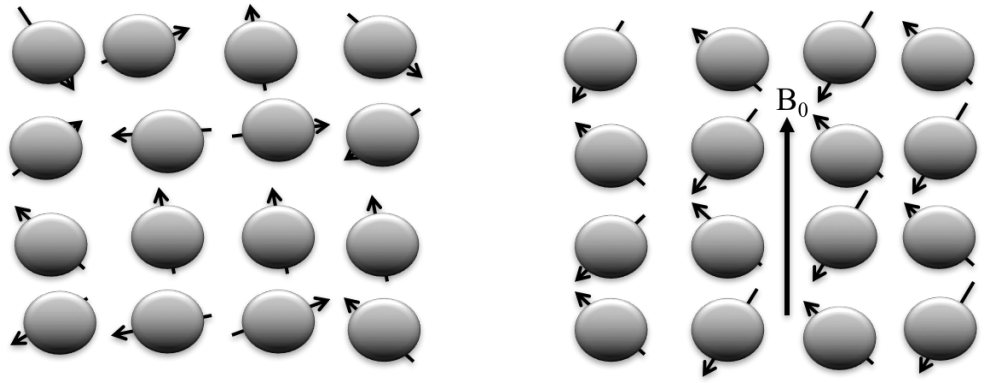

Figure 2.4: Atoms orientated randomly in the absence of magnetic field (on left-hand side). Atoms spin up and spin down alignment of the protons in the presence of strong magnetic field (on right-hand side).

As the magnetic moment is not aligned exactly with the magnetic field, it experiences a torque which causes it to precess around the axis of the main magnetic field. The frequency of precession is called the Larmor frequency (equation 1) (26).

$$w_0 = \gamma B_o \qquad (1)$$

where γ is the gyromagnetic ratio and equal to 42.57 rad MHz T^{-1} for ^1H.

2.4.2 Excitation

The equilibrium longitudinal net magnetisation is extremely small when compared with the static magnetic field. In order to be able to measure the NMR signal and create an image, the net magnetisation is first tipped away from the longitudinal axis by applying a radiofrequency (RF) pulse perpendicular to B_0 and oscillating at a frequency equal to the resonance Larmor frequency. This is known as the excitation pulse or B_1 field. The flip angle is the angle through which the net magnetisation is tipped.

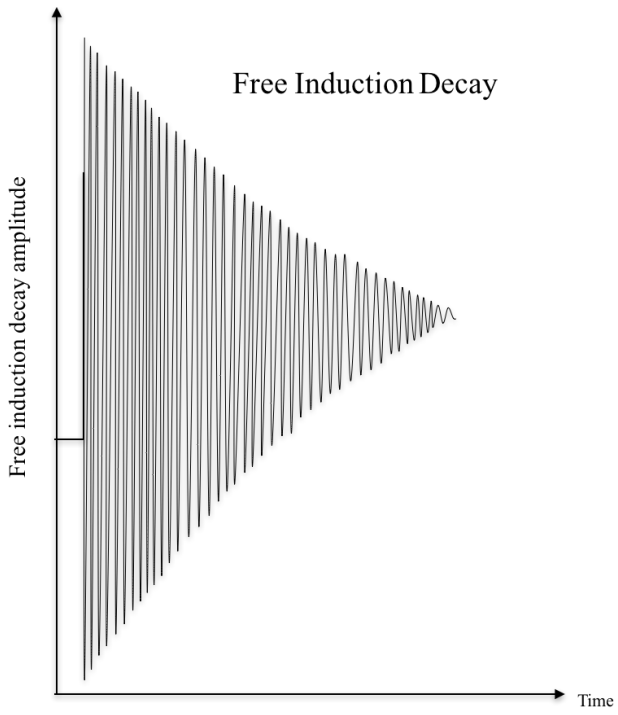

Figure 2.5: NMR signal or free induction decay observed in the transverse plane.

For example, a 90^{o} RF pulse tips the net magnetisation vector into the transverse plane where it precesses around the axis of the static field and induces a signal in a receiver coil. This signal is known as the free induction decay (Figure 2.5): following the excitation pulse the transverse magnetisation (M_{xy}) and therefore, signal amplitude, rapidly decreases to zero as the protons dephase. The longitudinal component of the net magnetisation (M_z) increases exponentially back to its equilibrium value. This process is known as relaxation.

2.4.3 Relaxation

The mechanisms by which the magnetization regain its equilibrium state are collectively known as relaxation. Relaxation starts occurring as soon as RF pulse is stopped. There are two main relaxation processes; transverse and longitudinal relaxation.

Spin-spin relaxation is the decay of the magnetisation in the transverse plane (M_{xy}) due to

the interaction between the spins, or magnetic moments, of neighbouring protons. Note that spin-spin relaxation can lead to complete dephasing in the transverse plane with no corresponding recovery of magnetization in the longitudinal axis, nor a net loss of energy. T_2 is the spin-spin relaxation time, defined as the time taken for transverse magnetization to decay to 37% of its initial value (Figure 2.6). As well as spin-spin interactions, transverse magnetisation is also lost through interaction with magnetic field inhomogeneities; T_2^* is a modified value of T_2 which takes these extra effects into account, and is thus always smaller than T_2. T_2^* is of particular relevance in cardiovascular imaging as it can be used to measure iron load.

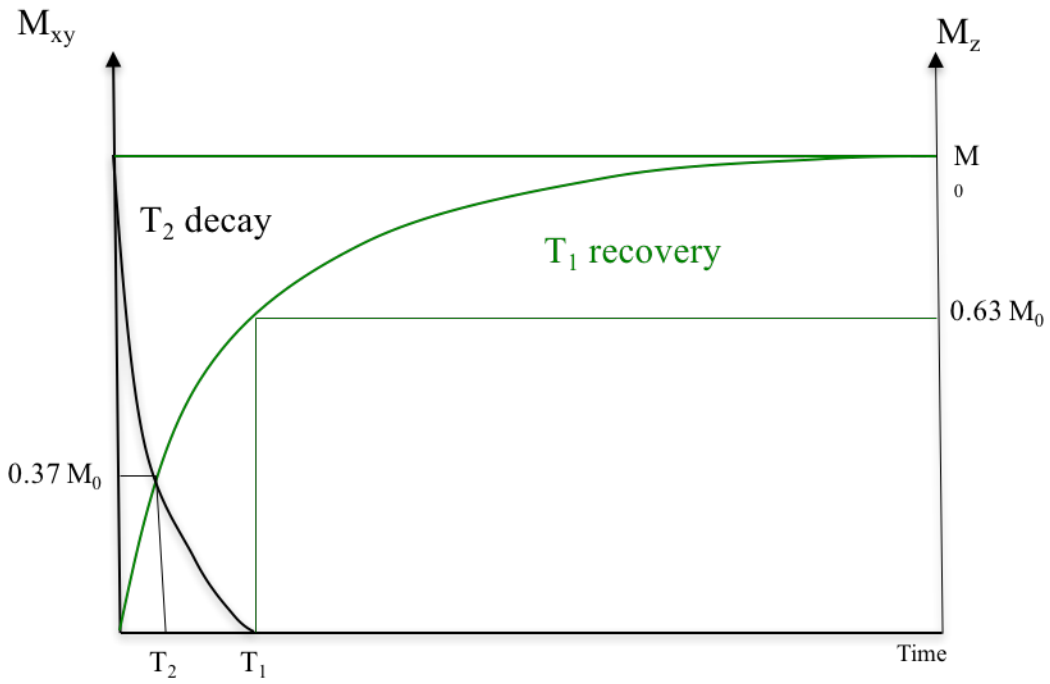

Figure 2.6: Transverse and longitudinal relaxation curves. The transverse relaxation (black) decays with a relaxation time T_2 equals to 37% of its initial value while the longitudinal relaxation recovers with a relaxation time T_1, or the time it takes for the magnetisation to reach 63% of the equilibrium value.

Spin-lattice relaxation is the recovery of the magnetization along the z-direction (M_z), the longitudinal direction, caused by interactions between the magnetic moment of the protons and the surrounding tissue, or lattice. T_1, the spin-lattice relaxation time, is the time taken for longitudinal magnetization to recover to 63% of its equilibrium size.

Figure 6 shows T_1 and T_2 relaxation curves. In human tissue, T_2 is always shorter than T_1.

2.5 Basic Sequences

In order to create an image, the NMR signal needs to be spatially encoded; this is done using a series of time varying magnetic field gradients (often just referred to as gradients). The arrangement of RF pulses and gradients are known as a pulse sequence. As it takes time for spatial to occur, the data collection does not occur during the FID, instead an "echo" is generated during which the data is collected. The way the echo is generated leads to two family of sequences, spin echo in which a second RF pulse is used and gradient echo in which the reversal of one of the gradient is used to generate the echo. Basic spin and gradient spin echo sequences are displayed in Figure 2.7.

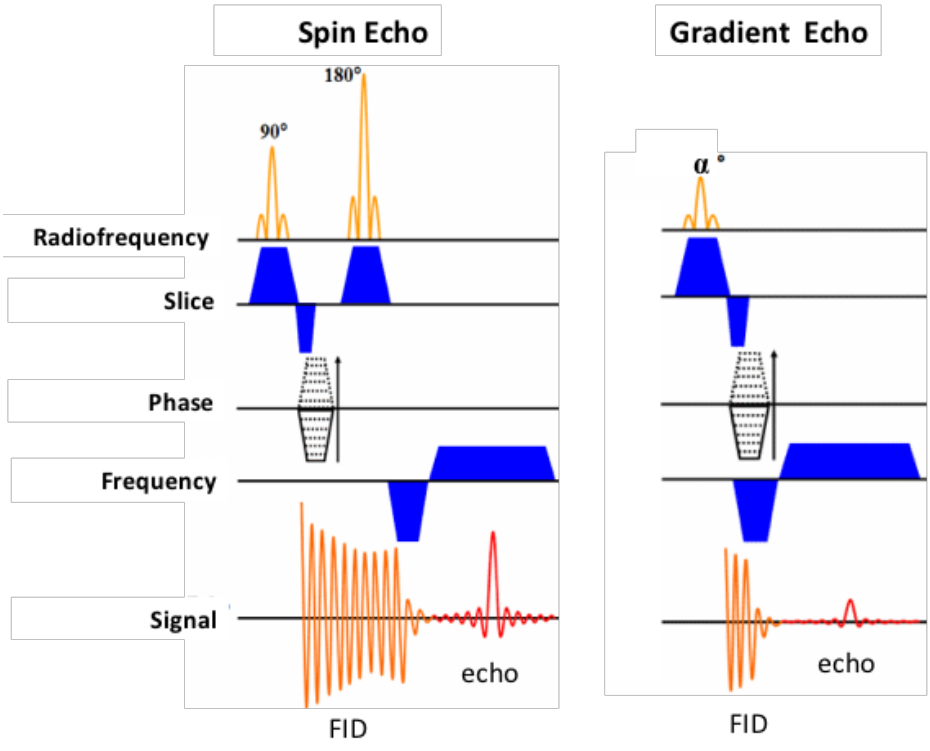

Figure 2.7: Basic spin (left) and gradient (right) pulse sequences. In a gradient echo sequence, a flip angle smaller than 90° is typically used.

The time between the RF excitation pulse and the echo is known as the echo time (TE). For each echo, data is acquired and the raw data is placed in a matrix known as k-space. A line of k-space is acquired per excitation and consequently, the sequence need to be repeated a number of time to acquire sufficient data to create an image. The phase encoding gradient is incremented for each experiment and the time between each successive excitation is known as the repetition time (TR). In a gradient echo sequence, field inhomogeneities are not refocussed and consequently the echo is T_2^* dependent. In most anatomical imaging, the way the image look is directly dependent on the choice of acquisition parameter in particular TE, TR and the flip angle in a gradient echo sequence.

2.6 Cardiac imaging

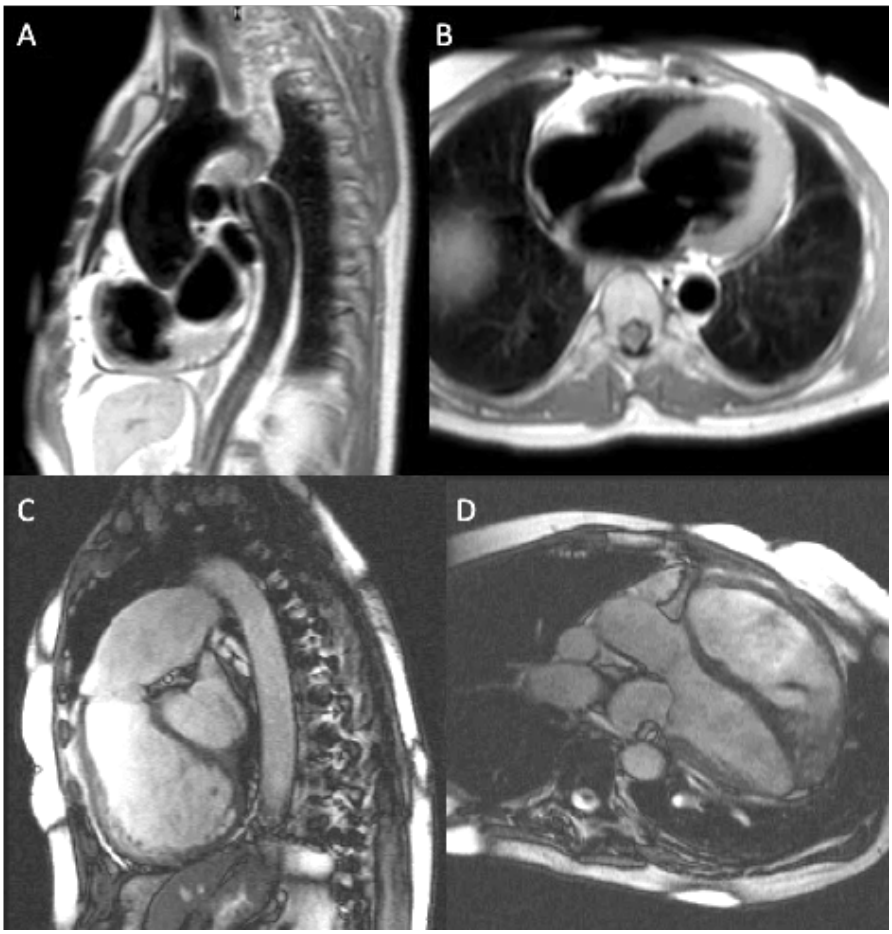

Figure 2.8: Typical Black Blood Spin Echo (A-B) and Bright Blood Gradient Echo (C-D) CMR images.

Cardiac MRI, often called CMR, is routinely used to investigate the anatomy and function of the cardiovascular system. Unlike conventional MRI, it usually relies on the use of an ECG or a vector ECG (VCG) to synchronise the data acquisition to the cardiac motion in order to acquire data in specific phases of the cardiac cycle. Furthermore, unlike most other body part the way the image looks is primarily dictated by blood flow. On one hand, spin echo sequences produce dark blood images as the blood excited by the 90° typically flows out of the slice by the time the 180° pulse is applied to produce the echo, hence generating a signal void is produced (Figure 2.8 A-B). Black blood images are primarily used to look at the anatomy of the heart and the vessels, and the signal from the blood is usually further suppressed by the application of preparation pulses (27). On the other hand, blood appears bright on gradient echo sequences (Figure 2.8 C-D). This is because those sequences use short TR and consequently, static tissues are exposed to numerous RF pulses and their signal gets saturated, or in other words does not recover fully between TR. They are said to be "beaten down" meanwhile fresh blood that hasn't been exposed to RF pulses flows into the slice and therefore appears brighter (27). Bright blood are typically used to evaluate cardiac function (27). These types of images are used in chapter 5 and 6 to compare different FT software packages.

The assessment of global and regional contractile functionality of the heart can be achieved by using cine (gradient echo) sequence synchronised to the patient's ECG. A cine scan provide a series of dynamic images throughout the cardiac cycle, that can be used to visualise cardiac motion abnormality and assess cardiac function (28)(29)(30). In routine CMR imaging, the data are acquired over multiple heartbeats and the acquisition synchronised to the patient's ECG to overcome the motion and artefacts resulting from cardiac motion (10). The methods to synchronise data acquisition are detailed below.

2.6.1 Prospectively ECG gating

For prospective ECG gating (in Figure 2.9 -top), the pulse sequence is triggered on the R-wave. The signal acquisition of the first cardiac phase starts after a short trigger delay (normally used to initiate acquisition of data after the QRS complex) and the number of cardiac phases is chosen by the user but limited by the heart rate. The acquisition of data must be stopped before the end of the cardiac cycle in order to allow for detection of the next R-wave thereby missing the last part of the cardiac cycle (10). This technique requires an estimation of the average R-R interval for each patient being examined which can manually be inputted by the MR operator or automatically captured from the ECG trace within the MR system (10). The estimated R-R interval is then used to estimate the length of the cardiac cycle over which data can be captured as well as to determine the maximum number of cardiac phases that can be acquired.

2.6.2 Retrospectively ECG gating

For retrospective gating (Figure 2.9 -bottom) data is continuously acquired and retrospectively matched to ECG. Data acquisition continues until enough k-space is filled for the defined number of cardiac phases thereby promoting accurate matching of the data to the whole of the cardiac cycle without missing any part from being imaged (10).

2.6.3. Cardiac function

The assessment of functional cardiac can be achieved by several global measures. The Left Ventricular End-Diastolic Volume (LVEDV) and Left Ventricular End-Systolic Volume (LVESV) can both be measured by using CMR or echocardiography. Compared to echocardiography, CMR provides more accurate and reproducible volumetric measurements and is considered the gold standard for LV functional assessment (31).

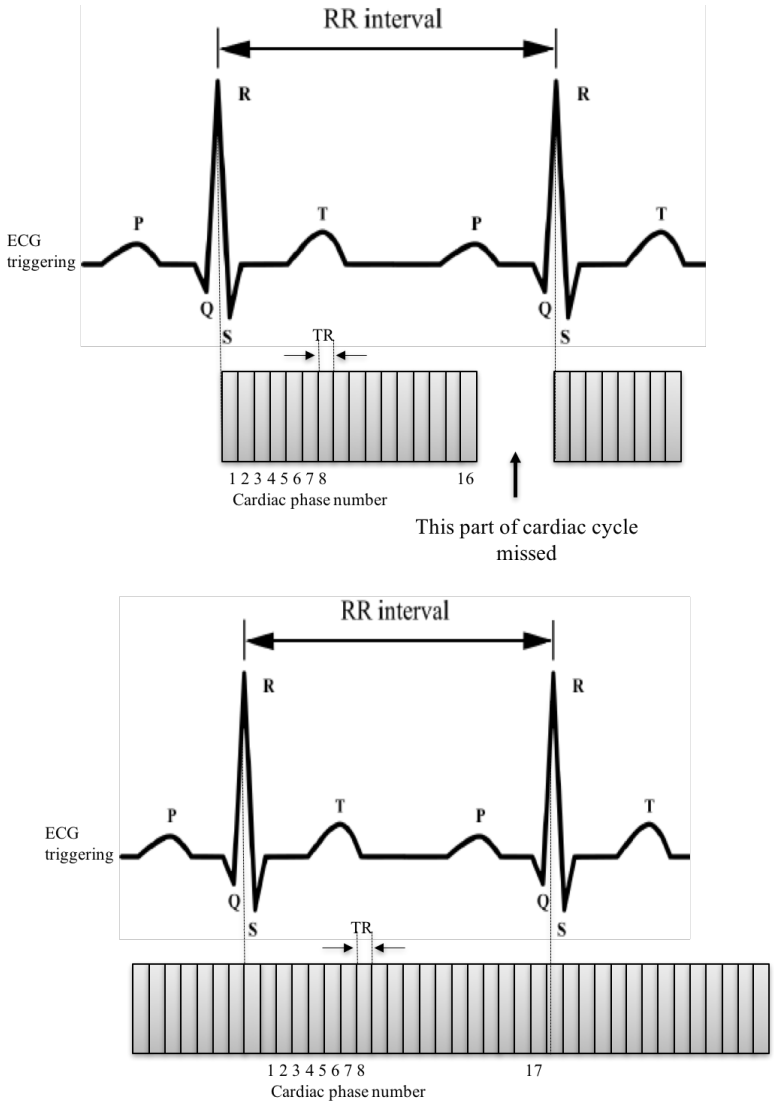

Figure 2.9: Prospective triggering (above) and retrospective gating (bottom) as used in cardiac MR imaging. Image adapted from (10).

CMR calculates the left ventricle cavity volumes from as set of true short axis cine slices that provide a complete coverage of the left ventricle and does not suffer for the limitations of echochardiography (suboptimal acoustic windows and view planning).

The end-systolic volume (ESV) is the volume of blood left in a ventricle at the end of contraction. The difference between End Diastolic Volume (EDV) and End Systolic Volume (ESV) is called the Stroke Volume (SV) and it describes a volumetric measurement of blood ejected from the right and left ventricle with each heartbeat:

$$SV = EDV - ESV \quad (2)$$

The Ejection Fraction (EF) is defined as the volumetric fraction of blood pumped out of the left ventricle with each cardiac cycle. This fraction can be measured for both the left and right ventricles. EF is expressed in % and calculated as the stroke volume SV divided by end-diastolic volume EDV:

$$E_f(\%) = \frac{SV}{EDV} \times 100 \qquad (3)$$

The acquisition of cine images of the heart can be achieved by acquiring data throughout the cardiac cycle over several heart beats as shown in Figure 2.10 (32). For each slice location multiple time points covering the entire cardiac cycle are acquired images to allow function analysis. This technique requires sampling of a number of cardiac phases (usually between 20 and 30 phases, also referred to as ‘’frames’’) to achieve the desired temporal resolution depending on the heart rate of the patient being imaged (32). These images are then analysed semi-automatically to calculate the different parameters as shown in Figure 2.10.

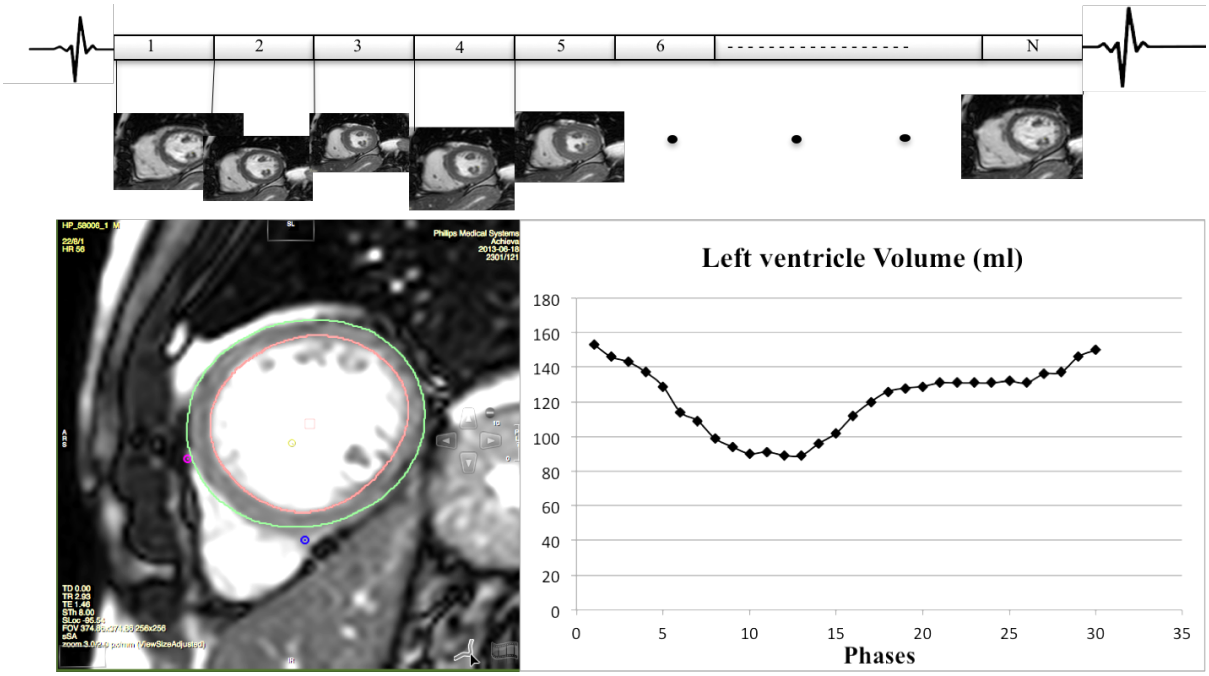

Figure 2.10: The cardiac phases and their images within one cardiac cycle (top). Short axis endocardial and epicardial contours (bottom-left-hand side) are drawn to calculate LV volume metrics. The corresponding left ventricle volume time curve for a short axis cine stack is shown (bottom-right-hand side).

2.7 CMR sequences used for myocardial motion analysis

2.7.1 Fast Gradient Echo sequences

Gradient-echo (GRE) sequences are by nature very fast as they use very short TR and consequently form the backbone of cardiac examination; they are used for function, tagging, perfusion, etc (33).

For a very short TR, the magnetisation does not have time to fully recover between each excitation; this forces the signal to reach a "steady-state" where it stays more or less constant. This happens to both the transverse and the longitudinal magnetisation, see Figure 2.11.

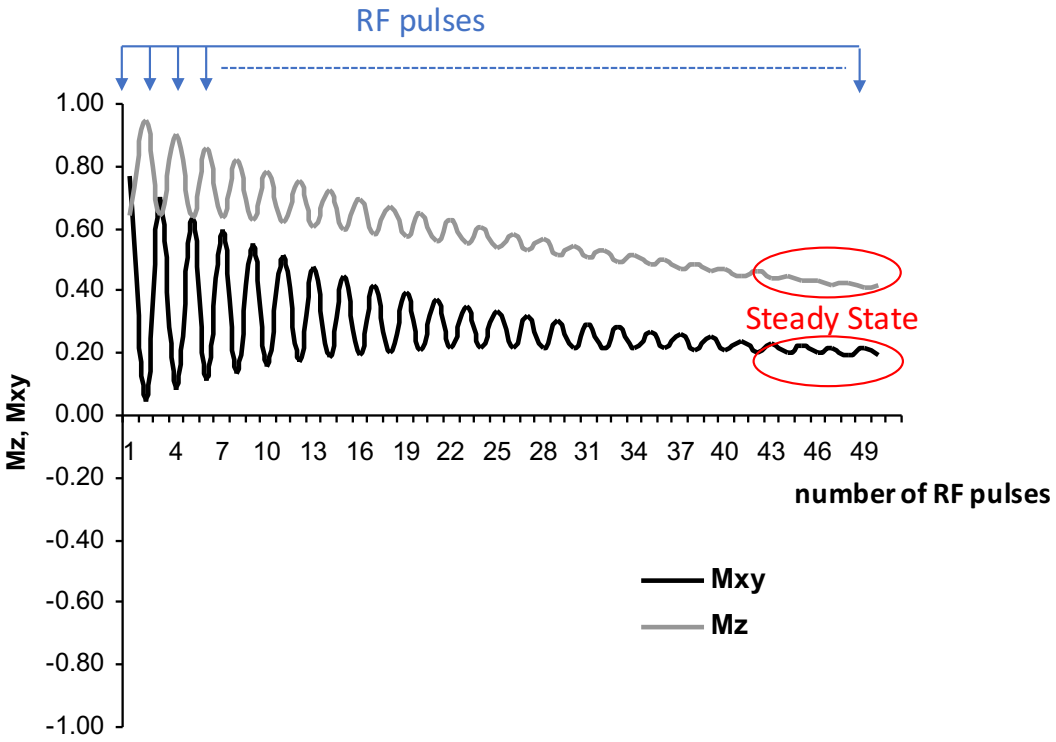

Figure 2.11: Steady state. In fast gradient echo sequences, the signal does not have to fully recover between excitations and consequently, after a number of RF pulses, it will reach a steady state in both the longitudinal and transverse magnetisations.

There are two basic types of fast sequences; for the first type both the transverse and longitudinal magnetisations, this is the balanced or coherent steady-state sequence

(balance steady state free precession or bSFFP, TrueFISP or FIESTA depending on the scanner manufacturer (34). For the second type, the remaining transverse magnetisation is destroyed before each new excitation, those sequences are incoherent or spoiled gradient echo. Pulse sequence diagrams of those two types of sequences are shown in Figure 2.12. Typically, balanced steady states have a high contrast ratio between the myocardium and the blood and have a high signal-to-noise (SNR) ratio. However, they are hard to optimise and are prone to artefacts in particular banding. Spoiled sequences have a lower SNR but tend to be more reliant to artefacts. Typical images are given in Figure 2.13.

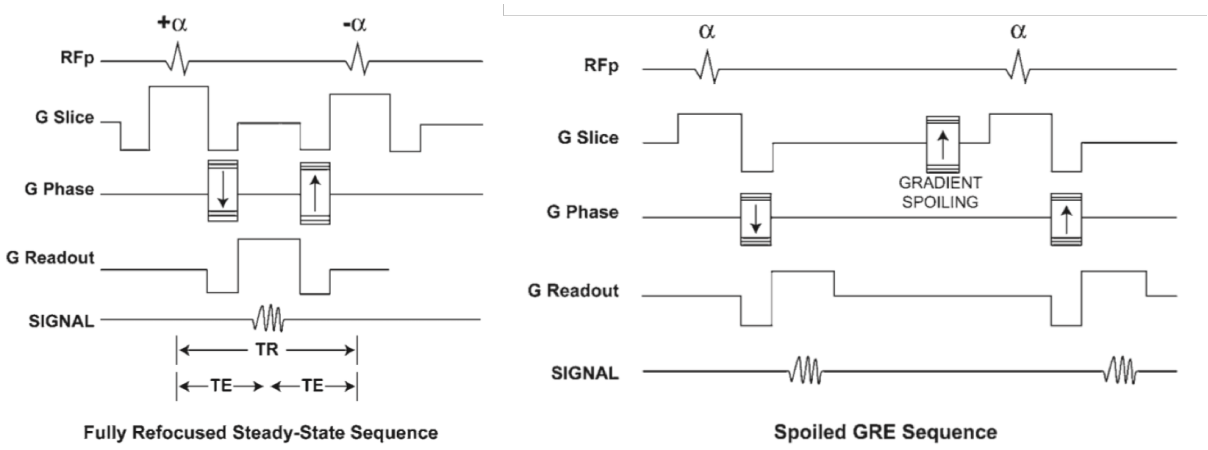

Figure 2.12: The diagram for steady state free precession (on left-hand side), Spoiled gradient echo sequence (on right-hand side) (33).

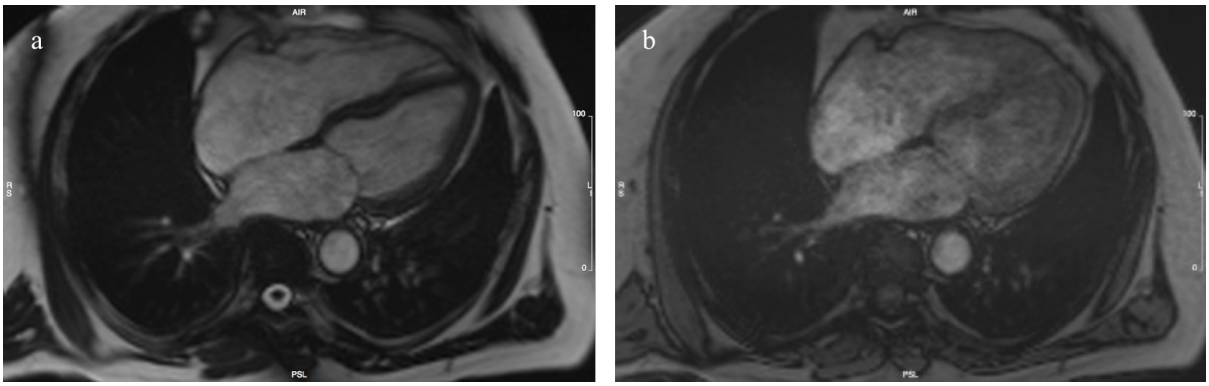

Figure 2.13: Typical cardiac images acquired with balanced (a), and spoiled gradient echo sequences (b).

Cardiac images used in Chapter 5 and 6 for FT analysis were acquired using balanced SSFP sequences. In chapter 6, tagging images were acquired using spatial modulation of magnetisation (CSPAMM) sequence, which is discussed below.

2.7.2 Tagging

The tagging technique was invented in the eighties (35), and quickly improved on (36). This improved methodology still forms the basis of the technique used today this technique and is called "spatial modulation of magnetisation" or SPAMM. The pulse sequence is divided into two phases; a preparation phase where the tag lines are created and an imaging phase which consists of a fast gradient echo sequence (Figure 2.14).

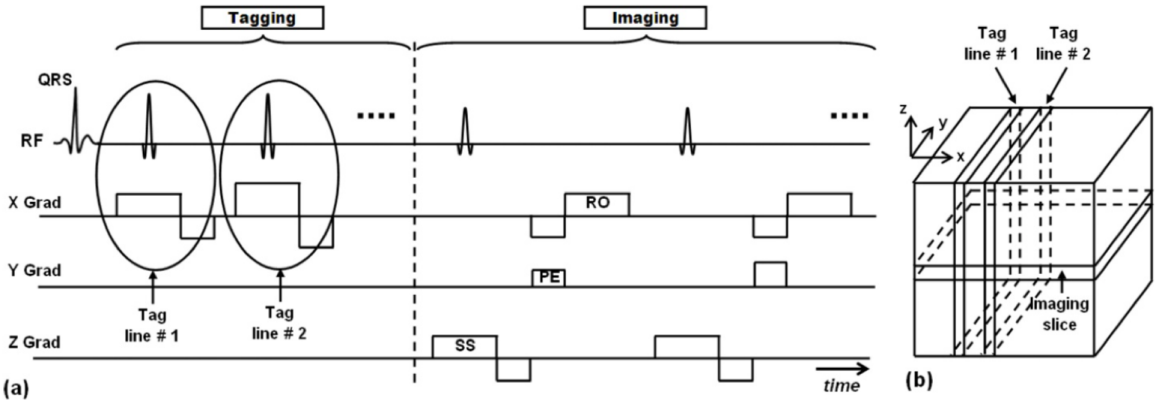

Figure 2.14: The SPAMM technique based on the principle that a slice-selective magnetisation saturated planes are created perpendicular to the imaging slice following the application of the tag pulses which disturbs the longitudinal magnetisation. (a) Pulse sequence showing the tagging preparation stage: tagging a plane requires slice-selective RF pulses to modulate the longitudinal magnetisation (RO = readout, PE = phase encoding, SS = slice selection). (b) Image acquisition stage after tagging showing the acquired slice and the tagged lines perpendicular to it (37).

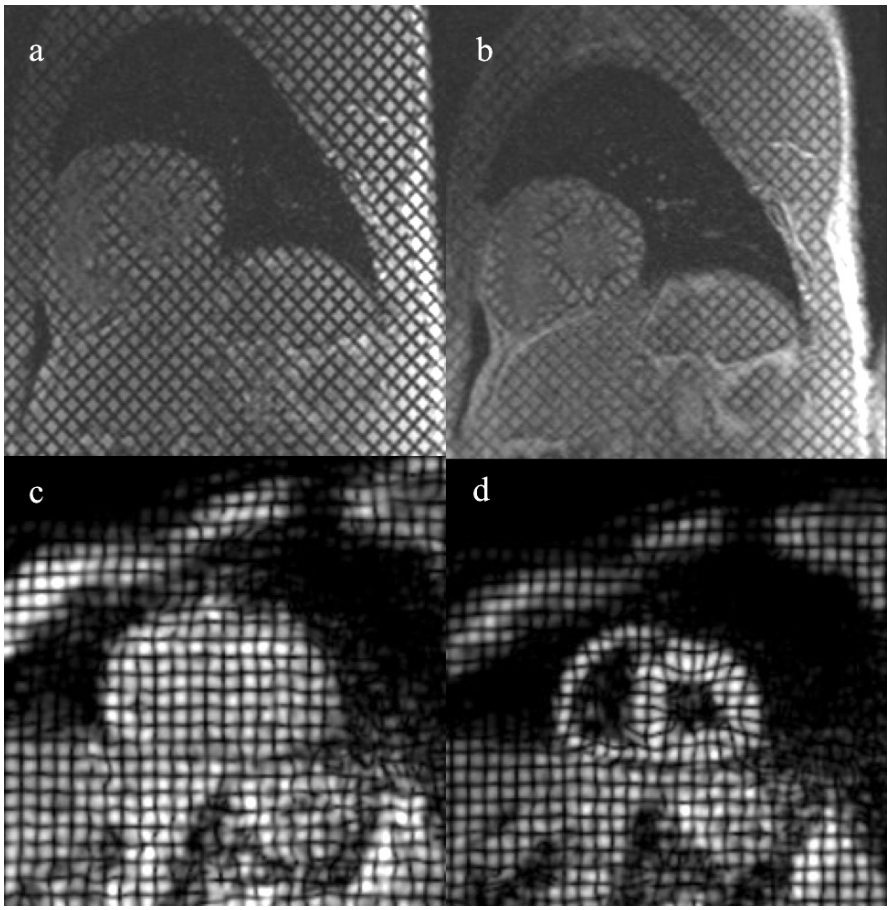

Figure 2.15: Typical SPAMM images at end-diastole (a) and end-systole (b). CPAMM images at end-diastole (c) and end-systole (d). Fading of the tagged lines (reduced contrast) in the systolic phase can be clearly observed for SPAMM (b), while this effect is greatly reduced in CSPAM (persistent tag lines contrast) (d).

Myocardial tissue tagging can be generated through the conventional SPAMM sequence (Figure 2.14). Tag preparation requires the application of slice selective radiofrequency pulses perpendicular to the imaging plane in order to disturb the longitudinal magnetisation at the point of intersection between the imaging plane and the selected slice without affecting other regions within the slices (37). The application of the first RF pulse brings all spins in phase by tipping the magnetisation into the transverse plane followed immediately by the application of a gradient pulse along the desired tagging direction. The applied gradient pulse modulates the transverse magnetisation in a sinusoidal pattern along the direction of the gradient by increasing the phase shift of the spins along this

direction. The modulated transverse magnetisation then returns to the longitudinal plane following the application of the second RF pulse. Finally, a spoiling gradient is applied to remove any residual transverse magnetization prior to image acquisition.

The CSPAMM (complementary SPAMM) tagging technique was introduced to resolve the problem associated with fading of tagging contrast through the cardiac cycle due to longitudinal relaxation commonly encountered in the SPAMM sequence (36) (see Figure 2.15). This fading phenomenon makes tracking of tagged lines extremely difficult and results in incomplete analysis of myocardial deformation in the diastolic cardiac phases. To reduce this effect, CSPAMM uses two SPAMM tagging sequences where the polarity of one of the RF pulses is inverted in the second tagging sequence. The final tagged images are then produced by subtracting the pair of SPAMM images. This results in: i) the removal of the static (DC) component; and ii) an enhancement of the amplitude of the tagged magnetisation, enabling it to last for longer compared to SPAMM (Figure 2.15 b and d).

Chapter 3: Myocardial Deformation Assessment Using Cardiovascular Magnetic Resonance Feature Tracking

3.1 Introduction

There is a growing recognition that early detection of cardiac abnormalities could improve patient quality of life and reduce both morbidity and mortality (38)(39)(40). Extensive improvements and developments in CMR sequences and post-processing techniques have been introduced to facilitate their use in clinical settings in order to improve the diagnostic accuracy of CVD in its onset stage (41)(42)(43).

Recent research has proven that global measures, such as ejection fraction, are only an indicator of global heart function and cannot be used to infer regional function, nor to detect any ventricle dysfunction at the very early stages of established diseases (44). Contrary to visual myocardial wall-deformation analysis, indices including strain, strain rate and torsion can be sensitive indicators of underlying myocardial contractile dysfunctions. Those indices can be also derived from CMR-tagging images (45). Tagging sequences use spatially selective saturation pulses to create dark lines on the myocardial tissue at the end diastole, with those lines persisting throughout part of or all the cardiac cycle (35). These techniques have since undergone extensive development and improvement for both imaging sequences (46)(47)(41), and post-processing methods (43)(42). CMR-tagging is now considered to be the gold standard for myocardial regional function assessment (48)(49).

This chapter first explains the principles of FT and the measurements that can be calculated using the method. Second, it reviews the expanding field of feature tracking with a particular emphasis on clinical and multimodality comparative studies.

3.2 Feature tracking Principles and Derived Cardiac Motion Parameters

3.2.1 Feature Tracking

CMR feature tracking has been introduced in 2010, as a quantitative post-processing technique for cine SSFP sequences that are acquired as part of routine clinical cardiac examinations (50). The fundamental principle of the feature tracking method is based on optical flow to extract spatiotemporal image features, such as varying image signal intensities, local textures and patterns from the cine images. The technique can then track anatomical features, such as epicardial and endocardial borders and myocardial tissue, in consecutive cine image frames by searching for the most comparable features in a local neighbourhood (defining a local voxel search window).

Current FT software packages are semi-automated and rely on an operator to manually delineate the initial endocardial and epicardial contours, usually on the end-diastolic cardiac phase. This frame then serves as the initial time point from which all motion parameters are calculated. Myocardial deformation parameters such as displacement, velocity, strain and strain rates can be computed at local and global levels. Further details on the operation of the FT software used in this thesis can be found in chapter 4. FT was initially developed for 2D cine images but can easily be extended to 3D cine images based on the same principles. The details of how tracking is implemented in different FT-software packages are not always known and this might affect the quality and accuracy of

the tracking and of the derived strain measurements. Furthermore, results are also affected by CMR imaging sequence parameters, such as temporal and spatial resolutions, and image quality, in particular signal-to-noise ratio (3) (51)(39).

3.2.2. Parameters

Quantitative regional assessments can add incremental information in early stage of cardiac diseases that can improve the quality of life for many cardiac patients. The regional assessment of cardiac function includes displacement, velocity strain and strain rate. A schematic of the different parameters measured by FT are given in Figure 3.1.

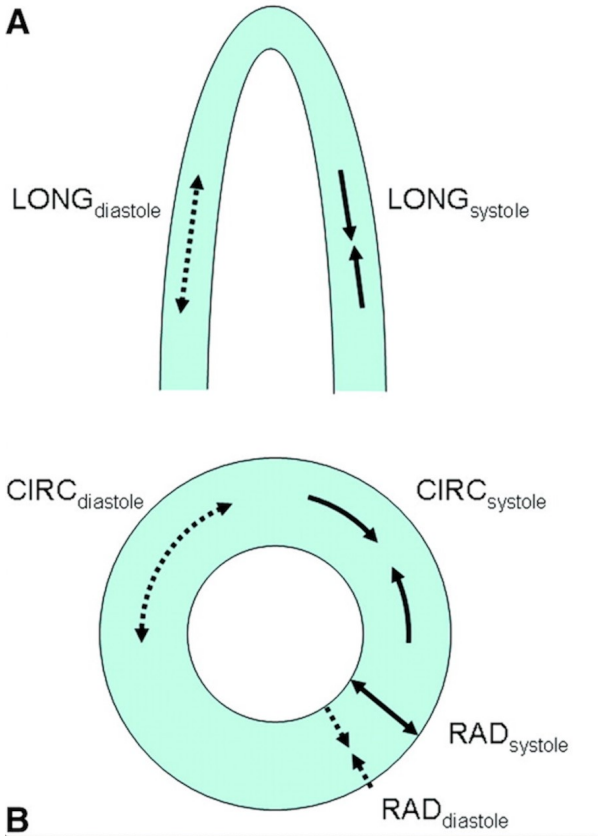

Figure 3.1: Myocardial deformation contains three strain components, circumferential, radial and longitudinal of the left ventricle: longitudinal (A), radial and circumferential (B). The direction of the deformation in diastole is shown as a dashed line and in systole shown as a solid line. The myocardial fibres shorten and lengthen in the three spatial directions: longitudinal, radial and circumferential. The strain can be calculated as the difference between myocardial fibre length (radial, circumferential and longitudinal) at end-diastole and at end-systole divided by the length at end-diastole, and expressed as percentage (%) (52).

The principal measurements can be defined as follows:

Displacement: It is the distance covered by a moving object over time. The object does not undergo deformation when all parts move with the same velocity. However, if different parts of the object move with different velocities, the object will be undergoing deformation (53).

Strain: Strain is a dimensionless quantity of myocardial deformation (54). It is mathematically defined as the change of myocardial fiber length during stress at end-systole (l) compared to its original length in a relaxed state at end-diastole (l_0):

$$Strain = \frac{(l - l_0)}{l_0} \quad (1)$$

Strain is usually expressed as a percentage (%).

Negative strain indicates fiber shortening or myocardial thinning, whereas a positive value describes lengthening or thickening (54). Put simply, strain measures the magnitude of myocardial fiber contraction and relaxation.

Strain Rate: The change of strain per unit of time is referred to as strain rate (SR). It is usually expressed as (%/s).

Longitudinal, radial and circumferential measurements: Cardiac function can be further assessed by more detailed measurements. This is achieved by calculating the deformation in particular segments and in specific directions. There are three main components of contraction deformation: radial, longitudinal, and circumferential (54).

- Longitudinal contraction represents motion from the base to the apex, which represent lengthening and shortening in the longitudinal direction (Figure 1.A).
- Radial contraction in the short axis is perpendicular to both long axis and the myocardial wall (see Figure 1.B). Thus, radial strain represents myocardial thickening and thinning.

- Circumferential strain is defined as the in plane myocardial circumferential motion (rotational motion) (see Figure 1.B).

Longitudinal deformation is assessed using longitudinal cardiac views (horizontal long axis, vertical long axis) while short axis views are used to assess in-plane circumferential and radial deformations.

3.3 Review of FT literature published to date

3.3.1 Feature Tracking (CMR-FT) studies

Cardiovascular Magnetic Resonance feature tracking (CMR-FT) is a quantitative post-processing technique that tracks myocardial tissue motion on SSFP cine images, the most commonly used sequence in clinical cardiac function assessment. The first software package based on FT techniques was introduced by TomTec Imaging Systems GMbH (Munich, Germany) and has been used in most clinical studies published to date (51)(50) (55). More recent studies used a different FT software package: a tissue tracking module within the CVI42 software (Circle Cardiovascular Imaging Inc. Calgary, Canada) (56); A summary of studies using CMR-FT is given in Table 3.1.

Some clinical studies were dedicated to assessing the reproducibility of FT by evaluating inter- and intra-observer variability, whereas others applied FT to both healthy subjects and patients to quantify the difference in cardiac deformation parameters between those groups (55)(4). Feature tracking can be applied to evaluate the function and the mechanics of all heart chambers: right ventricle (RV), left ventricle (LV) and atrial deformations.

CMR-FT was applied to detect quantitative motion changes at rest and stress in the LV, (51)(7) as left ventricular motion abnormalities detected by CMR post-processing

techniques could be an early and sensitive tool for any contractile dysfunction. The quantitative wall parameters derived from cine images were assessed at rest and during dobutamine stress in healthy volunteers (7) and in patients with ischaemic cardiomyopathy (51). CMR-FT demonstrated its ability to detect wall motion changes between rest and stress, where circumferential and radial strains increased significantly with dobutamine in both studies. However, there was no response to dobutamine in dysfunctional segments with scar in patients with ischaemic cardiomyopathy compared to non-dysfunctional segments. In stress studies, the more reproducible myocardial deformation parameter for inter- and intra-observer was circumferential strain (51)(7). CMR-FT can then be used to assess strain measures at rest and stress and could provide a potential method for assessing wall contraction changes.

Heart failure and cardiomyopathies have also been evaluated using CMR-FT in particular hypertrophic cardiomyopathy (4). The ability of CMR-FT to differentiate between patients and healthy controls was evaluated in two studies. (50)(4) In hypertrophic cardiomyopathy and heart failure patients, both left atrium longitudinal strain (22.1% and 16.3 %) and strain rate (0.9 s^{-1} and 0.8 s^{-1}) were lower than in healthy subjects (strain 29.1% and strain rate 1.1 s^{-1}).(4) Scarred segments showed lower contractile function, radial displacement, radial velocity, radial strain and longitudinal strain values compared to non-scar segments. Radial strain was shown to be the best parameter to discriminate between scarred segments from non-scarred ones (50).

Diseases of the aorta have also been given a great deal of attention in clinical research, in particular coarctation of the aorta (COA) (55) (57). Repaired COA patients were assessed using CMR-FT compared to normal subjects (55). Global radial and global longitudinal strains were decreased in patients, while global circumferential strain was preserved compared to normal subjects. In the presence of hypertrophy, global longitudinal strain was significantly reduced, which could be used as an indicator of early LV dysfunction.

A study carried out by Maret et al. assessed the ability of the CMR-FT technique to detect scar defined with gadolinium-enhanced CMR of LV(50). Scarred segments showed lower functional measurements than distant segments. Myocardial function can also be measured by FT-motion parameters, such as velocity and displacement of a specific myocardial point or segment. Myocardial wall contractility will be reduced in the presence of scar and as a consequence of reduced myocardial blood flow.

CMR-FT applications were not limited to cardiovascular disease patients, but included healthy subjects to assess inter-study reproducibility at global and segmental levels. Circumferential strain was found to be the most reproducible component, as its coefficient of variation (CV) is 20.3%, whereas reproducibility for radial strain was poor (CV= 27.2%). (6) In another study, inter- and intra-observer variability at rest was best for circumferential strain and the observer-variability did not significantly increase with stress (7).

To evaluate whether inter-study reproducibility is affected by physiological variations, sixteen healthy volunteers underwent CMR examinations 3 times on the same day: the first scan was conducted after fasting, the second scan immediately after the first scan, and the last examination was a non-fasting scan in the afternoon. No diurnal variation was observed (6). Global measures showed no significant difference among the three repeated scans, as opposed to segmental measures, which were significant for radial strain.

Table 3.1: Comparison between studies using CMR-FT technique.

Study	Strain parameters	Software	Healthy Subjects	Subjects Disease studied	Main findings		Limitations
					Positive	Negative	
Schuster et al., 2011 (7)	RV & LV C, R, L Segmental, Global	Tomtec	10	-	- During dobutamine stress, CS & RS increased significantly. - CS, best observer variability of LV.	- Worse observer variability of RV- LS.	- Small sample size.
Schuster et al., 2013 (51)	LV C, R Segmental	Tomtec	-	15 Ischaemic cardiomyopathy	- No response to dobutamine in dysfunctional segments with scar in all C & R strain parameters.		- Small sample size. - No Follow up post-revascularization data. - No functional recovery data.
Kowallick et al., 2014 (4)	LA L Global and segmental	Tomtec	10	20 Hypertrophic cardiomyopathy (10) Heart failure (10)	- Excellent inter- & intra-observer variability for all strain and SR. - LS discrimination between patients and healthy controls.		- Small sample size.
Taylor et al., 2014 (5)	LV C, R Segmental	Tomtec	55	108 Cardiomyopathy	- Lower CS & RS in patients than healthy controls.		- Heterogeneous age and gender groups.
Maret et al., 2009 (50)	LV R, L Global and segmental	Tomtec	-	30 Presence of LV scar	- Lower functional measures in scarred segments than distant segments.		- Heterogeneous (gender). - large number of infarctions with subendocardial distribution is needed to be tested by the FT-technique. - Low accuracy of ejection fraction.
Morton et al., 2012 (6)	LV R, L Global and segmental	Tomtec	16	-	- More reproducible for global measurements than segmental ones. - CS most reproducible measure of LV.	- Variable inter-study reproducibility. - L measures least reproducible segmental measure of RV measurements. RS least reproducible global measurement.	- Small sample size.

C= Circumferential, R= Radial, L= Longitudinal, CS= Circumferential strain, RS= Radial strain, LS= Longitudinal strain, CSR= Circumferential strain rate, GRS= Global radial strain, GLS= Global longitudinal strain, GCS= Global circumferential strain, LV= Left ventricle, RV= Right ventricle, LA= Left atria
l.

3.3.2 Comparison between CMR-FT and CMR-tagging

There are currently two main CMR post-processing techniques that have been applied in order to quantify regional myocardial function: analysis of CMR tagging, and CMR-FT using functional cine images (4)(5)(58). Regional myocardial deformation strain is a sensitive measure for detecting onset stages of myocardial dysfunctions and can be derived from CMR-FT and CMR-tagging techniques. CMR-FT and CMR-tagging techniques can help in early identification of myocardial dysfunctions. These techniques could prove important for clinical risk management, starting treatment and helping in therapy decision-making (45)(59). CMR-FT is increasingly being used in studies to assess its potential in routine clinical evaluation, as CMR-FT analysis computes strain from routinely performed SSFP cine images without the need to acquire any additional CMR sequences. However, CMR-FT requires standardisation of MRI acquisition and post-processing protocols to reduce any possible discrepancies between studies beside inherent natural physiological variability between healthy subjects (8). As for CMR-tagging, tagged lines fade out towards the end of the cardiac cycle making them difficult to track using post-processing techniques (60). Few studies have compared CMR-FT to CMR-tagging in healthy subjects or patients to diagnose subtle myocardial motion abnormalities. The number of subjects in each study needs to be taken into account when comparisons are being made with other studies. A summary is given in Table 3.2.

Muscular dystrophies such as Duchenne Muscular Dystrophy were the subject of regional myocardial function assessment using both FT and tagging techniques (8). The study included healthy volunteers and a large population of Duchenne Muscular Dystrophy patients of different age groups and severity; when strain values from the mid-left ventricular short-axis slice were compared between the two techniques, the mean circumferential strain was highly correlated. This study showed that the two techniques

were comparable.

Comparison between the two techniques was also carried out in cardiomyopathies (1)(45)(61). One study compared the techniques in both healthy subjects and hypertrophic cardiomyopathy patients (1). The results showed a closer agreement in time-to-peak circumferential strain than in the magnitude of strain peak between both techniques. A second study compared the techniques in healthy volunteers, patients with left bundle branch block and hypertrophic cardiomyopathy (61). The segmental peak and time-to-peak for systolic circumferential strains were assessed, and both the intra- and inter-observer reproducibility were evaluated. This study demonstrated that absolute values of peak systolic circumferential strain are higher with CMR-FT than with tissue tagging. There was also a significant difference in mean peak systolic circumferential strain values between the populations studied. The inter- and intra-observer agreements were both lower with CMR-FT than with tagging.

While most studies (1)(8) focused solely on systolic deformation parameters, a study by Moody et al. (45) compared both techniques in short and long axis views, both in systole and diastole, in healthy subjects and patients with dilated cardiomyopathy. The study showed a good agreement between CMR-FT and CMR-tagging techniques for systolic global circumferential strain (-22.7 ±6.2% vs. -22.5 ±6.9%, bias= 0.2 ±4%, p=0.8) respectively and early diastolic global circumferential strain rate (1.21 ±0.44 s^{-1} vs. 1.07 ±0.3 s^{-1}, bias= -0.14 ±0.34 s^{-1}). There was an acceptable agreement for systolic global longitudinal strain (-18.1 ±5 % vs. -16.7 ±4.8 %, bias=1.3 ±3.8%, p=0.03) in healthy subjects. In dilated cardiomyopathy patients, the difference between both techniques was not significant (-9.7 ±4.5% vs. -8.8 ±3.9%, p=0.44), whereas the agreement for early diastolic global longitudinal strain rate was poor, and the difference between both techniques was significant ($p < 0.001$) in healthy subjects. Overall, there was an

acceptable agreement between systolic and diastolic strains for some parameters measured by both techniques in both groups. However, the study only included 35 healthy subjects and 10 dilated cardiomyopathy patients; this could have had an impact on the statistical results, and should be considered when comparing this study to other studies with larger population sizes.

A different study was carried out to compare the two techniques for diastolic and systolic strain measurements in patients with aortic stenosis (62). In this study, the strain parameters were consistently higher with FT than with tagging. Furthermore, the interstudy reproducibility for circumferential peak systolic strain was excellent with FT and good with tagging, whereas the reproducibility for circumferential peak end diastolic strain rate was good only with basal and mid-slices.

Finally, FT and tagging were compared in healthy adults (30). For global measurement of strain, there was a good agreement between both techniques with circumferential strain, but this was not the case with radial and longitudinal strains. Reproducibility showed the same trends with reasonable inter-observer variability for circumferential measures. The study showed some variation in strain with gender: longitudinal strain values were higher in females, whereas radial values were higher in males.

There are obvious limitations in comparison studies that could explain the published disparities and disagreements in results. CMR-FT studies have been published by numerous centres using heterogeneous equipment (including field strength) and sequence acquisition parameters (temporal resolution, spatial resolution, slice orientation etc.). All these differences can affect the reported results and unfortunately, few studies include detailed limitations and reproducibility data. Although MRI acquisition parameters (temporal resolution, spatial resolution, slice orientation etc.) could be made as close as possible for both tagging and SSFP sequences, they are not identical (61)(63). There were also differences in external parameters such as population demographics (64).

Table 3.2: Comparison between studies using CMR-FT and tagging techniques.

Study	Strain parameters	Software	Healthy subjects	Subjects Disease studied	Main findings		Limitations
					Positive	Negative	
Hor et al., 2010 (8)	LV C Global and segmental	TomTec HARP	42	191 Duchenne Muscular Dystrophy (DMD)	- CS derived by FT highly correlated with tagging technique. - Low intra-observer and inter-observer bias and variability for FT.		- Analysis only performed on a mi ventricular short axis slice. - Only average strain was calcul regional measures were not included i study.
Harrild, D.M et al. 2009 (1)	LV C	MATLAB	13	11 Hypertrophic cardiomyopathy	- Close agreement between both techniques. - Better agreement for time to peak strain than peak strain magnitude.		- Small sample size. - Endocardial circumferential strain mid-left ventricle was the only exam parameter. - Further study needed to examine r and longitudinal strains as well epicardial strain.
Augustine et al. 2013 (30)	C, R, L Global and segmental	TomTec CIMTag2D	145	-	- Good agreement between both techniques for CS. - Acceptable global inter-observer variability for circumferential measures. - Some variation in strain with gender: longitudinal strain higher and radial lower in females.	- Poor agreement between FT and tagging for R and LS. - Poor inter-observer reproducibility for R and LS for both techniques.	- Healthy subjects were heterogen related to gender.
Singh et al., 2014 (62)	C, L Global and segmental	TomTec InTag	-	18 aortic stenosis (AS)	- Excellent inter study reproducibility for circumferential peak systolic strain with FT and good with tagging. - Good reproducibility for circumferential peak end diastolic strain rate for basal and mid slices only.	- Strain parameters consistently higher with FT.	- Small sample size.
Wu et al., 2014 (61)	LV C Segmental	TomTec MASS	10	20 left bundle branch block (10) hypertrophic cardiomyopathy (10)		- Intra and inter-observer agreement of segmental peak SCS and T2P-SCS substantially lower with FT compared with tagging. - Significant differences in mean peak SCS values between FT and tagging. - Higher absolute values of peak SCS with FT compared with tagging. - Significant difference in mean peak SCS values.	- Small sample size. - Similar but not identical slice level for CMR-FT and CMR-tagging.
Moody et al., 2014 (45)	LV C, L Global	TomTec CIMTag2D	35	10 dilated cardiomyopathy	- Good agreement between both techniques at peak global systolic circumferential strain and early global diastolic circumferential strain rate. - Acceptable agreement at peak systolic global longitudinal strain.	- Poor agreement for early diastolic global longitudinal strain.	- Small sample size. - As a result of tag fading, late dias strain measures not possible.

C= Circumferential, R= Radial, L= Longitudinal, CS= Circumferential strain, RS= Radial strain, LS= Longitudinal strain, SCS= Systolic circumferential strain, T2P-SCS= Time-to-peak-systolic circumferential strain, LV= Left ventricle. Tomtec= MR FT analysis (TomTec Imaging Systems, Munich, Germany). Tagging analysis: HARP= (Diagnosoft, Palo Alto, California). CIMTag2D= (CIMTag2D v.7, Auckland MRI Research Group, New Zealand). InTag= (Creatis, Lyon, France) and MASS= (Medis, Leiden, The Netherlands).

3.3.3 Comparison between CMR-FT and Echocardiography

The calculation of strain and strain rate always depends on image quality; this can have an effect on the reliability and reproducibility of deformation parameters derived from echocardiographic images. Echocardiography is limited by acquisition angle and operator dependence (60)(65). CMR is increasingly the method of choice because of its wide field-of-view, better image quality and reproducibility (66) . A few clinical studies have compared echocardiography and CMR-FT in patients and healthy subjects to evaluate the clinical usefulness of the latter in assessing myocardial deformation parameters (67)(2). A summary of studies comparing CMR-FT to echocardiography is given in Table 3.3.

Most comparative studies have focussed on adult congenital heart disease, in particular Tetralogy of Fallot (TOF) (67)(68). A study was carried out in adult TOF patients and healthy subjects comparing CMR-FT to speckle tracking echocardiography (STE) (68). There was a close agreement between global longitudinal and circumferential LV strains measured by CMR-FT and STE techniques, but the agreement was poor for global radial LV strain. There was also a good agreement between both techniques for global longitudinal RV strain. Inter-observer agreement for both techniques was similar for LV global longitudinal strain; however, CMR-FT showed better inter-observer reproducibility for LV circumferential and radial strains and RV global longitudinal strain. There was no significant difference between TOF patients and healthy subjects in LV circumferential strain (-23.5 ±6 vs. -22 ±3.9%, p=0.28) with CMR-FT, while LV longitudinal strain (-19.2 ±4 vs. -21.3 ±3.3%, p=0.048) and LV radial strain (22 ±8.9 vs. 28 ±11.3%, p=0.2) were found to be lower in patients. Furthermore, RV longitudinal strain was lower in patients compared to healthy subjects (18.3 ±4.3 vs. 24.1 ±4%, p=0.0001) (68).

The agreement between CMR-FT and STE techniques were also assessed for LV and RV

global longitudinal, radial and circumferential strains in TOF patients. (67) LV global circumferential and longitudinal strains had the best inter-modality agreement, whereas poorer inter-modalities and inter-observer variability were found for global radial strain, contrary to what was observed for radial strain in a previous study (68). When comparing TOF patients to healthy subjects, LV global circumferential, radial and longitudinal strains and RV global longitudinal strain were lower in patients compared to healthy subjects; this is in line with previously reported data (68).

The feasibility of CMR-FT technique was assessed in patients with dyssynchrony (2). There was a reasonable agreement in radial dyssynchrony in patients with more marked dyssynchrony between CMR-FT and STE. The results showed a significant increase in radial myocardial contraction and circumferential strain after stent implantation. The feasibility of CMR-FT technique compared to echocardiography was also assessed in healthy subjects and patients with left ventricle hypertrophy cardiomyopathy (66). CMR-FT-derived strain and strain rate correlated well with echocardiography, and consequently could become an alternative to echocardiography for assessing myocardial deformation parameters in clinical settings in the future.

3.4 Discussion

FT was used to assess regional cardiac function by calculating myocardial deformation parameters and their variation with age, gender and different cardiac dysfunction pathologies. An increasing number of research studies are using feature tracking and comparing it to tagging techniques or echocardiography in both patients and healthy subjects. Some studies have proved the usefulness of feature tracking for evaluating myocardial deformation indices and differentiating between healthy and disease states.

Table 3.3: Comparison between studies using CMR-FT and echocardiography

Study	Strain parameters	Software	Healthy subjects	Subjects Disease studied	Main findings		Limitations
					Positive	Negative	
Kempny et al., 2012 (68)	RV & LV C, R, L Global and segmental	TomTec Tomtec (STE)	25	28 Tetralogy of Fallot	- Close agreement between global LV and global RV strain measurements. - Similar inter-observer agreement for both modalities for LV GLS. - Better inter-observer reproducibility for LV CS or RS and RV GLS measured by FT.	- Reproducibility for regional strain using FT technique was poor.	- No TOF patients with different severity of pulmonary regurgitation data, for the association between the severity of pulmonary regurgitation and strain measurements.
Padiyath et al.,2013 (67)	RV & LV C, R, L Global and segmental	TomTec Tomtec (2DE)	20	20 Tetralogy of Fallot	- Best intermodality agreement for GCS followed by GLS. - Acceptable inter-observer agreement for GLS and GCS of LV and RV with both modalities.	- Inter-modality and inter-observer agreements were poor for GRS.	- Small sample size. - Heterogeneous related to age and gender in both groups. - No Right ventricle out flow assessment by FT technique.
Onishi et al., 2013 (2)	R Segmental	TomTec Tomtec		72 Dyssynchrony	- Reasonable agreement between both modalities for the patients with more marked dyssynchrony.		- No available long term follow up data.
Orwat et al., 2014 (66)	L, C Global	TomTec Tomtec	20	20 patients with left ventricular hypertrophy cardiomyopathy (HCM)	- Good agreement between both modalities for LV GLS for healthy and patients.	- Poor agreement for CS and all SR measurements. - Higher LV and RV strain, inter-observer reproducibility compared to SR.	- Small sample size. - Heterogeneous related to age in both group.

C= Circumferential, R= Radial, L= Longitudinal, CS= Circumferential strain, RS= Radial strain, LS= Longitudinal strain, CSR= Circumferential strain rate, GRS= Global radial strain, GLS= Global longitudinal strain, GCS=Global circumferential strain, LV= Left ventricle, RV= Right ventricle. Tomtec= MR feature tracking analysis. Echocardiography FT: Tomtec (2DE) = 2D Echocardiography analysis. Tomtec (STE)= Speckle Tracking analysis. (TomTec Imaging Systems, Munich, Germany)

However, as summarised in Tables 3.1 to 3.3, the number of subjects varies between studies which has a subsequent impact on statistical results (68). The detection of motion abnormalities in the early stage of CVD is of great importance for an accurate diagnosis. Feature tracking provides a quantitative assessment of left ventricular motion (51)(7), and can therefore be a sensitive tool to detect contractile dysfunction. Significant changes between rest and dobutamine stress were detected by FT technique in ischaemic cardiomyopathy, with no response to dobutamine in dysfunctional parts with scar (51). FT can distinguish scarred segments from distant ones as scarred segments showed lower functional measures (50).

Global strain measures proved to be more reproducible than regional results (4)(6)(67). The potential benefit of global myocardial strain assessment has been shown to be a sensitive indicator of RV function in TOF patients (67). In another study that assessed inter-observer reproducibility in TOF patients, a close agreement was found between global left (LV) and right ventricular (RV) global strain measures (68). The most consistently reproducible strain components were global longitudinal and global circumferential strain, whereas large variations were observed in global radial strain (51)(7).

Despite the increasing number of published studies in feature tracking, there is still an obvious lack of comparison, standardisation and validation studies. Therefore, results of these studies have highlighted discrepancies between the different FT software packages available. Unlike speckle tracking echocardiography (69)(70), CMR-FT has not gone through standardisation and validation in physical or numerical phantom and/or animal models in order to validate it as a routine clinical tool. It is of paramount importance to understand the origin of these discrepancies in CMR-FT results. Consequently, in order to validate and compare the different FT software packages, it would be ideal to develop a

"ground truth" numerical phantom. Such a phantom would also allow for the optimisation of clinical applications. Feature tracking software providers should aim to reach a consensus for the validation and standardisation of reliable deformation parameters and MRI acquisitions and analysis of post-processing methods.

3.5 Conclusion

The current review chapter summarised the main results, reproducibility, and clinical applications of FT studies, as well as their limitations, while also suggesting important possible avenues for future work.

Research studies in healthy volunteers and/or patients either applied CMR-feature tracking alone to assess myocardial motion or compared it to either established CMR-tagging techniques or to speckle tracking echocardiography. These studies assessed the feasibility and reliability of calculating or determining global and regional myocardial deformation strain parameters. Regional deformation parameters are reviewed and compared. Better reproducibility for global deformation perameters was observed compared to segmental parameters. Overall, studies demonstrated that circumferential strain was the most reproducible parameter, usually followed by longitudinal strain; in contrast, radial strain showed high variability.

Based on the high variability and low reproducibility for some deformation strain parameters derived from feature tracking technique noted in various research studies, there was a clear need to compare feature tracking software and establish inter and intra-observer variability in clearly defined populations. Consequently, chapter 5 focusses on the comparison of three FT software packages in 26 hypertensive patients and 28 healthy subjects. Moreover, it is obvious that FT also need to be compared to the current MRI

gold standard that is Tagging. This is the aim of chapter 6 where a large cohort of 28 healthy subjects and 62 hypertensive patients is analysed to compare FT and CMR-tagging.

Although comparative studies with tagging and echocardiography are a necessary step in validating CMR-FT, only numerical phantoms could give an absolute answer when evaluating different algorithms. Ideally, synthetic images mimicking known LV motions should be used to validate and compare the different FT software solutions. This is the main aim of chapter 7 in this thesis.

Chapter 4: Methodology

The aim of this chapter is to describe the common methods used to investigate global and regional myocardial functional parameters calculated from feature tracking and cardiac tagging in the remainder of this thesis. The chapter also details the analysis process for the different CMR software packages. Different software packages were applied to healthy subjects and hypertensive patients; the derived results from the same population were compared, in order to ascertain whether the results from different software packages were comparable in accuracy and precision. The various statistical tests used in the experimental chapters are also discussed. The focus of chapter 5 is to compare the three most commonly available feature tracking software packages: Tomtec (Tomtec MR FT analysis, TomTec Imaging Systems, Munich, Germany), CVI42 (Circle Cardiovascular Imaging Inc. Calgary, Canada) and CIM-FT (CIM-FT, Auckland MRI Research Group, New Zealand). This was carried out on a patient population (26 hypertensive patients) and healthy subjects (28). The comparison includes both inter- and intra-observer variability.

Chapter 6 is a comparative study of FT and tagging techniques. This study includes a larger hypertensive population (62) and the same healthy subjects (28) that was applied in chapter 5, both groups were carried out using two commercially available software were used; one for FT analysis (CVI42) and one for tagging (CIMTag2D).

Image acquisition parameters for both studies are also discussed in this chapter.

4.1 Cardiac magnetic resonance (CMR)

4.1.1 CMR cine acquisition protocol

All CMR examinations were acquired using the recommended CMR protocol as defined by the cardiovascular magnetic resonance CMR guidelines paper for cine imaging and tagging sequences including recommended scan parameters for spatial resolution and temporal resolution, coverage, slice thickness and inter-slice gap (71). The 26 hypertensive patient population analysed in chapter 5 was imaged using a 1.5T scanner (Avanto, Siemens Medical Imaging, Germany), in conjunction with 32-channel cardiac receiver coil was used. LV function was assessed with a retrospective ECG-gated SSFP cine sequence during short breath-holding in the following planes: two-chamber or four-chamber, and three short axis slices (basal, mid, and apical levels). The SSFP acquisition parameters were: echo time (TE) 2.48 ms, repetition time (TR) 1.24 ms, flip angle 70°, typical field of view 292×360 mm^2, slice thickness 7 mm, acquisition matrix size 208×256, and reconstructed pixel size 1.25×1.25 mm^2.

The healthy population analysed in chapter 5 and 6, and the hypertensive population of chapter 6 were all enrolled in the HAPPY London study. All CMR images were acquired using a 1.5T scanner (Achieva, Philips Medical Systems, Best, the Netherlands) and a dedicated 32-channel cardiac receiver coil. Cine image acquisitions were retrospectively ECG-gated. All images were acquired during short breath-holding in the following planes: vertical long axis (VLA or two-chamber), horizontal long axis (HLA or four-chamber), and short axis slices (basal, mid, and apical levels). Left ventricular apical, mid, and basal short-axes cine-images (SSFP) were acquired for all subjects.

The SSFP sequence parameters were: TE 1.44 ms, TR 2.9 ms, field-of-view 205×380 mm^2, acquisition matrix 108×186, slice thickness 8 mm with a 2 mm gap between slices,

30 reconstructed frames per cardiac cycle (typical temporal resolution of 46 ms for a heart-rate of 60 beats per minute), and a flip angle of 60°; typical images are as shown in Figure 4.1.

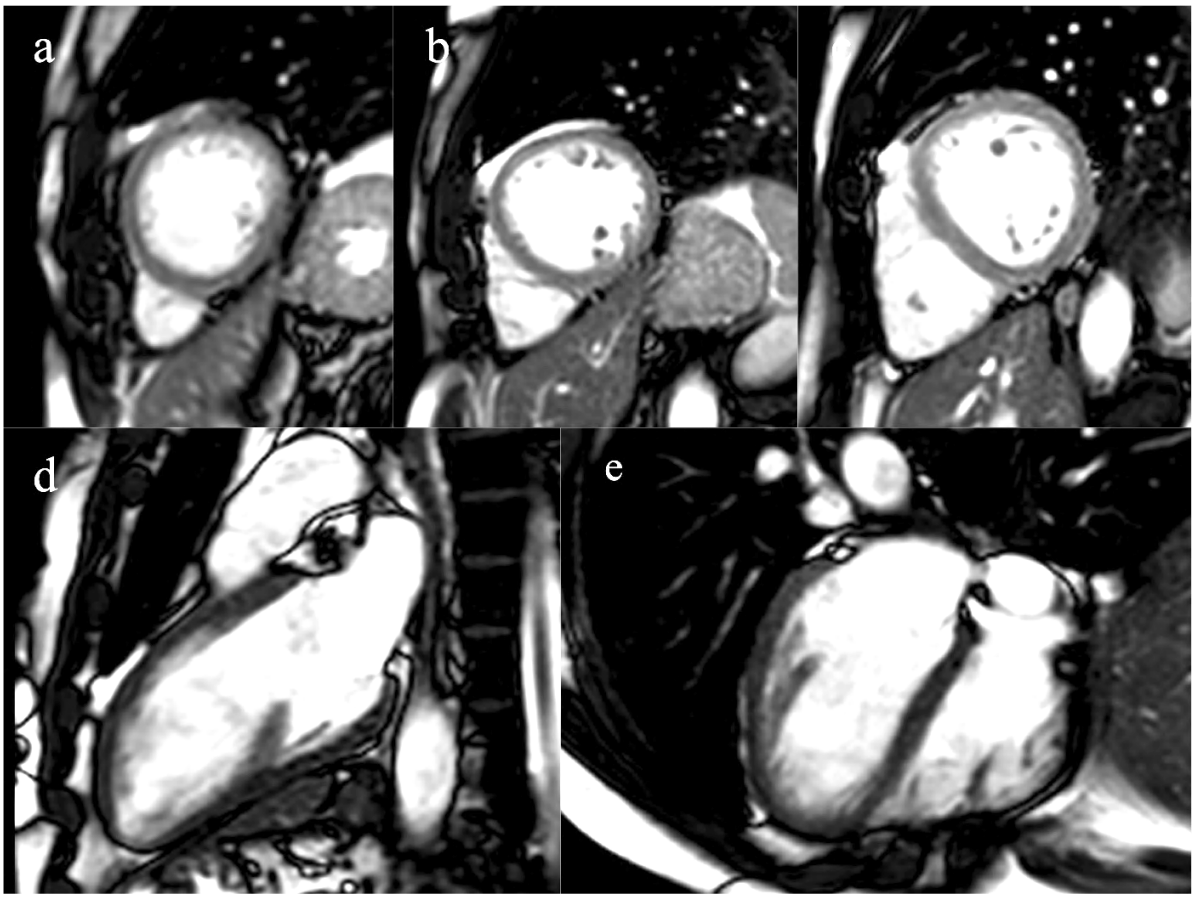

Figure 4.1: Typical SSFP images; (a) apical short axis, (b) mid ventricle short axis, (c) basal short axis, (d) two chamber long axis, (e) four chamber long axis acquired for the study.

4.1.2 CMR-tagging acquisition protocol

In chapter 6, short axis apical, mid and basal two-chamber and four-chamber tagged images matched to the SSFP images were obtained using CSPAMM. Prospectively gated tagged images were acquired as follows; three short axis-tagged images of the LV (base, mid, and apex) four-chamber and two-chamber images were acquired using prospective ECG-gating. A uniform tag grid was created on the images using a CSPAMM sequence, with a tag separation of 7.5 mm, TR 25 ms, TE 10.28 ms, flip angle 25°, tag grid angle

90°, slice thickness 8 mm, and temporal resolution 25 ms; typical images are shown in Figure 4.2.

4.1.3 HAPPY London study

All participants gave written informed consent. The study was approved by the National Research Ethics Committee London-Central on February 21, 2013 (13LO/0094) and was conducted in accordance with the principles of the declaration of Helsinki to be used for subsequent analysis. HAPPY London study data was provided by Dr. Mohammed Khanji (9).

The primary objective of HAPPY London study was to assess the clinical effectiveness of personalised, continuous e-coaching to support a healthier lifestyle as a primary prevention tool in reducing future CV risk and improving quality of life in asymptomatic individuals with high predicted 10-year CVD risk. However, the aim of using HAPPY London data in my thesis was to compare the feature tracking analysis across the different FT software packages (Chapter 5) and to compare these against the tagging technique (Chapter 6)."

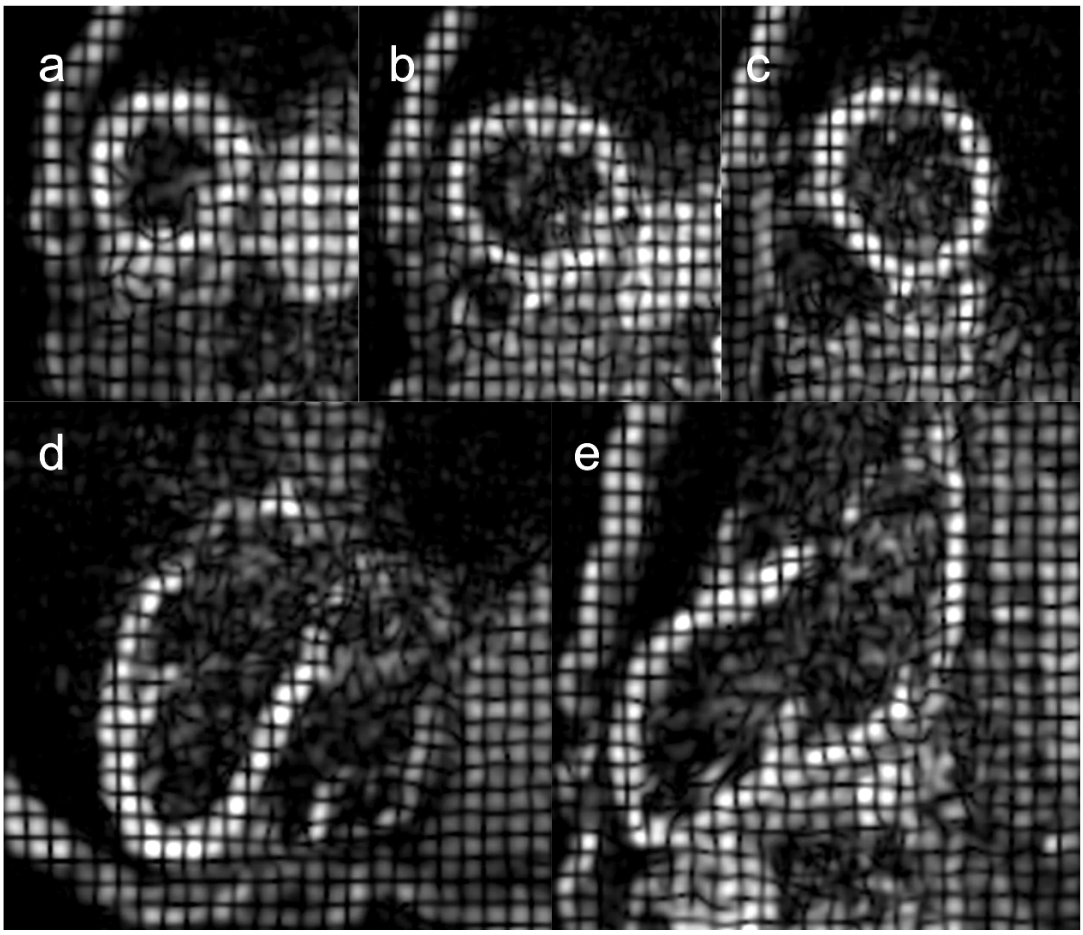

Figure 4.2: Typical CSPAMM images; (a) apical short axis, (b) mid ventricle short axis, (c) basal short axis, (d) 2-chamber long axis, (e) 4- chamber long axis acquired for the study.

4.2 CMR feature-tracking for the assessment of deformation parameters

Feature tracking is a post-processing technique that can be used to analyse cine CMR images.

The endocardial and epicardial borders of the left ventricle are manually traced at the end diastolic phase. Then, the software algorithms track the anatomical features such as epicardial and endocardial borders and myocardial tissue as well as the edges between the tissue-blood pool cavities over time by searching the maximum likelihood displacement

of those features over a local neighbourhood in the successive frames (3).

The motion of those features will be tracked throughout the cardiac cycle. The derived deformation and motion parameters obtained from left ventricular myocardium are: displacement, velocity, strain and strain rate for each software used in this thesis are shown in Table 4.1. These parameters can be measured for both the epicardial and endocardial contours at a global level for the whole LV, measured at the basal, mid, and apical short axes, and 2 chamber and 4 chamber long axes, or they can be measured at the regional level (myocardial segments).

4.2.1 Tomtec

Tomtec (Tomtec MR FT analysis, Version 4.6, Build 4.6.2.12, TomTec Imaging Systems, Munich, Germany) was the first software available for CMR feature tracking and has thus been used in a majority of research studies published to date. The first published study applied Tomtec feature tracing analysis to a population of 191 Duchenne muscular dystrophy patients (8). In this thesis, Tomtec was used to analyse the short axis (basal, mid and apical levels), two-chamber and four-chamber long axes images in chapter 5.

The software is relatively easy to use; following the labelling of the view or orientation of the cine images, contour points need to be placed on the endocardial and epicardial borders of the initial frame corresponding to the end diastolic phase. These points manually delineate the endocardial and epicardial borders. It is also important to mark the upper septal insertion point between the left ventricle and right ventricle short axis to allow for accurate segmentation; segmental results based on a 16-segment or 17-segment model may be selected (3).

Table 4.1: Deformation parameters that can be derived from each feature tracking and tagging software package. Radial parameters can be calculated for both short and long axis, whereas circumferential only applies to short axis and longitudinal to long axis views.

Parameters			Tomtec	CVI42	CIM-FT	CIMTag2D	Comment
Displacement (mm)	**Global**	Radial		✓			Distance between instantaneous and initial (often at the end diastole) position of a myocardial segment (72)
		Circumferential		✓			
		Longitudinal		✓			
	Endo	Radial	✓	✓			
		Circumferential	✓	✓			
		Longitudinal	✓	✓			
	Epi	Radial	✓	✓			
		Circumferential	✓	✓			
		Longitudinal	✓	✓			
Velocity ($mm.s^{-1}$)	**Global**	Radial		✓			Accuracy is highly frame-rate dependent.
		Circumferential		✓			
		Longitudinal		✓			
	Endo	Radial	✓	✓			
		Circumferential	✓	✓			
		Longitudinal	✓	✓			
	Epi	Radial	✓	✓			
		Circumferential	✓	✓			
		Longitudinal	✓	✓			
Strain (%)	**Global**	Radial	✓	✓	✓	✓	Change in the length of myocardial fibre within a specific direction relative to its initial length (often at the end diastole) Accuracy is highly frame-rate dependent.
		Circumferential		✓	✓	✓	
		Longitudinal		✓	✓	✓	
	Endo	Radial		✓	✓	✓	
		Circumferential	✓	✓	✓	✓	
		Longitudinal	✓	✓	✓	✓	
	Epi	Radial		✓	✓	✓	
		Circumferential	✓	✓	✓	✓	
		Longitudinal	✓	✓	✓	✓	
Strain rate (s^{-1})	**Global**	Radial	✓	✓	✓	✓	
		Circumferential		✓	✓	✓	
		Longitudinal		✓	✓	✓	
	Endo	Radial		✓	✓	✓	
		Circumferential	✓	✓	✓	✓	
		Longitudinal	✓	✓	✓	✓	
	Epi	Radial		✓	✓	✓	
		Circumferential	✓	✓	✓	✓	
		Longitudinal	✓	✓	✓	✓	

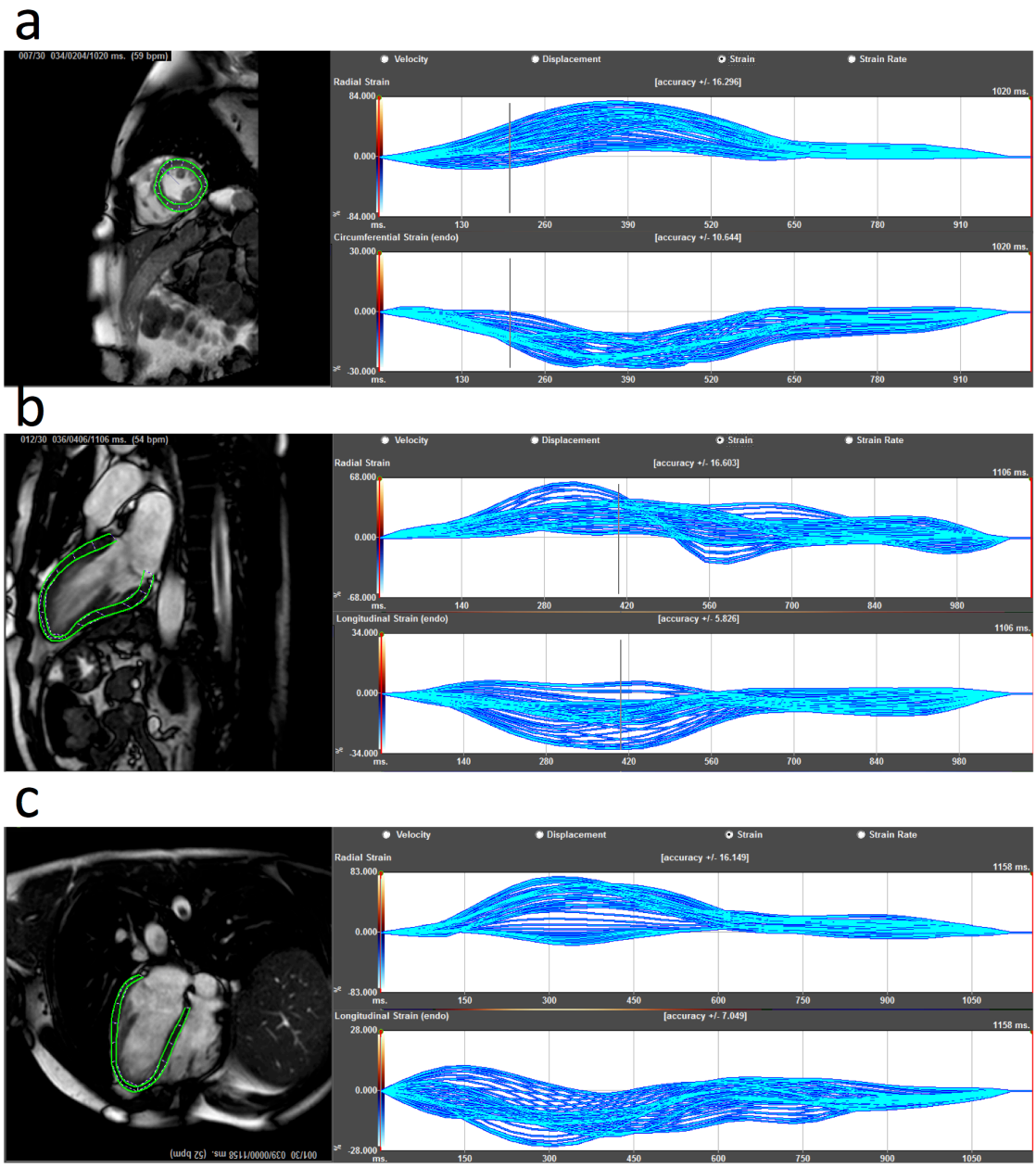

Figure 4.3: Example of FT analysis using Tomtec. Endocardial and epicardial contours of the LV are drawn on one frame and propagated throughout the cardiac cycle. (a) A short axis slice with endocardial and epicardial contours (left-hand side), and the corresponding radial (upper right-hand side) and circumferential strains (lower right-hand side). (b) A 2-chamber view with endocardial and epicardial contours (left-hand side), with corresponding radial (upper right-hand side) and longitudinal strains (lower right-hand side). (c) A 4-chamber view with endocardial and epicardial contours (left-hand side), and the corresponding radial (upper right-hand side) and longitudinal strains (lower right-hand side). Other deformation parameters such as velocity, displacement and strain rates can be calculated.

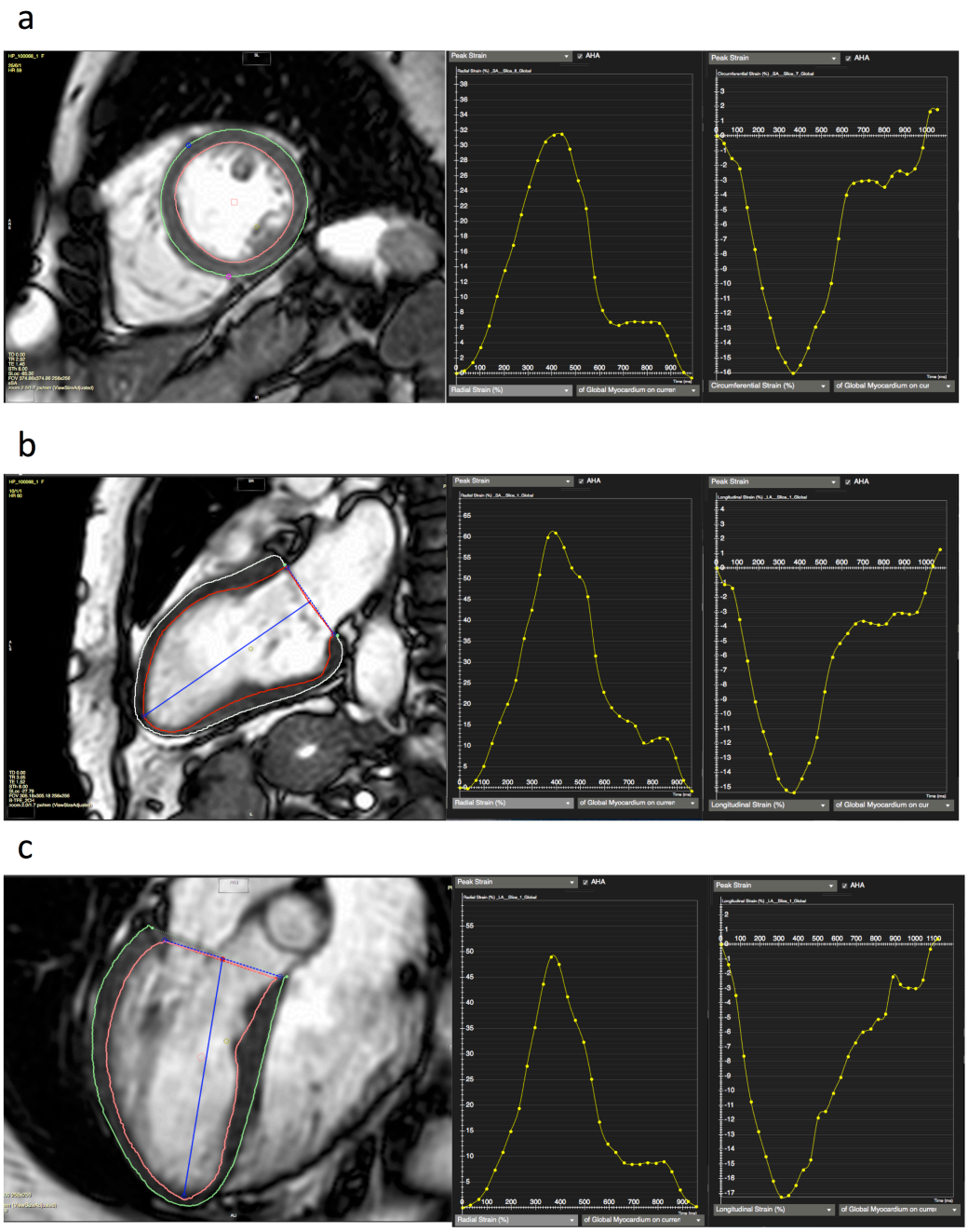

Figure 4.4: Example of CVI42 FT analysis. The software semi-automatically defines the endocardial (red contour) and epicardial (green contour) LV contours throughout the cardiac cycle. (a) A short axis slice with delineated endocardial and epicardial contours (left-hand side) and the corresponding radial (middle) and circumferential strains (right-hand side). (b) A 2-chamber long axis slice with delineated endocardial and epicardial contours (left-hand side) and the corresponding radial (middle) and longitudinal strains (right hand side). (c) A 4-chamber long axis slice with delineated endocardial and epicardial contours (left hand side) and the corresponding radial (middle) and longitudinal strains (right hand side). Additional calculated parameters include velocity, displacement and strain rates.

The initial contours are automatically tracked across the following time frames by the software, which then allows the myocardial deformation parameters to be computed. The contours can be visually checked in all cardiac phases, and in case of incorrectly tracked contours, the initial frame can be manually adjusted and re-propagated when necessary; an example is shown in Figure 4.3.

4.2.2 CVI42

CVI42 (release 5.1.1, Circle Cardiovascular Imaging Inc. Calgary, Canada) tissue tracking software was used in the first study published comparing Tomtec to another clinical software (73).

This software can use cine CMR images in the (apical, mid and basal level) short axis, two-chamber and four-chamber long axis to calculate strain parameters.

In order to obtain an accurate segmentation, reference points need to be positioned at the superior and inferior insertion points of the right ventricle on the short-axis images. The LV endocardial and epicardial contours are traced by placing a series of points on the endocardial and epicardial borders; these contours are delineated on the end-diastolic cardiac phase, usually the initial frame of the short axis and long axis cine images. Those points are then tracked by the software using the tissue tracking module over the entire cardiac cycle. Deformation parameters for both short and long axes can be computed and all cardiac motion and strain parameters can be exported as a text file or as an XML file format. Figure 4.4 illustrates part of the analysis process using CVI42.

4.2.3 CIM-FT

The software CIM-FT (version v.8.1.2, CIM-FT, Auckland MRI Research Group, New Zealand) is a non-commercial software that requires a research agreement with the providing institution.

Before analysis, each cine series has to be labelled as either a short-axis (mid, basal or apical slices) or as a long axis cardiac view. First, contours for short axis or long axis have to be drawn on the first frame, typically corresponding to the end diastolic phase. Guide points can be used to achieve the best possible fit of the initial epicardial and endocardial contours to the myocardial borders. Then, the right ventricle superior and inferior insertion points have to be identified and positioned on each short axis slice. It is best to do this on the end-systolic phase, when the blood pool is at its minimum and myocardial tissue is at its maximum thickness. The feature tracking mode is then selected and the epicardial and endocardial borders are tracked automatically. The resulting tracked contours are displayed for all cardiac phases, and the user in able to make manual contour adjustments in all of subsequent frames when needed in order to obtain the best possible tracking results. Finally, cardiac motion parameters are computed throughout the cardiac cycle; an example is displayed in Figure 4.5.

4.3 Analysis of CMR-tagging for the assessment of deformation parameters using CIMTag2D

The CMR-tagged images can be used to quantify myocardial regional deformation parameters by tracking non-invasive markers that are created in the myocardium tissue, referred to as ‘tags’. Tags are created within myocardial tissue via spatially selective radiofrequency saturation to generate regions of low signal intensity, which appear as dark lines in the acquired images (see chapter 2 section 2.7.2).

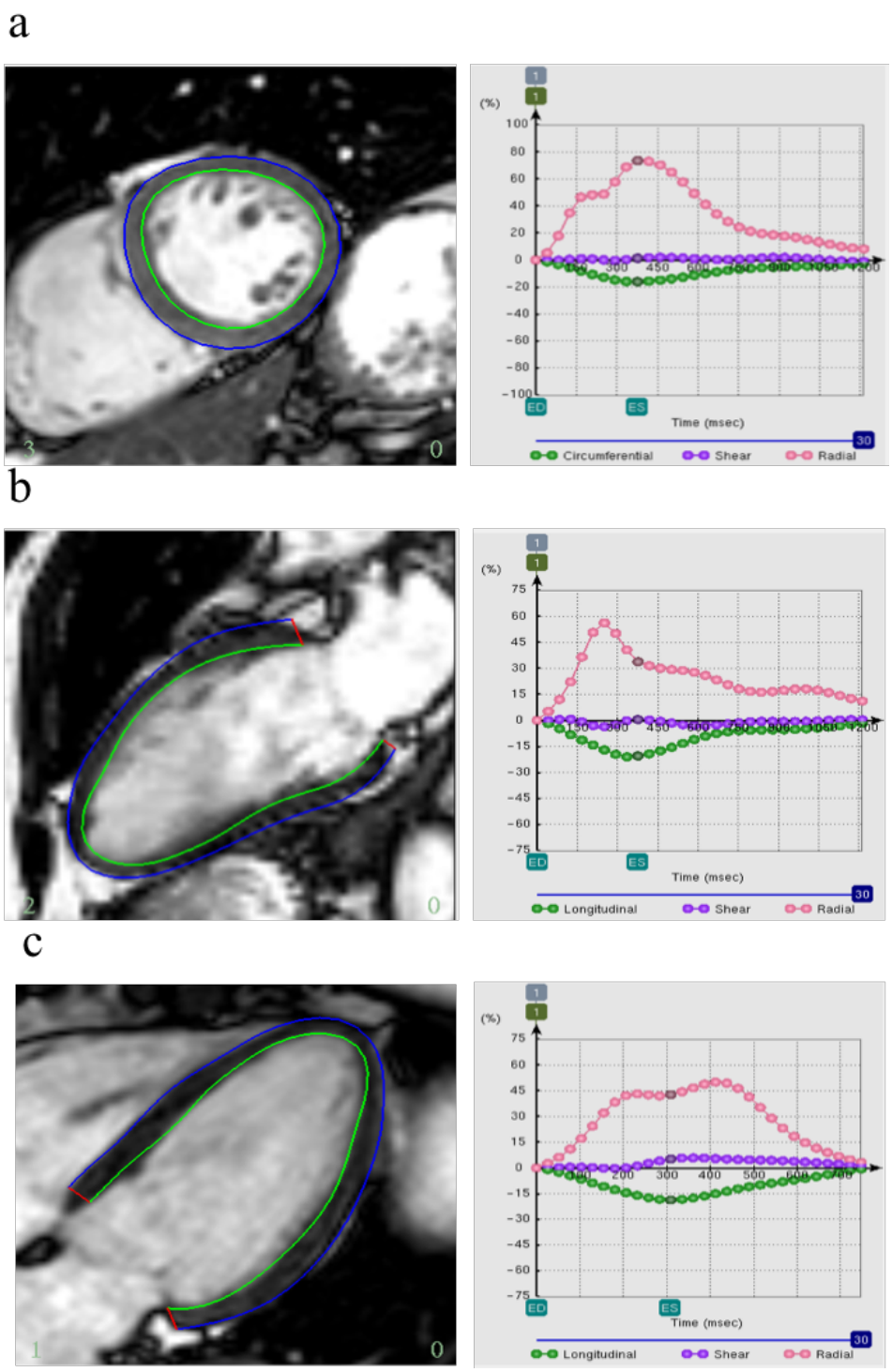

Figure 4.5: Example of CIM-FT analysis. Endocardial and epicardial contours of the LV are drawn on one frame and propagated throughout the cardiac cycle. (a) A short axis slice with delineated endocardial and epicardial contours (left hand side), and (right hand side) the corresponding radial, circumferential strain and shear. (b) A 2-chamber slice with delineated endocardial and epicardial contours (left hand side) and with corresponding radial, longitudinal strain and shear (right hand side). (c) A 4-chamber slice with delineated endocardial and epicardial contours (left hand side) and with corresponding radial, longitudinal strain and shear (right hand side).

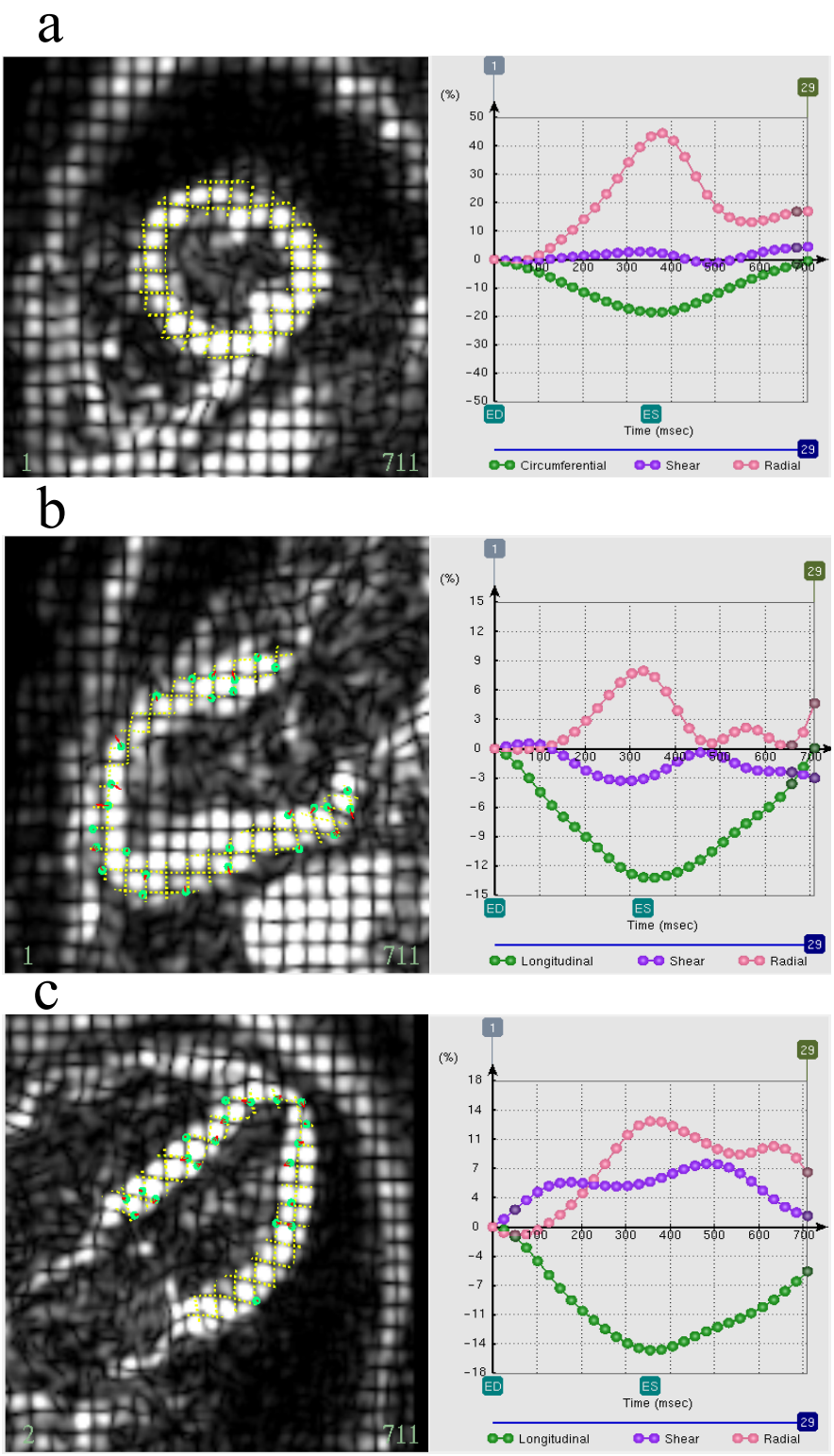

Figure 4.6: Example of tagging analysis-using CIMTag2D. Endocardial and epicardial contours of the LV are drawn on one frame and propagated throughout the cardiac cycle. (a) A short axis slice with the deformation tagging grid (left hand side), and (right hand side) the corresponding radial, circumferential strain and shear. (b) A 2-chamber view with the deformation tagging grid (left hand side), with corresponding radial, longitudinal strain and shear (right hand side). (c) A 4-chamber view with the deformation tagging grid (left hand side), with corresponding radial, longitudinal strain and shear (right hand side).

These created lines deform with cardiac contraction and therefore, by tracking their deformation throughout the cardiac cycle, the myocardial deformation parameters can be computed. In chapter 6, tagged images were analysed using CIMTag2D software (version 8.1.5, Cardiac Image Modelling, University of Auckland, Auckland, New Zealand). CIMTag2D was used as an established or reference method (8) and has been previously be used for comparative studies with feature tracking (30)(45). In CIMTag2D, the short and long axes of the CMR-tagged images first need to be specified. Then, the grid model geometry requires to be initialised on the first frame, usually the end diastolic phase for the short- and long axes cine images. The step thereafter is achieved by using guide-points, where the model grid is aligned manually to the myocardial tagging grid; these grid points can be adjusted by the user throughout consecutive frames.

The left ventricular endocardial and epicardial contours can be adjusted using the guide points when necessary. The right ventricular superior and inferior points also need to be defined. Additionally, the software requires the end-systolic phase to be identified when the blood pool is at its minimal area, and myocardial tissue is at its maximal thickness. The software motion tracking mode can then be selected to follow the deformation of the grid tags throughout the cardiac cycle. Afterwards, adjustments to the tracked grid control points can be made in all cardiac frames when needed to improve the quality of the tracking; an example of analysis with CIMTag2D is shown on Figure 4.6.

4.4 FT Software optimisation and standardization

“All the software used in the thesis are available to our group (Cardiovascular Imaging, Barts Health/QMUL) and are subject to constant analysis optimisation and standardization (see section 4.4).

4.4.1 Personal Work

In order to gain sufficient experience, I first practised using each software package on available data. I compared the strain values in the extracted text file every time I repeated the analysis, until I gained full confidence in the analysis process and my results showed little to no variability. I also compared my results with other users. As part of the studies in chapter 5 and 6, my analysis was compared against the most experienced user in our group.

Each software has its standard operating procedure (SOP), which was provided by the company or research group. This allowed us to follow a clear step by step process on how to draw the endocardial and epicardial contours and extract the strain results as applied to all software packages: Tomtec, CVI42, CIM-FT and CIMTag2D. Those SOPs are updated and adapted by the group (see next section).

CIM-FT and CIMTag2D software packages were provided by Auckland MRI Research Group. To start with, CIM-FT showed high sensitivity to contour drawing, and as a result, the peak strain values could jump from 30-40% to 2000%. Consequently, I raised this issue with the Auckland group that developed the software. As a result, they changed their SOP and advised to only modify the contours on the diastolic phase (first frame) and systolic phase without modifying the contours on the rest of the frame.

As part of the study in chapter 5, I also tried to analyse the tagged SPAMM data for the 26 hypertensive patients. However, the fading of the tagging grids in the systolic phases did not allow for reliable analysis and consequently, I did not analyse the full data set and did not include those results. As the HAPPY London data included CSPAMM imaging, with no fading of tagged lines through the cardiac cycle, the analysis was easier and more

reproducible and consequently the analysis forms part of Chapter 6.

4.4.2 Group Standardisation

As part of the group effort to standardise analysis and minimise intra and inter-observer variabilities, local SOPs have been put in place for the different software. The most commonly used software in the group is CVI42 and the standardisation of analysis has been mainly based on the experience using this software. The standardisation has been applied to short axis, 2-chamber and 4-chamber views. For short axis left ventricular function, only slices where 50% of the myocardium tissue is displayed are included; CVI42 allows for open and closed contours.

Contours are always drawn on the first frame (end-diastolic frame when the volume is at its maximum), and the systolic frame. Those frames are first identified by going through all frames to look for the minimum and maximum left ventricle volumes.

It was also decided not to include the papillary muscle in short axis, 2-chamber and 4-chamber long axes to allow calculating the strain for myocardial tissue and to allow comparison across our groups."

4.5 General statistical analysis

Statistical analysis was performed using IBM SPSS Statistics version 23. All deformation parameters measured by all software packages were first assessed by the Shapiro-Wilk test to check for normality of the distribution, the criterion for significance was $p < 0.05$. Non-normally distributed variables were tested using non-parametric methods (Friedman), but the intra-class correlation (ICC) which requires a normal distribution was not calculated for these variables. The difference between distributions when using two or more methods for the same observation can be assessed using the Friedman test (74).

The Friedman test was used as it does not make any assumption about the distribution, so it can be applied to all variables including non-normally distributed variables. Friedman test is not applied to the measurements themselves, but ranks the methods from the lowest to highest value in each row (each observation) and compares the total ranks for those variables across the methods. As the Friedman test was applied to a large number of variables, Bonferroni adjustment was used as a multiple test procedure (75). The significance level was adjusted according to Bonferroni with $p<0.05$ divided by n, where n is the total number of comparisons made.

Intra-observer variability was assessed when the same observer repeats the same measurements by using the same technique on the same subjects after a short period of time. Inter-observer variability can be assessed when two different observers measure the same parameters by using the same technique on the same subject. The two observers who did the measurements on the same population are Haifa Almutairi, the author of the thesis, and José Miguel Paiva, a radiographer with 2.5 years' experience (analysing >5000 cases). Each observer made strain measurements using Tomtec, CVI42, CIM-FT and CIMT2D at different time points.

Bland-Altman statistics, with a calculation of 95% limits of agreement were applied to assess the agreement between two software packages' results, and to assess the agreement for inter- and intra-observer measurements (76). It is a method to visualise the data graphically in order to evaluate the range within which it is expected discrepancies between the methods to lie as well as any bias between the methods as shown by a mean difference between both measurements that differs from zero. The difference between the means of two measurements shows the bias from zero, and the limits of agreement are calculated as mean ± 1.96 SD. SD is the standard deviation of differences which represents the distribution of how far the observations differ from the mean. Paired t-tests

were used to test whether the bias in the results generated from the software packages and between and within observers was significantly different from zero.

Agreement between methods or raters can also be assessed using the ICC as a measure of reliability (77). However, ICC can only be applied for variables that are normally distributed and so this method has not been used for the non-normally distributed variables derived from all software packages. The intra-class correlation coefficient (consistency and absolute agreement) was assessed. Absolute agreement evaluated whether the three software types provided the same results; ICC (absolute agreement) will be low if there is low correlation between the software results or if there are relevant differences in means between the strain measures derived from different software packages i.e. if one software gives consistently higher results than another. Consistency ICC considers whether the software packages rank the values consistently. If the consistency ICC is higher than the absolute ICC this suggests that the methods may give good agreement if the bias between means could be adjusted for (77).

Box plots were used for visual comparison between global and regional deformation parameters across all software packages in healthy subjects and hypertensive patients as well as between male and female, and between healthy subjects and hypertensive patients. Comparisons allow commenting on the distribution, median, range (between the maximum and minimum values) and the interquartile range (IQR), which is the box width for the measurements. The independent sample t-test is a test to compare means between two unrelated groups for the same dependent continuous variable and was used to test for differences between males and females, hypertensive and non-hypertensive subjects and non-diabetic and diabetic subjects. To compare two continuous variables Spearman's correlation coefficient was used. It ranks the order of the measurements for n observations, and measures the strength and direction of the correlation between the

ranks. Spearman correlation can be used for both normal and non-normally distributed variables and was used to test the association of systolic and diastolic blood pressure with the deformation parameters. The statistician Jackie Cooper who provided me with statistics advise on all the analysis that I run.

Chapter 5: Comparison of feature tracking software packages in hypertensive patients and healthy subjects

5.1 Introduction

CMR-feature tracking allows the assessment of global and regional deformation parameters of the left ventricle, thus potentially offering useful clinical information (3). Myocardial deformation parameters have been used to detect early left ventricular contractile dysfunction in some CVD (51)(55). Previous studies have applied FT to normal subjects and reported reference strain values that can be used when comparing healthy and CVD strain results. Despite the potential of the technique in early diagnosis of cardiac pathology, it is yet to be implemented in routine clinical CMR, due to high variability in reported results when compared to other modalities such as CMR-tagging and echocardiography.

In this chapter, three FT software packages were used to analyse SSFP cine CMR images both of healthy subjects and hypertensive patients in order to assess the agreement in global and regional cardiac deformation parameters between the three software packages. The chapter also evaluated the inter- and intra-observer variability of those three FT software packages. All the data that was included in chapter 5 are pre-existing data at our

unit, which was run by other colleagues, 26 hypertensive patients (in Chapter 5) from The Heart Hospital, while 28 healthy subjects from HAPPY London study (9). Finally, the results for health subjects and hypertensive patients were compared for each software. Both datasets were acquired at different imaging centers using different MRI scanners, acquisition parameters and spatial and temporal resolutions, which is expected to have an impact on the derived results.

5.2 Methods

Twenty-eight (28) healthy subjects and twenty-six (26) hypertensive patients underwent different standardised CMR scan at different centers (71). The CMR cine acquisition protocol for SSFP for healthy subjects and hypertensive patients are presented in chapter 4 (4.1.1).

LV systolic deformation parameters were obtained by analysing cine CMR images using three different FT software packages: Tomtec = MR FT analysis (TomTec Imaging Systems, Munich, Germany), CVI42 (Circle Cardiovascular Imaging Inc. Calgary, Canada), and CIM-FT (CIM-FT, Auckland MRI Research Group, New Zealand) (see section 4). Inter- and intra-observer variability were assessed in ten healthy subjects; CMR images were re-analysed by the author of this dissertation for intra-observer variability and analysed by an experienced second observer, José Miguel Paiva, a radiographer with 2.5 years' experience (analysing >5000 cases), to evaluate inter-observer variability.

5.2.1 Study Population

All 28 healthy subjects that were recruited in the HAPPY London study had no previous angina or myocardial infarction, no history of stroke or transient ischaemic attack (TIA), or any Cardiac sounding chest pain requiring further investigations. Other than vascular disease, healthy subjects had no medical history of diabetes, were not on hypertension treatment and had no history of overt cardiac disease(9). The 26 hypertensive patients were prospectively recruited from a tertiary hypertension clinic and enrolled to undergo CMR examinations. Table 5.1 illustrates the demographic variables for the healthy subjects and hypertensive patients. Both groups were not matched for gender and age. Diastolic and systolic BP and the ejection fraction were also not matched as those parameters are affected by hypertension.

5.2.2 Statistical analysis

IBM SPSS Statistics version 23 was used for conducting statistical tests. All LV deformation parameters are presented as mean ± standard deviation (SD). Differences in the distribution of variables between software packages were tested using a paired non-parametric method, Friedman test, that can be applied to normal and non-normal distributed variables. A Bonferroni adjustment was applied to take multiple testing into account; 20 comparisons in Table 5.2 and 5.3, therefore $p=0.05/20$ thus, a $p<0.003$ was considered to highlight a statistically significant difference (75).

The inter- and intra-observer variability for deformation parameters (global, endocardial and epicardial strains) were assessed using the Bland-Altman approach, with a calculation of the 95% limits of agreement (76). The p-value for inter- and intra-observers were calculated for all deformation parameters to examine any significant bias between inter-

and intra-measurements. The significance level after Bonferroni adjustment was taken as $p<0.002$ (30 comparisons, $p<0.05/30$) for CVI42 and CIM-FT and $p<0.003$, (20 comparisons, $p<0.05/20$) for Tomtec.

Table 5.1: Demographic details for healthy subjects and hypertensive patients. Red cell = significant difference ($p<0.05$).

Parameters	Healthy subjects	Hypertensive Patients
Female / Male	8 / 20	11 / 15
Age (years)	66.2 ± 5.3	53.5± 15.6
Height (m)	1.74 ± 0.10	1.69± 0.11
Weight (kg)	80.8 ± 11.4	81.6± 14.9
BMI (kg/m2)	26.8 ± 3.1	28.2± 4.3
BSA (m2)	1.97 ± 0.18	1.96± 0.22
Systolic BP (mmHg)	125.9 ± 8.6	150.6± 17.8
Diastolic BP (mmHg)	77.1 ± 6.5	88.2± 8.9
LV ejection fraction (%)	62.1 ± 6.0	71.8± 7.5

BMI=body mass index, BSA = Body surface area, BP=blood pressure, LV-EF= Left Ventricle ejection fraction.

Normality for all variables measured by FT software packages was determined using the Shapiro-Wilk test. All derived deformation parameters were normally distributed, except for the radial strain derived from the short axis and long axis using CIM-FT software. Intra-class correlation coefficient (ICC), the two-way mixed model for absolute agreement and consistency was computed for all derived variables with normal distributions to assess agreement as shown in Table 5.4. Absolute agreement evaluated whether the three software provided the same results; ICC (absolute agreement) is low for a high bias between mean differences. In this instance, consistency considers whether the software packages rank the values consistently but is not affected by differences in means. Based on ICC, the results were categorised for agreement and consistency as follows: $ICC\leq0.4$, poor; $0.4<ICC\leq0.6$, fair; $0.6<ICC\leq0.75$, good; $ICC>0.75$, excellent

(78)(77). Box plots were used to compare between deformation parameters across the three FT software packages in healthy subjects and hypertensive patients.

5.3 Results

5.3.1 Comparison between software packages

The global, endocardial and epicardial circumferential, radial and longitudinal strain means are given in Tables 5.2 (healthy) and 5.3 (hypertensive). The Friedman test showed significant differences in most parameters across the three FT software packages in healthy subjects as shown in Table 5.2. However, there were agreements for six parameters: global and endocardial circumferential strain for apical short axis, global circumferential strain for mid ventricle short axis, global radial strain for 2-chamber and 4-chamber and for endocardial longitudinal strain for 2-chamber. The Friedman test also demonstrated significant differences across all FT software packages in hypertensive patients as shown in Table 5.3. However, there were also agreements for nine parameters: endocardial circumferential strain for apical, mid and basal ventricle short axes, as well as global circumferential strain for apical short axis. Global and endocardial longitudinal strain for 2-chamber as well as global, endocardial and epicardial longitudinal strain for 4-chamber.

All circumferential and longitudinal strains showed low standard deviations (narrow distribution) across all software packages in healthy and hypertensive patients, indicating low variation between observations (Tables 5.2 and 5.3). While global, endocardial and epicardial radial strains, in particular in short axis views, showed larger standard deviation in particular for CIM-FT in hypertensive patients (Table 5.3).

ICC results were calculated for normal distributed parameters derived from all FT

software packages in healthy subjects and patients (Table 5.4). Overall, software performed slightly better in patients than in volunteers. Consistency was good or excellent in 10/17 parameters in healthy subjects and 15/17 in patients. The most consistent parameters across the two populations were circumferential strains from mid-short axis (excellent) followed by circumferential strains from apical short axis and longitudinal strain from 2-chamber long axis, both good. Circumferential strain from the basal short axis were both excellent in the hypertensive population but only poor to fair in the healthy population. Radial strain, especially from the mid-short axis slice was the worst performer across the two populations.

Table 5.2: Summary of the strain values (mean ± standard deviation) in the healthy population calculated by the different software. Tomtec only calculate global radial strain values. Red cell = significant difference (p<0.003) between the three software.

Strain (%)		Tomtec			CVI42			CIM-FT			Friedman test		
		Global	**Endo**	**Epi**	**Global**	**Endo**	**Epi**	**Global**	**Endo**	**Epi**	**Global**	**Endo**	**Epi**
Circumferential	Basal-SAX	-15.42 ±3.01	-19.79 ±3.44	-11.12 ±3.09	-24.44 ±3.63	-26.33 ±3.85	-22.15 ±3.18	-16.85 ±2.41	-19.27 ±2.55	-14.57 ±2.56	0.000	0.000	0.000
	Mid-SAX	-13.77 ±2.69	-17.86 ±3.29	-9.78 ±2.57	-19.40 ±2.63	-20.82 ±2.72	-18.03 ±2.67	14.96 ±2.26	-17.30 ±2.44	-12.69 ±2.22	0.06	0.000	0.000
	Apical-SAX	-17.01 ±4.07	-20.88 ±4.23	-13.25 ±4.42	-19.49 ±3.20	-21.18 ±3.36	-17.87 ±3.32	-18.48 ±4.87	-21.57 ±5.06	-15.59 ±4.85	0.12	0.78	0.000
Radial	Basal-SAX	36.14 ±7.43	NA	NA	52.19 ±19.37	60.87 ±23.46	41.77 ±11.27	49.34 ±13.75	50.18 ±14.14	48.49 ±13.66	0.000	NA	NA
	Mid-SAX	38.43 ±12.67	NA	NA	33.88 ±7.87	38.21 ±8.82	30.03 ±7.34	52.20 ±15.39	53.76 ±15.04	51.06 ±15.97	0.000	NA	NA
	Apical-SAX	31.14 ±10.55	NA	NA	38.49 ±10.80	44.84 ±13.27	33.35 ±9.64	52.73 ±15.74	57.48 ±16.05	49.21 ±15.99	0.000	NA	NA
	2ch-LAX	39.07 ±13.91	NA	NA	33.58 ±8.84	33.93 ±10.05	33.82 ±8.32	40.72 ±13.43	41.16 ±14.22	40.15 ±13.25	0.04	NA	NA
	4ch-LAX	31.39 ±6.35	NA	NA	35.95 ±7.63	37.09 ±8.74	37.41 ±8.80	36.02 ±14.02	36.84 ±14.43	34.86 ±13.15	0.13	NA	NA
Longitudinal	2ch-LAX	-15.51 ±3.22	-18.48 ±3.87	-12.59 ±3.49	-18.12 ±2.38	-18.17 ±2.44	-18.38 ±2.44	-16.98 ±2.43	-17.25 ±2.46	-16.63 ±2.46	0.000	0.01	0.000
	4ch-LAX	-16.80 ±3.49	-19.52 ±4.19	-14.2 3±3.69	-18.55 ±2.22	-18.74 ±2.34	-19.23 ±2.54	-15.65 ±1.73	-15.9 7±1.93	-15.25 ±1.63	0.000	0.000	0.000

Endo = endocardial, Epi= epicardial, SAX = short axis, LAX = long axis, 2ch = 2 chamber, 4ch =4 chamber, NA = not available.

Table 5.3: Summary of the strain values (mean ± standard deviation) in the hypertensive population calculated by the different software. Tomtec only calculate global radial strain values. Red cell = significant difference (p<0.003) between the three software.

Strain (%)		Tomtec			CVI42			CIM-FT			Friedman p-value		
		Global	**Endo**	**Epi**	**Global**	**Endo**	**Epi**	**Global**	**Endo**	**Epi**	**Global**	**Endo**	**Epi**
Circumferential	Basal SAX	-19.53 ±4.26	-25.25 ±4.84	-13.82 ±4.30	-25.82 ±4.45	-28.43 ±4.76	-22.89 ±3.89	-18.82 ±3.03	-23.86 ±3.87	-14.09 ±2.69	0.000	0.011	0.000
	Mid SAX	-18.33 ±4.23	-23.5 7±5.67	-13.12 ±3.59	-20.66 ±4.24	-22.92 ±4.60	-18.43 ±3.96	-17.13 ±2.91	-22.87 ±4.02	-11.51 ±2.35	0.000	0.30	0.000
	Apical SAX	-20.20 ±4.43	-25.24 ±5.83	-15.19 ±5.83	-19.96 ±3.56	-22.19 ±4.02	-17.66 ±3.15	-19.61 ±4.28	-26.06 ±5.29	-13.60 ±3.56	0.45	0.01	0.000
Radial	Basal SAX	36.66 ±8.42	NA	NA	59.65 ±20.09	73.6 3±26.55	44.81 ±12.48	69.40 ±27.57	79.41 ±37.88	68.12 ±32.91	0.000	NA	NA
	Mid SAX	36.13 ±14.59	NA	NA	39.00 ±13.32	47.28 ±17.42	31.77 ±10.35	94.90 ±38.30	119.98 ±73.72	85.34 ±36.16	0.000	NA	NA
	Apical SAX	26.13 ±14.24	NA	NA	40.44 ±10.89	49.49 ±14.22	33.01 ±8.15	92.84 ±45.59	115.54 ±65.05	86.19 ±44.21	0.000	NA	NA
	2ch LAX	36.01 ±11.01	NA	NA	33.81 ±6.91	34.24 ±7.05	33.49 ±7.48	63.13 ±21.84	66.66 ±22.66	59.19 ±20.67	0.000	NA	NA
	4ch LAX	27.92 ±8.09	NA	NA	37.28 ±10.59	38.63 ±11.02	38.06 ±11.42	55.89 ±24.41	59.35 ±26.98	51.76 ±21.68	0.000	NA	NA
Longitudinal	2ch LAX	-16.73 ±4.64	-19.38 ±5.07	-14.15 ±4.42	-18.97 ±2.25	-19.13 ±2.35	-18.86 ±2.39	-18.83 ±3.46	-19.86 ±3.44	-17.69 ±3.66	0.01	0.96	0.000
	4ch LAX	-19.19 ±5.17	-20.43 ±5.56	-18.01 ±4.95	-19.07 ±3.33	-19.54 ±3.31	-19.03 ±3.49	-17.89 ±2.89	-18.76 ±2.73	-16.89 ±3.35	0.05	0.11	0.04

Endo = endocardial, Epi= epicardial, SAX = short axis, LAX = long axis, 2ch = 2 chamber, 4ch =4 chamber, NA = not available.

Table 5.4: Intra-class correlation coefficient (ICC) results for consistency and absolute agreement for normal distributed variables derived by Tomtec, CVI42 and CIM-FT, in healthy subjects and hypertensive patients.

Strain (%)			Consistency		Absolute agreement	
			Healthy	Hypertensive	Healthy	Hypertensive
Circumferential	Apical SAX	Global	0.64	0.70	0.61	0.71
		Endo	0.63	0.67	0.69	0.62
		Epi	0.61	0.75	0.53	0.65
	Mid SAX	Global	0.82	0.93	0.51	0.86
		Endo	0.76	0.93	0.63	0.93
		Epi	0.82	0.88	0.36	0.59
	Basal SAX	Global	0.45	0.84	0.16	0.59
		Endo	0.36	0.83	0.18	0.75
		Epi	0.55	0.79	0.17	0.41
Radial	Apical SAX	Global	0.68	0.33	0.48	0.15
	Mid SAX	Global	0.49	0.55	0.36	0.26
Longitudinal	2ch LAX	Global	0.73	0.72	0.65	0.68
		Endo	0.69	0.71	0.68	0.71
		Epi	0.63	0.67	0.39	0.53
	4ch LAX	Global	0.54	0.82	0.45	0.82
		Endo	0.52	0.79	0.42	0.78
		Epi	0.42	0.81	0.26	0.79

Endo = endocardial, Epi= epicardial, SAX = short axis, LAX = long axis, 2ch = 2 chamber, 4ch =4 chamber.

Absolute agreement was not as good as consistency for the two populations, with only 5/17 parameters rated good in the healthy population and 11/17 good or excellent in the hypertensive population. For global parameters, circumferential strain from the apical short axis slice and longitudinal from the 2-chamber long axis were the most consistent across populations (good), while circumferential strain from the basal short axis slice and radial strains were the worst (poor to fair). Notably, the absolute agreements for circumferential strain from the mid-short axis slice and longitudinal strain from the 4-chamber view were excellent in the patient population while it was only fair in the healthy population.

The three FT software packages were also compared against each other in both healthy subjects and hypertensive patients. In healthy subjects and hypertensive patients, global circumferential strain calculated from mid ventricle and basal short axis by CVI42 were lower than the value obtained by Tomtec and CIM-FT, see also in Figure 5.1 B-C. There were statistically significant differences for mid and basal short axis across the three software packages in both groups. However, there was no statistically significant difference for apical short axis in hypertensive patients, while its statistically significant in healthy subjects across the three software packages (see also Figure 5.1 A).

Global longitudinal strain results for 4-chamber did not differ significantly between the software packages for hypertensive patients, while they differ significantly for healthy subjects. Tomtec software results for 2-chamber and 4-chamber longitudinal strain results were higher in both healthy subjects and hypertensive patients compare to CVI42 and CIM-FT results, see also Figure 5.2 A-B. Finally, measurements derived by Tomtec showed higher variability than CVI42 and CIM-FT in healthy subjects (Figure 5.2 A-B).

The global radial strain parameters derived from the three FT software packages showed statistically significant differences in both groups for apical, mid and basal short axis as well as 2-chamber and 4-chamber, however the only parameter that not differ significantly between the software packages in healthy subjects is global radial strain for 4-chamber ($P = 0.13$) (Figure 5.5 A-E).

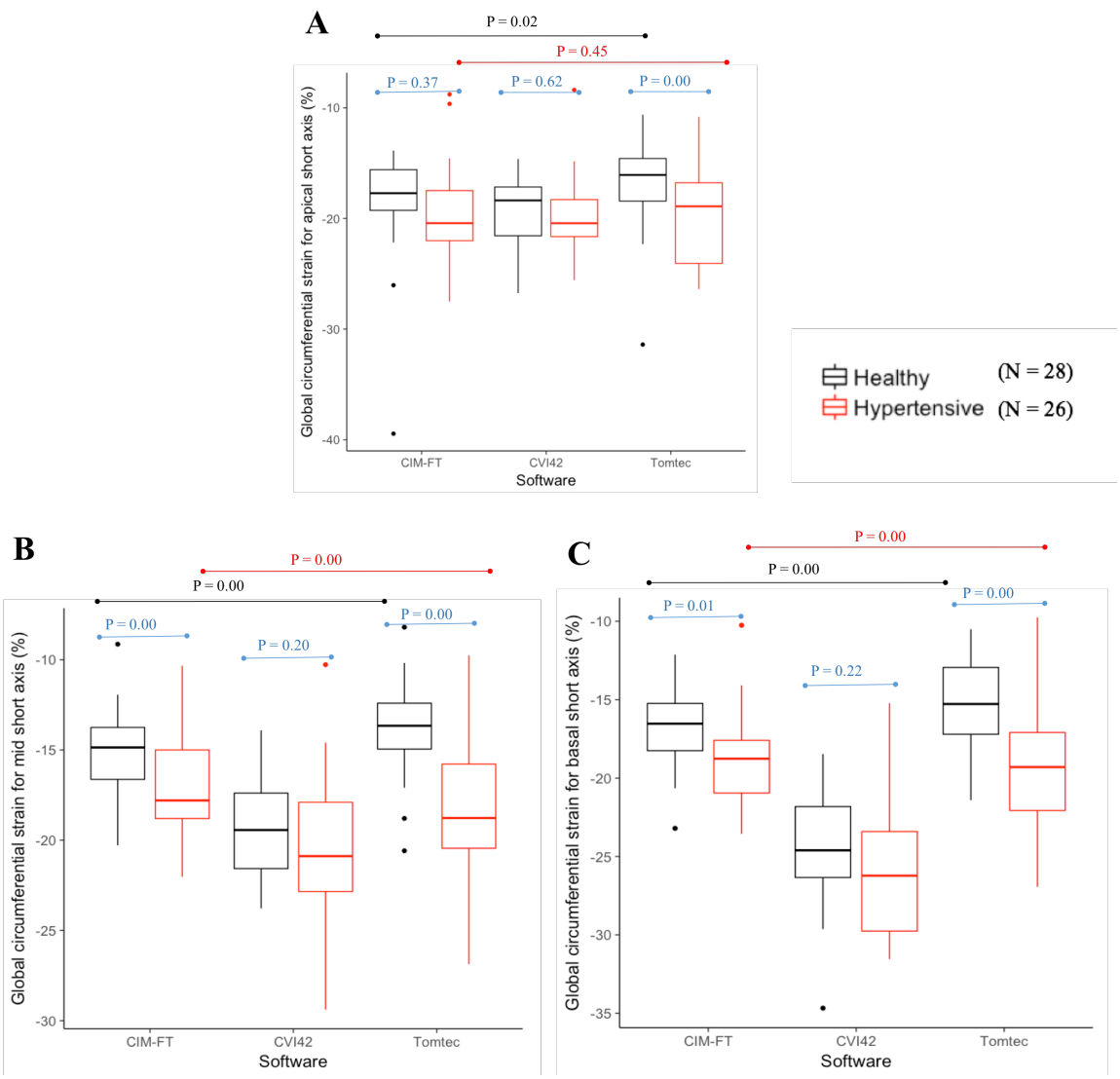

Figure 5.1: Box plots for global circumferential strains by Tomtec, CVI42 and CIM-FT in healthy subjects (black) and hypertensive patients (red) calculated from (A) apical, (B) mid and (C) basal short axis for the three software. The blue p-value (P<0.05 considered as significant) shows any significant difference between healthy subjects and hypertensive patients for Tomtec, CVI42 and CIM-FT software packages. The black p-value (P<0.05 considered as significant) shows any significant difference between Tomtec, CVI42 and CIM-FT software packages for healthy subjects. The red p-value (P<0.05 considered as significant) shows any significant difference between Tomtec, CVI42 and CIM-FT software packages for hypertensive patients. The significance level is unadjusted for multiple comparison.

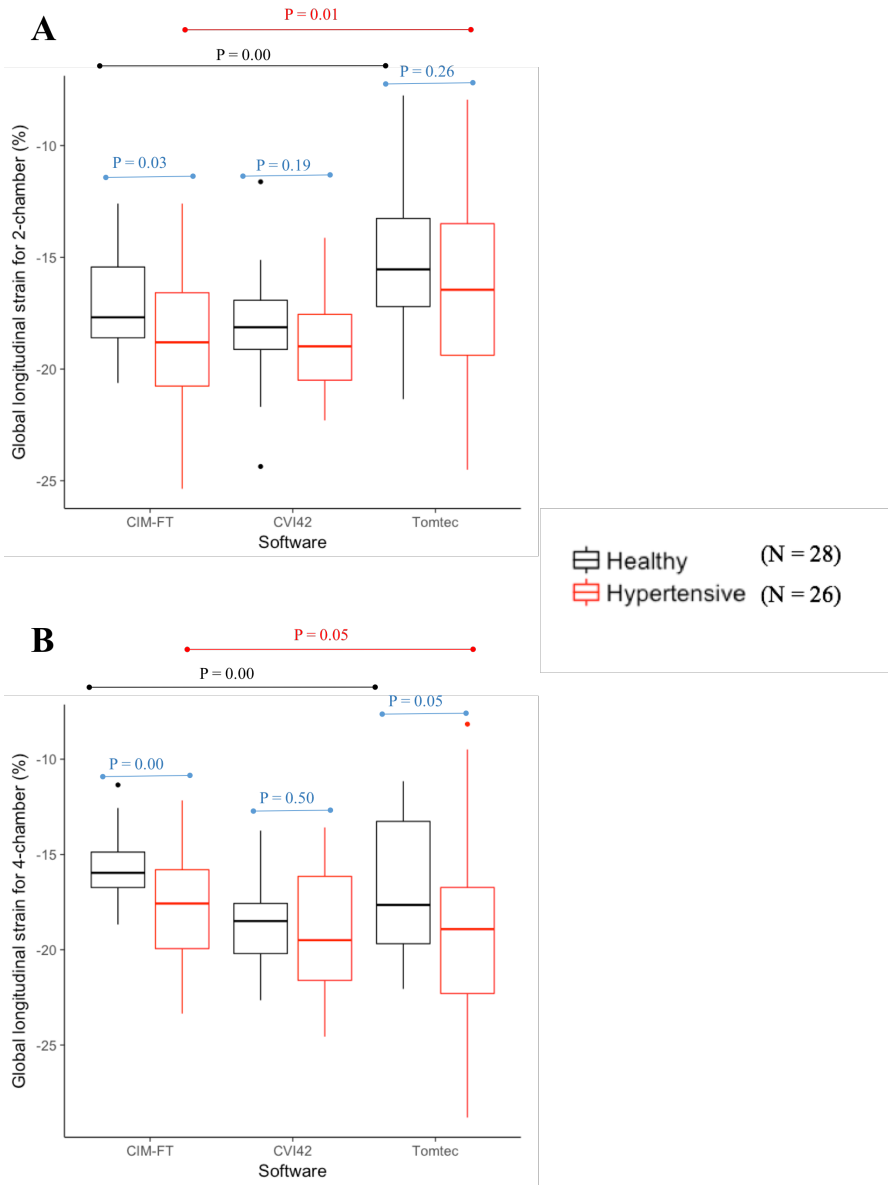

Figure 5.2: Box plots for global longitudinal strains by Tomtec, CVI42 and CIM-FT in healthy subjects (black) and hypertensive patients (red) calculated from (A) 2-chamber, (B) 4-chamber long axis for the three software. The blue p-value (P<0.05 considered as significant) shows any significant difference between healthy subjects and hypertensive patients for Tomtec, CVI42 and CIM-FT software packages. The black p-value (P<0.05 considered as significant) shows any significant difference between Tomtec, CVI42 and CIM-FT software packages for healthy subjects. The red p-value (P<0.05 considered as significant) shows any significant difference between Tomtec, CVI42 and CIM-FT software packages for hypertensive patients. The significance level is unadjusted for multiple comparison.

5.3.2 Inter and Intra-observer variability

Inter-observer variability was evaluated in all three FT software packages; results for the three software packages are shown in Table 5.5 and Bland-Altman for the global strains calculated with all three FT software packages are shown in Figure 5.3. Overall, inter-

observer variability was very good with all global strains in agreement for all software and a single parameter displaying significant statistical difference across the three software (Tomtec: endocardial circumferential strain calculated from the apical short axis slice). When considering all global measurement, CVI42 had the lowest bias (1.20 ± 2.95 %), followed by Tomtec (3.33 ± 7.33 %), with CIM-FT exhibiting the worse agreement (5.73 ± 15.03%). For the three software packages, global circumferential and longitudinal strain exhibited good agreement (better than 2%) whereas the agreement for radial strain was more variable. Across all parameters and software, the lowest bias and lowest standard deviation results were observed for circumferential and longitudinal strain parameters for Tomtec. For this software, the lowest bias for a global measurement was -0.04% (SD=±1.62) for 4-chamber longitudinal strain. For CVI42, the majority of global measurements (6/10) had a bias lower than 1%, with only one measurement being slightly worse than 3% (basal short axis radial strain). For CIM-FT, the agreement global circumferential and mid-short axis radial strains were good (<2%), however, the agreement for the other global radial measurements was poor especially for the basal short axis (over 20%) and the 2 long axis measurements (c.a. 13%).

Intra-observer variability results for the three software packages are given in Table 5.6 and Bland-Altman graphs for the global parameters for all three FT software packages are displayed in Figure 5.4. Overall, intra-observer variability was good but two parameters showed statistically significant differences; endocardial circumferential strain calculated from the apical short axis slice and the 2-chamber global longitudinal strain. When considering all global measurements, intra-observer displayed the same trend as inter-observer variability; CVI42 had the lowest bias (1.64 ± 3.67 %), followed by Tomtec (2.87 ± 7.81 %), with CIM-FT exhibiting the worse agreement (7.62 ± 12.84%). Across all parameters and software, the lowest bias and lowest standard deviation results were observed for longitudinal strain parameters for CVI42. For this software, the lowest bias

for a global measurement was 0.01 ± 1.89% for 4-chamber longitudinal strain closely followed by the 2-chamber longitudinal strain (0.16 ± 1.40%). CVI42 also performed really for global circumferential strains (all biases <2%) and for radial strain derived from apical and mid-short axis. Radial strain from long axis view was also acceptable (<3%) but poorer for the basal short axis.

Table 5.5: Bland-Altman statistics for inter-observer variability across all the measured strain parameters in healthy volunteers. Red cell = significant difference.

Strain (%)			Tomtec				CVI42				CIM-FT			
			Bias	SD	Limits of agreement		Bias	SD	Limits of agreement		Bias	SD	Limits of agreement	
Circumferential	Apical SAX	Global	-1.12	1.05	-3.17	0.94	0.28	0.89	-1.47	2.03	0.49	2.03	-3.49	4.49
		Endo	-2.31	1.58	-5.40	0.79	0.45	0.89	-1.28	2.19	0.72	2.93	-5.03	6.46
		Epi	0.11	1.44	-2.71	2.92	0.30	1.27	-2.18	2.78	0.24	1.70	-3.09	3.58
	Mid SAX	Global	-0.83	1.17	-3.13	1.47	0.26	0.49	-0.71	1.22	0.62	2.79	-4.87	6.09
		Endo	-1.06	1.57	-4.14	2.01	0.63	0.91	-1.15	2.42	1.41	3.18	-4.82	7.64
		Epi	-0.59	1.27	-3.08	1.89	0.25	0.69	-1.09	1.59	-0.26	2.74	-5.65	5.12
	Basal SAX	Global	-1.61	1.53	-4.62	1.39	0.84	0.92	-0.96	2.64	1.07	2.52	-3.87	6.02
		Endo	-2.67	2.53	-7.63	2.28	1.17	1.09	-0.97	3.31	2.74	3.09	-3.32	8.79
		Epi	-0.54	0.97	-2.44	1.37	0.61	1.04	-1.42	2.64	-0.58	2.40	-5.30	4.14
Radial	Apical SAX	Global	1.19	7.61	-13.73	16.12	-0.31	1.76	-3.75	3.14	6.49	22.23	-37.08	50.07
		Endo	-	-	-	-	-1.30	2.84	-6.84	4.23	39.31	76.03	-109.70	188.32
		Epi	-	-	-	-	-0.03	2.20	-4.33	4.27	-18.95	24.14	-66.25	28.35
	Mid SAX	Global	-5.45	6.34	-17.88	6.99	0.18	1.74	-3.21	3.58	0.68	33.28	-64.54	65.90
		Endo	-	-	-	-	-0.51	1.93	-4.27	3.25	36.59	62.01	-84.94	158.12
		Epi	-	-	-	-	0.48	1.55	-2.54	3.51	-16.39	28.62	-72.47	39.69
	Basal SAX	Global	-2.66	4.70	-11.88	6.56	-3.14	3.71	-10.37	4.08	-21.59	35.31	-90.80	47.61
		Endo	-	-	-	-	-4.82	5.33	-15.21	5.57	9.62	39.89	-68.58	87.81
		Epi	-	-	-	-	-1.79	3.18	-7.99	4.40	-45.40	49.51	-142.43	51.63
	2ch LAX	Global	-5.11	10.00	-24.72	14.49	-2.54	7.19	-16.58	11.49	13.17	28.34	-42.38	68.72
		Endo	-	-	-	-	-2.58	8.56	-19.28	14.12	12.98	30.34	-46.49	72.46
		Epi	-	-	-	-	-2.34	7.03	-16.05	11.37	12.75	26.09	-38.39	63.891
	4ch LAX	Global	-14.70	36.74	-86.71	57.31	1.92	7.34	-12.39	16.24	-12.61	22.38	-56.47	31.26
		Endo	-	-	-	-	0.99	5.89	-10.49	12.48	-14.81	22.81	-59.52	29.901
		Epi	-	-	-	-	2.81	8.64	-14.03	19.66	-10.54	21.98	-53.61	32.54
Longitudinal	2ch LAX	Global	0.58	2.59	-4.51	5.66	1.42	1.91	-2.29	5.14	-1.57	1.57	-4.64	1.49
		Endo	0.83	3.92	-6.86	8.512	1.53	2.15	-2.66	5.72	-1.64	2.72	-6.96	3.69
		Epi	0.29	1.69	-3.02	3.61	1.13	2.19	-3.15	5.40	-1.61	1.66	-4.87	1.65
	4ch LAX	Global	-0.04	1.62	-3.23	3.15	0.75	2.11	-3.36	4.86	-1.47	2.41	-6.19	3.245
		Endo	-0.001	1.64	-3.21	3.21	0.94	1.87	-2.70	4.59	-1.09	2.86	-6.69	4.512
		Epi	-0.11	1.91	-3.86	3.64	0.49	2.25	-3.89	4.87	-1.89	2.164	-6.13	2.35

Endo = endocardial, Epi= epicardial, SAX = short axis, LAX = long axis, 2ch = 2 chamber, 4ch = 4 chamber.

Table 5.6: Bland-Altman statistics for intra-observer variability across all the measured strain parameters in healthy volunteers. Red cell = significant difference.

Strain (%)			Tomtec				CVI42				CIM-FT			
			Bias	SD	Limits of agreement		Bias	SD	Limits of agreement		Bias	SD	Limits of agreement	
Circumferential	Apical SAX	Global	-1.14	1.03	-3.156	0.87	0.39	0.98	-1.52	2.32	-1.37	1.96	-5.20	2.46
		Endo	-0.55	1.98	-4.43	3.33	0.28	0.89	-1.47	2.03	-3.79	2.523	-8.75	1.16
		Epi	-1.65	1.66	-4.89	1.61	0.75	1.45	-2.08	3.58	0.88	2.167	-3.367	5.12
	Mid SAX	Global	0.18	0.87	-1.53	1.89	0.76	0.85	-0.90	2.42	-0.71	1.478	-3.601	2.19
		Endo	0.57	0.96	-1.31	2.46	0.96	1.14	-1.26	3.19	-1.94	2.46	-6.77	2.89
		Epi	-0.25	0.87	-1.97	1.46	0.89	1.10	-1.25	3.05	0.45	1.09	-1.678	2.578
	Basal SAX	Global	-0.90	0.88	-2.62	0.82	1.58	1.21	-0.77	3.93	-0.75	1.98	-4.63	3.13
		Endo	-1.04	1.79	-4.55	2.48	1.58	1.34	-1.04	4.19	-2.28	2.33	-6.85	2.28
		Epi	-0.77	0.65	-2.05	0.51	1.52	1.41	-1.22	4.27	0.66	2.52	-4.27	5.59
Radial	Apical SAX	Global	1.11	10.19	-18.87	21.09	-1.15	2.50	-6.03	3.73	21.02	24.31	-26.63	68.67
		Endo	-	-	-	-	-0.94	2.95	-6.70	4.82	43.68	77.69	-108.60	195.96
		Epi	-	-	-	-	-1.62	3.48	-8.40	5.16	9.88	20.75	-30.79	50.55
	Mid SAX	Global	-0.51	5.62	-11.51	10.50	-0.89	2.61	-5.99	4.19	13.24	27.36	-40.38	66.86
		Endo	-	-	-	-	-1.28	2.67	-6.50	3.92	52.76	48.29	-41.88	147.41
		Epi	-	-	-	-	-0.93	2.73	-6.25	4.39	-4.32	28.44	-60.056	51.41
	Basal SAX	Global	-1.35	7.90	-16.84	14.14	-6.32	5.84	-17.71	5.08	10.15	21.57	-32.12	52.42
		Endo	-	-	-	-	-7.41	7.96	-22.94	8.12	32.39	38.82	-43.70	108.47
		Epi	-	-	-	-	-5.09	5.19	-15.23	5.05	-0.19	23.09	-45.44	45.07
	2ch LAX	Global	-5.56	11.03	-27.18	16.06	-2.67	7.50	-17.29	11.96	20.448	25.81	-30.13	71.03
		Endo	-	-	-	-	-3.36	9.37	-21.63	14.92	21.69	27.25	-31.72	75.12
		Epi	-	-	-	-	-2.62	7.96	-18.15	12.90	19.11	24.21	-28.34	66.56
	4ch LAX	Global	-16.68	36.29	-87.81	54.44	2.49	11.90	-20.71	25.69	4.97	20.77	-35.73	45.68
		Endo	-	-	-	-	1.62	12.06	-21.90	25.14	5.27	21.50	-36.87	47.42
		Epi	-	-	-	-	1.99	14.63	-26.54	30.53	5.07	19.41	-32.96	43.11
Longitudinal	2ch LAX	Global	0.41	2.25	-4.00	4.81	0.16	1.40	-2.57	2.89	-1.79	1.46	-4.66	1.06
		Endo	0.31	2.71	-5.00	5.63	0.41	1.95	-3.39	4.22	-2.70	1.49	-5.63	0.23
		Epi	0.50	3.32	-5.99	7.00	0.12	1.56	-2.92	3.16	-0.79	1.73	-4.19	2.61
	4ch LAX	Global	0.82	2.02	-3.14	4.79	0.01	1.89	-3.68	3.70	-1.74	1.72	-5.11	1.63
		Endo	-0.62	1.68	-3.91	2.67	0.09	2.09	-3.99	4.19	-1.86	2.17	-6.03	2.31
		Epi	2.20	3.23	-4.14	8.55	0.43	2.52	-4.47	5.34	-1.51	1.75	-4.94	1.92

Endo = endocardial, Epi= epicardial, SAX = short axis, LAX = long axis, 2ch = 2 chamber, 4ch = 4 chamber.

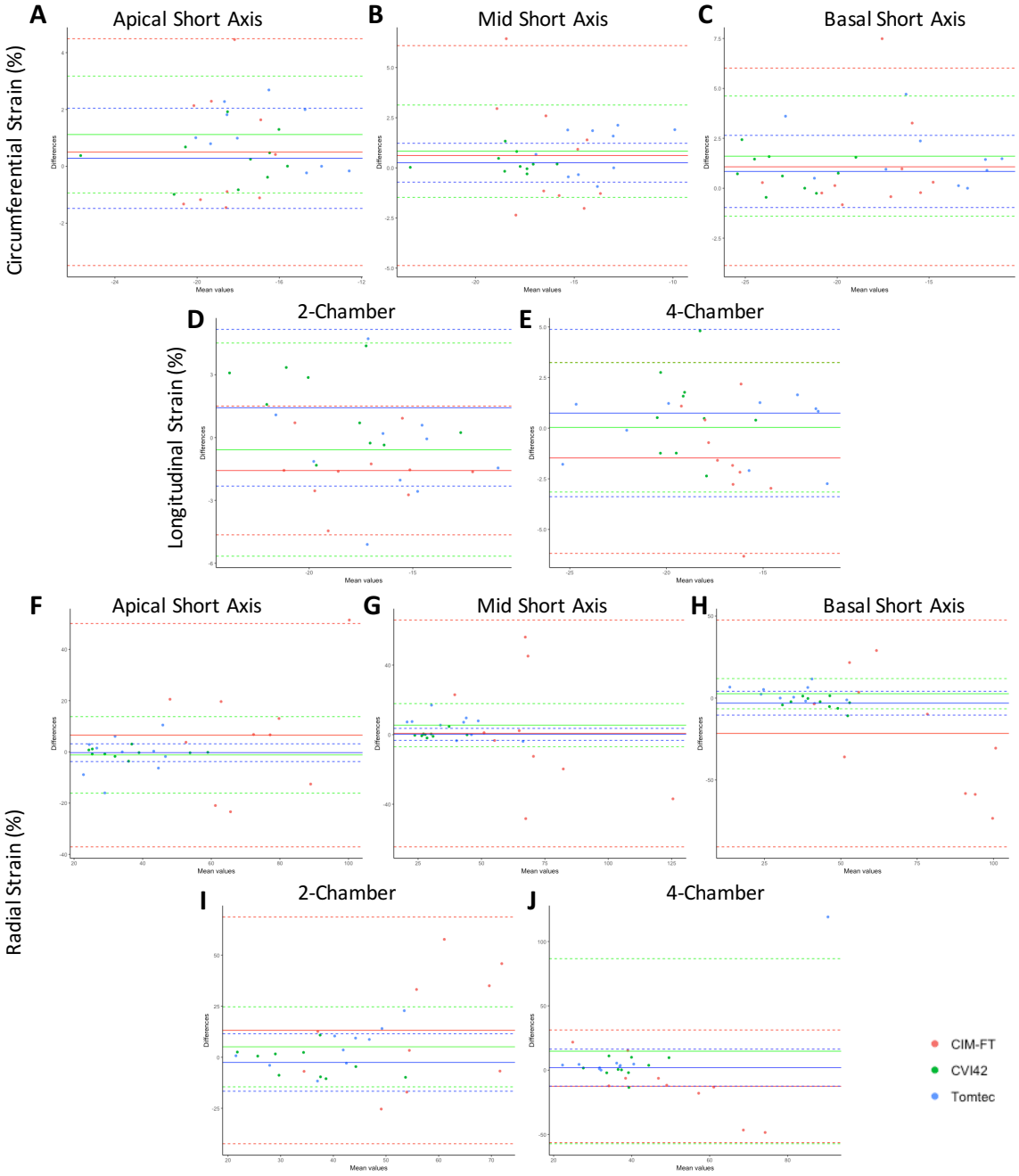

Figure 5.3: Bland-Altman plots for inter-observer variability for global strain parameters for all software. Top row (A-C) circumferential strain, second row (DE) longitudinal strain and bottom 2 rows (F-J) radial strain.

Tomtec did perform well for circumferential, longitudinal and short axis radial strains (all biases <2%) but the results were poor for radial strain for 2-chamber (-5.56 ± 11.03 %) and 4-chamber (-16.68 ± 36.29 %).

Once more CIM-FT was the poorest performer. Although the results were good for circumferential and longitudinal strains (<2%), they were poor from all radial strains with bias ranging from 5 to 21%.

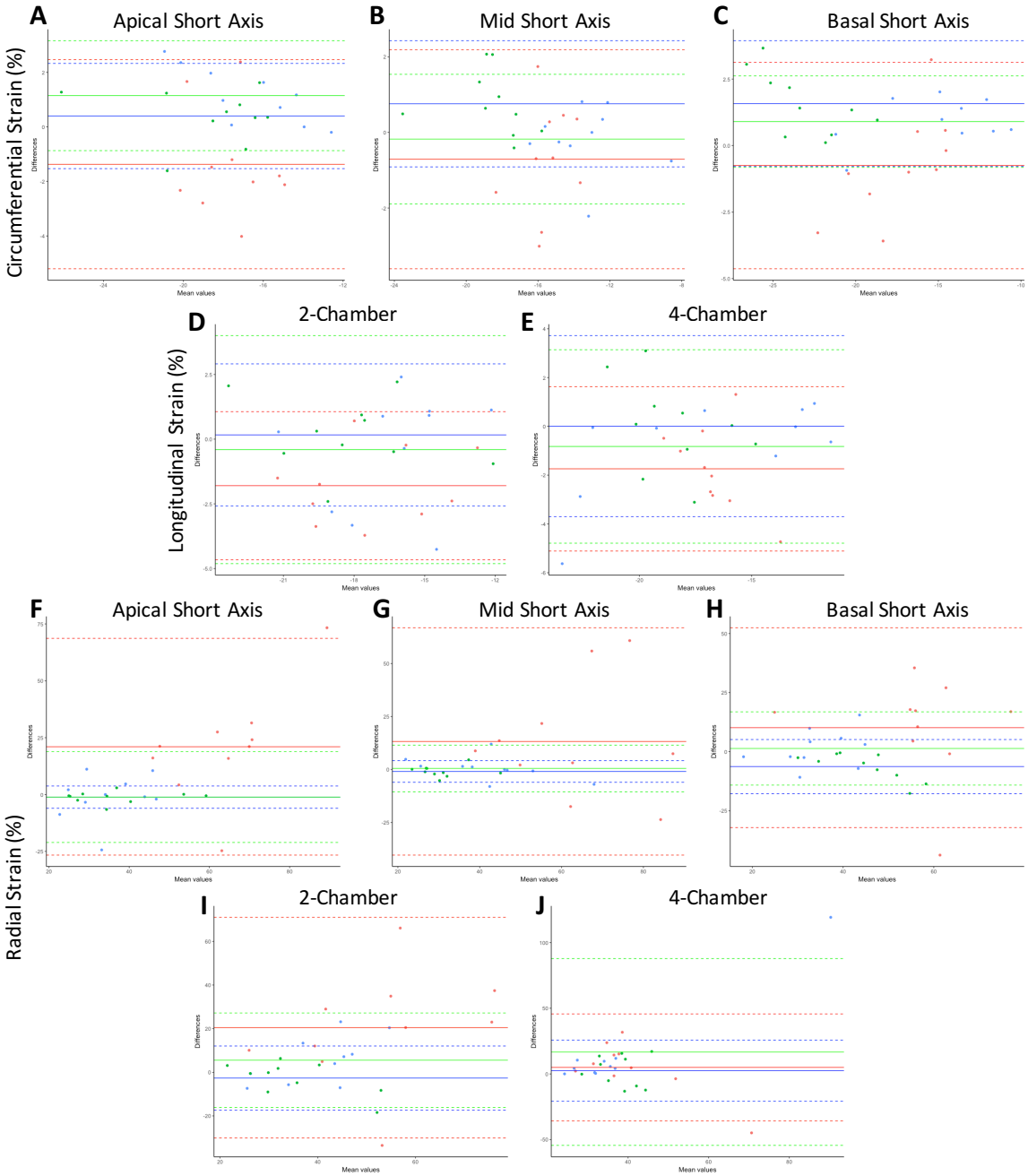

Figure 5.4: Bland-Altman plots for intra-observer variability for global strain parameters and all software. Top row (A-C) circumferential strain, second row (DE) longitudinal strain and bottom 2 rows (F-J) radial strain.

5.3.3 Comparison between populations

When comparing healthy subjects and hypertensive population, all three software packages returned slightly higher absolute global circumferential and global longitudinal strain values for the patient population (see Tables 5.2 and 5.3, Figures 5.1 and 5.2). However, the picture was mixed for global radial strain as the values measured for hypertensive patients were lower for Tomtec, slightly higher for CVI42 and significantly

higher for CIM-FT (Figure 5.5).

Table 5.7: Acquisition parameters for Steady State Free Precession (SSFP) sequence.

Parameters	Siemens MRI 1.5 scanner (26 hypertensive patients)	Philips MRI 1.5 scanner (28 healthy subjects)
TR (ms)	2.5	2.9
TE (ms)	1.24	1.44
Matrix	208 × 256	108 × 186
Field of view (mm^2)	292 ×360	205 × 380
Acquired pixel size (mm^2)	1.4 × 1.4	1.89 × 2.1
Temporal resolution (ms)	35	46
Slice thickness (mm)	7	8
Flip Angle (^{o})	70	60

In fact, there were significant differences in most parameter derived by CIM-FT between healthy subjects and hypertensive patients. Global, endocardial and epicardial radial strain for apical and mid ventricle short axis as well as for 2-chamber and 4-chamber were significantly lower in healthy subjects when compared to hypertensive patients. Furthermore, endocardial circumferential strain for basal and mid ventricle short axis as well as endocardial longitudinal strain for 4-chamber were statistically significantly lower in healthy subject results compared to hypertensive patients results derived by CIM-FT. However, epicardial circumferential strain for apical, mid ventricle and basal short axis by CIM-FT showed to be lower in hypertensive patients.

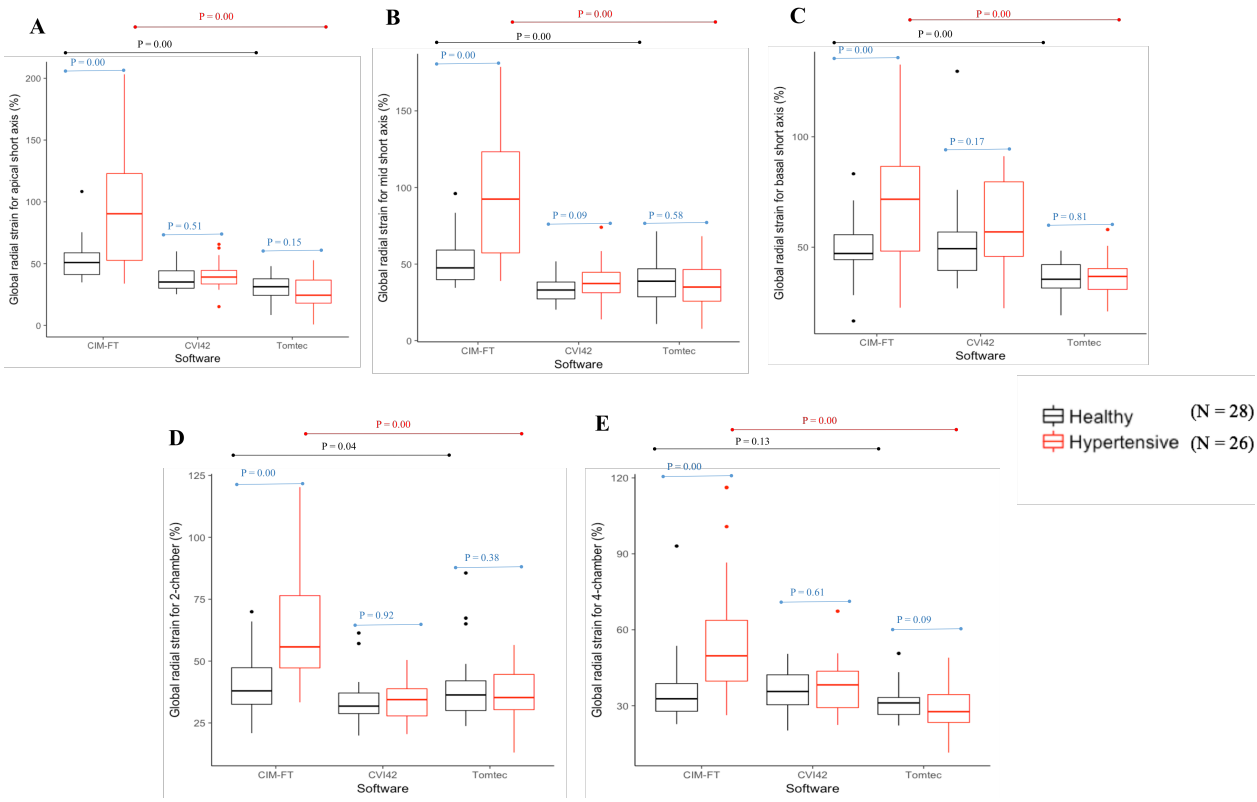

Figure 5.5: Global radial strains in healthy volunteers (black) and hypertensive patients (red) calculated from short axis (A-C), 2 chamber (D) and 4 chamber views (E) for the three software. Box plots for global radial strains by Tomtec, CVI42 and CIM-FT in healthy subjects (black) and hypertensive patients (red) calculated from (A) apical, (B) mid, (C) basal short axis for the three software. The blue p-value (P<0.05 considered as significant) shows any significant difference between healthy subjects and hypertensive patients for Tomtec, CVI42 and CIM-FT software packages. The black p-value (P<0.05 considered as significant) shows any significant difference between Tomtec, CVI42 and CIM-FT software packages for healthy subjects. The red p-value (P<0.05 considered as significant) shows any significant difference between Tomtec, CVI42 and CIM-FT software packages for hypertensive patients. The significance level is unadjusted for multiple comparison.

There were no significant differences between healthy subject's results and hypertensive patients' results derived by CVI42. While epicardial longitudinal strain for 4-chamber and epicardial circumferential strain for apical short axis as well as epicardial radial strain for apical short axis and for 2-chamber by CVI42 showed to be lower in hypertensive patients.

The endocardial circumferential strain for basal short axis by Tomtec was statistically lower in healthy subjects compared to hypertensive patients. Global, endocardial and epicardial circumferential strain for mid ventricle short axis was also statistically lower in

healthy subjects than hypertensive patients. However, global radial strain for apical and mid ventricle short axis, 2-chamber and 4-chamber by Tomtec showed to be lower in hypertensive patient than healthy subjects.

It is important to highlight that images for the healthy subjects and hypertensive patients CMR images were acquired at different centers using different scanners and with slightly different imaging parameters (Table 5.7) but at the same field strength. This was a pragmatic choice, as this hypertensive patient study did not include comparative healthy volunteer data but I had access to the healthy volunteer data from the HAPPY London Study (9). The main differences were a higher spatial and temporal resolutions for the hypertensive patients. This could potentially have an effect on the results of all three FT software packages and can be considered a potential confounding factor in this chapter. As explained in chapter 3 of this thesis, FT analysis relies on features (image signal intensities, local texture or patterns, boundaries edges) that can be tracked at pixel level in consecutive frames (3). The FT software packages define those features at the first frame in the area of interest identified by contours drawn on the endocardial and epicardial boundaries in the short axis or long axis view. After defining those features in the area of interest the FT software searches for the best comparable features in the following frames (3). Assuming comparable image quality, higher spatial and temporal resolutions would be expected to improve tracking accuracy (better ability to resolve finer in-plane and through time pixel motion) (39)(79). All healthy subjects and hypertensive patients' CMR images used for the analysis had no artefacts that could affect the FT tracking quality. Hence, it was possible to analyse all images without having to exclude any subjects in either groups.

5.4 Discussion

In this chapter, most absolute strain results were higher in hypertensive patients than healthy subjects for most global and regional parameters derived by the three FT software packages, which is not in line with previous studies (80)(81)(82). The only notable exception was for radial strains derived by Tomtec that were slightly lower in hypertensive patients. There were significant differences between healthy subjects and hypertensive patients strain results derived by Tomtec and CIM-FT, whereas differences calculated by CVI42 were not statistically significant. The significant differences between both groups were observed by the three software packages. It is important to highlight that both groups are not match in age and gender, and they use different CMR images acquisition parameters, particularly spatial and temporal resolutions. These limitations could be confounding factors and could affect the results.

In order to further investigate these findings, a similar analysis needs to be applied to a larger cohort matched in terms of age, gender and other demographic variables to eliminate any uncertainties."

Across the two groups and the three software, the most reliable and consistent parameters were circumferential strain for mid ventricle short axis followed by longitudinal strain results. The reproducibility was very high for those deformation strain parameters derived by CVI42 followed by Tomtec. CIM-FT exhibited the poorest results.

Although FT technique showed to be a promising tool to discriminate between healthy subjects and CVD patients (4)(50), the significant differences across the three FT software packages in both groups, can have a bad influence on the FT implementation in clinical practice today. The high variability makes it difficult to drive a reliable cut-off for healthy subjects and hypertensive patients in this chapter. The high variability observed in this chapter is consistent with several studies which previously observed variabilities in

FT technique (83)(7)(6)(73). As observed by previous studies, several other factors could have an impact on our results, which may have introduced variabilities in the measured parameters such as inherent natural physiological variability between subjects including gender, age, race (63). The CMR acquisition protocol parameters vary from vendor to vendor. The temporal and spatial resolution depends on the acquisition protocol and hence when they vary, this can affect image quality and impact on the analysed results. In this chapter, there were inherent variabilities between the two different populations, scanner types and CMR acquisition parameters, so possible discrepancies between groups can be expected. It is important to note that this is the first study conducted to compare three different FT software packages for circumferential, radial and longitudinal strain in hypertensive patients and healthy subjects. In terms of different scanners and different CMR image parameters, hypertensive patients showed agreement in more global and regional parameters compared to healthy results between the three FT software packages. This could be in part due to the higher spatial and temporal image resolutions resulting in a better tracking quality and therefore, better agreement between software approaches as shown in data using Friedman test in Table 5.2, Table 5.3 and ICC in Table 5.4 (39)(79). The most recent study compared four FT software packages (Tomtec, CVI42, Medis and MTT) in 110 subjects, including preclinical and overt arrhythmogenic right ventricle dysplasia patients and control group, to assess any agreement of right ventricle global and regional longitudinal strain measurements derived from four chamber acquisitions (83). In general, the results for the right ventricular longitudinal strain showed significant variability between the four FT software packages, which is consistent with the variability of the global longitudinal strain observed in this chapter across the three FT software and both groups. The ICC for absolute agreement for global longitudinal strain was 0.44 for the right ventricle (83), whereas in this chapter, the ICC was 0.45 for the left ventricle in healthy subjects, which was similar and two of those FT-software packages in their

research were also Tomtec and CVI42, which was similar to the ones used in our study (83). Also in their study, Tomtec had the highest longitudinal strain for 4-chamber compared to other FT software packages followed by CVI42 (83), while in our current study, Tomtec had the highest longitudinal strain in both groups followed by CVI42 as shown in Figure 5.2. Findings from this chapter are also in line with the observation of previous studies, which used multiple software packages for analysis of speckle tracking by echocardiography. In one study, it was reported that even previous versions of the same software yielded a wide range of global longitudinal strain with significant bias in healthy subjects (84) and hence, only the global longitudinal strain was compared since it was the most stable used parameter, and thus included as a quantification parameter in strain echocardiography examination guidelines (85). Similarly, another study investigating speckle tracking echocardiography applied seven different analysis approaches from different vendors to compare global longitudinal strain to healthy volunteers (69), the variation was small but significant.

Another related study, which used Tomtec and CVI42 for comparisons, noted reasonable inter- and intra-vendors' agreement for circumferential strain, high variability for radial strain of left ventricle. These findings are consistent with the results from this chapter, which showed that the most consistent parameter in both group was circumferential strain. Their study also ranked the degree of agreement according to software used for each parameter and reported more variability for circumferential strain measured by CVI42 and more variability for radial strain by Tomtec (73). In this chapter, CVI42 showed less variability for all parameters and best inter- and intra- agreement followed by Tomtec software.

Feature tracking technique offers the possibility to assess LV myocardial strain parameters from cine images, which is a more time-effective approach compared to the tagging technique, which requires separate acquisition of tagged images and more time-

consuming post-processing (61), which make FT attractive to use. There is increase demand on the FT technique after the first software (Tomtec) (8), and more recently, CVI42 and CIM-FT were introduced. However, it is important to note that all FT software packages used in this chapter required initial derivation of endocardial and epicardial delineation contours by the user and making correction to the tracking when necessary, which could also contribute to the observed variability. It is crucial that FT software variabilities are kept to a minimum with a high reproducibly to allow widespread clinical use (73).

Circumferential strain parameters for mid ventricle short axis images showed to be the most consistent parameter across the three software packages in both group in healthy subjects and hypertensive patients. Furthermore, the reproducible of circumferential strain is superior followed by longitudinal in comparison to radial strain parameters (67). The global circumferential strain showed the best agreement between Tomtec and CVI42 FT software packages in healthy subjects (73). Circumferential strain for mid ventricle is preferable in several studies (8) for its high reproducibility this could be a result of the mid-wall layer, with circumferentially oriented fibres (8)(86).

The reproducibility for inter- and intra-observer for the three FT software packages showed the best agreement with lowest bias and lowest standard deviation for circumferential and longitudinal strain parameters contrary to radial strain results. This finding is in line with previously published reviews in healthy subjects (87)(6)(73) which reported acceptable inter-observer agreement for global longitudinal strain and global circumferential strain of LV and RV using both CMR FT and echocardiography, poor inter-observer agreement for global radial strain in tetralogy of Fallot patients (67). These results are consistent with this chapter findings. Global deformation parameters were better for inter-observer than intra-observer across FT software packages as well as global measurements showed higher reproducibility compared to regional measurements, this is

in line with previous studies (6)(72).

5.5 Conclusion

This chapter compared the results of three FT software in hypertensive and healthy populations. The results might not be fully generalizable as the two populations were not matched and the images acquired on different scanners with different scan parameters. However, some interesting observations were made.

Firstly, most global and regional deformation parameters were significantly higher in hypertensive patients than in healthy subjects for all the three FT software packages but this may have been partly due to the confounding factors including different acquisitions parameters in particular temporal and spatial resolutions and both populations are not matched for age and gender.

Secondly, circumferential strain parameters for mid ventricle short axis images showed to be the most consistent parameter by ICC agreement in both groups.

Finally, when investigating the inter- and intra- observer variability, CVI42 showed a better reproducibility followed by Tomtec software. However, it is important to highlight that these results cannot be generalised to all other versions of these software packages as vendors constantly update and try to improve their tracking algorithms.

The circumferential and longitudinal strain parameters showed lowest bias and standard deviation as well as narrowest limits of agreement. Radial strain in general showed higher variations, wider limit of agreement, in particular when using the CIM-FT software package. Overall, the most consistent parameters across the three software by ICC agreement were circumferential strain for mid-ventricle short axis and to a lesser extend longitudinal strain.

Consequently, it might be advisable to use circumferential and longitudinal strains in

clinical analysis, especially when comparing results across centres/software. Conversely, radial strain showed high variation between the three software packages, and thus, it might be better to avoid using this parameter in isolation when comparing different studies.

In order to avoid some of the limitations, a larger cohort of hypertensive patients was studied in the next chapter. For chapter 6, both groups were recruited as part of the HAPPY London study. Consequently, the images were acquired with the same protocol on the same scanner. The main aim of the next chapter was to compare FT to the current MRI gold-standard for deformation, tagging. As CVI42, demonstrated the best reproducibility of the three software, only this one was used for the FT analysis.

Chapter 6: Comparison of feature tracking and tagging analysis in healthy subjects and hypertensive patients

6.1 Introduction

Although FT has seen improvements since its creation (87) and commercial software are now available, its abilities to highlight several cardiac health pathologies (83)(88) will only be truly harvested when the technique will be fully validated. Different studies, including chapter 5, have highlighted the high variability between different software. Another step, that needs to be taken to validate FT is to compare it to established techniques, echocardiography speckle tracking and CMR tagging that can be considered the "gold standard" for this modality.

This chapter aimed to compare the results from FT (CVI42) and tagging (CIMTag2D) in healthy subjects and hypertensive patients from the HAPPY London study (9). Since CVI42 software demonstrated the best reproducibility of the three software (Tomtec, CVI42 and CIM-FT) in chapter 5, hence only CVI42 was used for the FT analysis in this chapter. Compared to chapter 5, this chapter includes a larger cohort of hypertensive patients. Furthermore, both patients and controlled populations were recruited as part of the HAPPY London study. Consequently, the MRI scanner and the image acquisition parameters used are identical for both populations hence removing some of the limitations discussed in chapter 5. It is important to highlight that the healthy population used in this chapter is identical to the one used in chapter 5. The primary objective of this

chapter was to examine whether there was any agreement in global and regional cardiac deformation results between FT and tagging software packages in healthy participants and hypertensive patients. The secondary objectives were to examine whether hypertension could affect strain values when compared with a healthy population and to investigate if any deformation parameters displayed significant differences with regards to gender.

6.2 Methods

Twenty-eight (28) healthy subjects and sixty-two (62) hypertensive patients underwent the same standardised CMR scan (71). Left ventricular systolic strain deformation parameters results were derived by using FT and tagging software packages (CVI42 and CIMTag2D) to analyse cine SSFP and tagging images. The CMR cine acquisition protocol for SSFP and CSPAMM are presented in Chapter 4 (sections 4.1.1 and 4.1.2). The endocardial and epicardial borders of the mid ventricle short axis, as well as in the two and 4-chamber long axes of the left ventricle, were analysed as presented in the method chapter (sections 4.2.2 and 4.3).

6.2.1 Study Population

The population (Table 6.1) consisted of ninety (90) subjects including 62 hypertensive patients, 18 (29%) of whom had diabetes. All participants were aged 50 or over. Forty-nine (49%) of the hypertensive patients were on antihypertensive medications. All 28 healthy subjects that were recruited for the HAPPY London study had no previous angina or myocardial infarction, no history of stroke or transient ischaemic attack (TIA), or any cardiac sounding chest pain requiring further investigations. Other than vascular disease, healthy subjects had no medical history of diabetes, were not on hypertension treatment

and had no history of overt cardiac disease (9).

Table 6.1: Demographic variables for healthy subjects and hypertensive patients. Red cell = significant difference ($p<0.05$).

Parameters	**Healthy Subjects**	**Hypertensive Patients**
Number of participants	28	62
Female / Male	8 / 20	30 / 32
Age (years)	66.2 ± 5.3	65.1 ± 5.5
Height (m)	1.74 ± 0.10	1.69 ± 0.09
Weight (kg)	80.8 ± 11.4	81.5 ± 16.5
BMI (kg.m-2)	26.8 ± 3.1	28.2 ± 4.6
BSA (m2)	1.97 ± 0.18	1.95 ± 0.24
Systolic-BP (mmHg)	125.9 ± 8.6	138.7 ± 13.6
Diastolic-BP (mmHg)	77.1 ± 6.5	80.8 ± 10.3
Heart Rate (beats/minute)	59± 8	64 ± 12
LV Ejection Fraction (%)	62.1 ± 6.0	66.8 ± 6.8

BMI=body mass index, BSA=body surface area, BP=blood pressure, LV=left ventricle.

Population groups were not matched in term of size and gender, but were matched for age. The diastolic and systolic BP and the ejection fraction as well as heart rate show significant differences as those parameters are affected by hypertension. Both datasets were from the HAPPY London project previously described in section 4.1.3 p 63.(9). Healthy subjects that are included in this chapter are the same healthy subjects included in the previous chapter. Details by sex for the healthy subjects are given in Table 6.2.

Table 6.2: Demographic variables by sex for healthy subjects, red cells indicate statistical difference ($p<0.05$).

Parameters	Male	Female
Number	20	8
Age (years)	65.4±5.2	68.6±4.7
Systolic-BP (mmHg)	126.6±6.7	124.3±13.4
Diastolic-BP (mmHg)	78.1±6.9	74.4±4.3
Heart rate (beats/min)	58±8	63±7
BMI (kg/ m^2)	26.4±3.4	27.8±2.2
BSA (m^2)	2.02±0.2	1.80±0.1
LV EF (%)	60.8±5.5	65.9±6.3

BMI=body mass index, BSA=body surface area, BP=blood pressure, LV=left ventricle.

6.2.2 Statistical analysis

Statistical analysis was performed using IBM SPSS Statistics version 23. The demographic variables for healthy subjects and hypertensive patients were presented as the mean ± standard deviation (SD) in Tables 6.1 and 6.2. Continuous data for deformation parameters derived from CVI42 and CIMTag2D were presented as mean ± standard deviation (SD), in the healthy and hypertensive patients' results as shown in Table 6.3. The maximum and minimum values for each deformation parameter were identified in healthy subjects and hypertensive patients for CVI42 and CIMTag2D as shown in Table 6.4. Paired t-tests were carried out to determine any significant differences between CVI42 and CIMTag2D software packages; results as shown in Table 6.3. A significant difference for the paired t-test results in Table 6.3, after Bonferroni adjustment, was considered to be $p<0.003$ ($p<0.05$ divided by 18, the number of comparisons) (75). The inter- and intra-observer reproducibility of global and regional deformation parameters derived from CIMTag2D were evaluated by the Bland-Altman method, with a calculation of the 95% limits of agreement as shown in Table 6.5 (76). The p-value for inter- and intra-observer assessment were computed by paired t-test to

examine any significant bias between inter- and intra-measurements and the significance level after Bonferroni adjustment considered to be $p<0.003$ for inter-observer ($p<0.05$ divided by 18 comparisons) and $p<0.002$ for intra-observer ($p< 0.05$ divided by 30 comparisons). An independent sample t-test was used to compare strain values derived from CVI42 and CIMTag2D between healthy male and female subjects in Table 6.6 and between healthy subjects and hypertensive patient in Table 6.7. Box plots were used to compare between male and female strain results as well as between healthy subjects and hypertensive patients strain results. Bonferroni correction was not applied to the results in table 6.6 and 6.7 as the power was low for these comparisons and in order to avoid type II error for these associations. Principal components analysis (PCA) was performed to reduce the number of variables to aid interpretation (89). All subjects were included in the principal components analysis. A large number of derived variables (72) measured by CVI42 needed to be reduced. PCA reduced the number of the variables to a smaller number that retained 72% of the variance observed in the original data. CVI42 variables reduced to 9 variables loaded on four principal components as shown in Table 6.8. Spearman's correlation coefficient was applied to investigate the correlation between systolic and diastolic blood pressure and the components PC1, PC2, PC3 and PC4 that resulted from PCA results as shown in Table 6.9. The results for independent samples tests between demographic categorical variables (gender, hypertension, hypertension treatment, diabetes) with principal component analysis: PC1, PC2, PC3, and PC4 are shown in Table 6.10. The discrimination between hypertension and healthy subjects was evaluated using the area under the Receiver Operating Characteristic (ROC)) curve. For the area under the curve (ROC), a value of [0.90–1.0] was considered excellent, [0.80–0.90] good, [0.60–0.80] moderate and <0.60 poor (83)(90).

Table 6.3: A summary of CVI42 and CIMTag2D strain parameters. Data are presented as the mean ± standard deviation (SD) in healthy subjects and hypertensive patients. Red cell = significant difference (p<0.003).

Strain (%)		Healthy Subjects						Hypertensive Patients					
		Global		Endo		Epi		Global		Endo		Epi	
		FT	Tag	FT	Tag	FT	Tag	FT	Tag	FT	Tag	FT	Tag
Circumferential	**Mid SAX**	-19.40 ±2.63	-19.77 ±2.43	-20.82 ±2.72	-24.69 ±3.15	-18.03 ±2.67	-14.92 ±2.13	-20.23 ±2.94	-19.25 ±2.68	-21.78 ±3.15	-24.04 ±3.16	-18.64 ±2.69	-14.59 ±2.48
Radial	**Mid SAX**	33.88 ±7.87	28.13 ±14.28	38.21 ±8.82	26.66 ±24.25	30.03 ±7.34	34.56 ±13.49	37.79 ±10.01	30.56 ±8.45	43.13 ±12.13	27.94 ±9.70	32.76 ±8.09	36.05 ±11.19
	2ch LAX	33.58 ±8.84	25.28 ±13.76	33.93 ±10.05	28.11 ±16.56	33.82 ±8.32	23.07 ±11.66	36.39 ±9.30	25.89 ±11.27	36.47 ±9.96	26.93 ±13.39	36.42 ±9.11	25.79 ±10.71
	4ch LAX	35.95 ±7.63	27.74 ±15.23	37.09 ±8.74	33.32 ±18.92	37.41 ±8.80	23.15 ±12.93	36.08 ±9.59	26.19 ±11.58	36.58 ±9.66	30.19 ±17.46	36.67 ±10.75	23.53 ±9.36
Longitudinal	**2ch LAX**	-18.12 ±2.38	-15.48 ±3.00	-18.17 ±2.44	-16.35 ±3.35	-18.38 ±2.44	-14.55 ±3.02	-19.03 ±2.59	-14.09 ±2.17	-18.95 ±2.78	-15.17 ±2.60	-19.16 ±2.56	-12.81 ±2.15
	4ch LAX	-18.55 ±2.22	-15.96 ±2.24	-18.74 ±2.34	-16.08 ±2.64	-19.23 ±2.54	-15.70 ±2.18	-18.42 ±2.62	-14.92 ±2.03	-18.57 ±2.65	-15.19 ±2.53	-18.53 ±2.81	-14.08 ±2.06

Endo = Endocardial, Epi = Epicardial, SAX = short axis, LAX= long axis, ch = chamber, FT = CVI42, Tag = CIMTag2D.

Table 6.4: Maximum and minimum values for the different strain parameters (%) calculated using CVI42 and CIMTag2D in healthy subjects and hypertensive patients.

		Healthy Subjects						**Hypertensive patients**					
		CVI42			**CIMTag2D**			**CVI42**			**CIMTag2D**		
Strain (%)		**Global**	**Endo**	**Epi**	**Global**	**Endo**	**Epi**	**Global**	**Endo**	**Epi**	**Global**	**Endo**	**Epi**
Circumferential	**Mid SAX**	-23.78 -13.92	-25.39 -14.48	-23.62 -12.54	-23.90 -14.53	-30.22 -19.04	-18.67 -9.68	-29.47 -14.37	-31.17 -15.01	-26.56 -13.52	-25.76 -14.13	-31.88 -18.09	-21.33 -9.20
Radial	**Mid SAX**	20.27 51.79	21.46 57.73	17.99 51.16	10.04 74.42	2.92 106.08	14.85 75.54	20.86 73.31	21.58 83.59	19.26 57.22	15.15 58.44	6.99 50.62	16.59 80.08
	2ch LAX	19.93 61.35	20.47 67.84	18.66 59.36	10.42 59.91	13.58 69.39	9.34 50.07	21.89 68.23	20.19 70.43	22.64 71.77	14.47 80.14	16.98 81.33	12.67 79.32
	4ch LAX	20.17 50.48	21.26 57.91	19.87 55.75	9.81 72.01	10.28 80.56	10.82 64.53	17.75 68.26	18.74 71.89	18.09 70.89	12.09 75.14	11.67 93.95	9.99 58.38
Longitudinal	**2ch LAX**	-24.36 -11.62	-24.74 -11.57	-23.44 -11.24	-23.36 -5.98	-24.76 -7.89	-21.84 -3.94	-25.71 -13.57	-26.12 -13.12	-25.23 -13.61	-19.55 -7.96	-19.56 -7.05	-19.41 -7.44
	4ch LAX	-22.65 -13.75	-23.17 -13.51	-24.48 -13.91	-20.01 -11.64	-21.94 -10.89	-19.59 -11.05	-24.75 -10.78	-26.02 -11.26	-25.74 -10.77	-10.71 -10.03	-21.80 -8.42	-18.12 -8.97

Endo = endocardial, Epi = epicardial, SAX = short axis, LAX= long axis, ch = chamber.

6.3 Results

6.3.1 Healthy subjects

The radial, circumferential, and longitudinal strain means for global, endocardial, and epicardial regional measurements derived from mid ventricle short axis, 2-chamber and 4-chamber long axis views are given in Table 6.3.

Comparison between strain results derived from CVI42 and CIMTag2D in healthy subjects using paired t-test showed that there were significant differences between FT (CVI42) and tagging (CIMTag2D) software packages in 8 out of 18 parameters in healthy subjects, one global (longitudinal from 2-chamber long axis) and 7 regionals. For epicardial measurements only one was in agreement; radial strain from the mid-short axis slice.

Maximum and minimum values for global and regional circumferential, radial, longitudinal strain results between CVI42 and CIMTag2D in healthy subjects are shown in Table 6.4. The maximum and minimum value for global circumferential strain for mid ventricle short axis between CIMTag2D and CVI42 were comparable. However, the minimum values for global, endocardial and epicardial longitudinal strain for 2-chamber and 4-chamber were lower in CIMTag2D compared to CVI42. Likewise, the maximum values for global, endocardial and epicardial radial strain for mid ventricle short axis and 4-chamber were higher in CIMTag2D than CVI42.

Inter-observer variability for CIMTag2D results showed no significant difference between the two observers' measurements, except for global and endocardial circumferential strain calculated from the mid-ventricle short axis. The global circumferential strain for basal short axis showed the lowest bias between two measurements ($0.26 \pm 2.32\%$) and is displayed in Figure 6.1 (left-hand side). However,

wide limits of agreement were observed in most radial parameters (Table 6.5).

The Bland-Altman statistics for intra-observer variability from the CIMTag2D software measurements are shown in Table 6.5. There were no significant differences between two measurements in all global and regional strain parameters. Additionally, the lowest bias was shown for endocardial longitudinal strain for 2-chamber (0.05 ± 4.23%) as shown in Figure 6.1 (right-hand side), then for endocardial radial strain for apical short axis (-0.09%) with higher SD (±10.14). The widest limits of agreement were observed for epicardial radial strain for basal short axis.

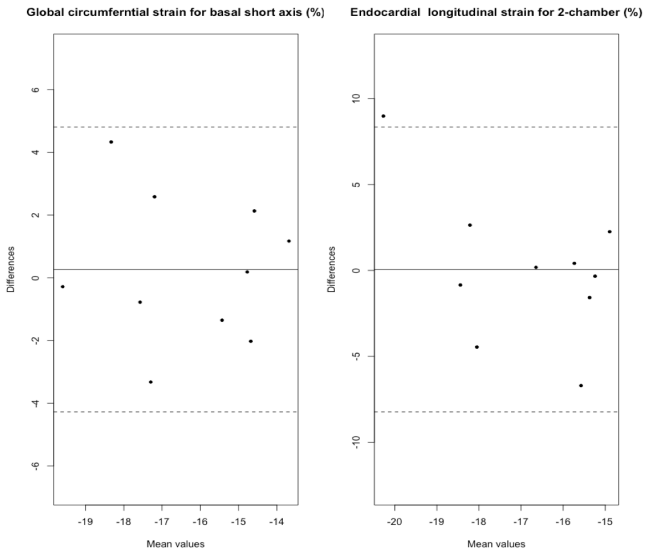

Figure 6.1: Bland-Altman graphs for the best inter-observer (left-hand side), and the best intra-observer (right-hand side) for CIMTag2D in healthy subjects.

The mean and standard deviation for all deformation parameters were calculated for healthy male and female subjects as measured by CVI42 and CIMTag2D (Table 6.6). There was significant difference for the body surface area (BSA) between male and female subjects but other parameters were in agreement. Given that the demographics were similar between both genders, this reduces the chance of confounding the comparison of strain parameters between male and female subjects.

Table 6.5: Bland-Altman statistics for CIMTag2D of ten healthy subjects for the intra-observer variability across all the measured parameters. Red cell = statistical significant difference

Strain (%)			Intra-observer variability					Inter-observer variability				
			Bias	SD	Limits of agreement		p-value	Bias	SD	Limits of agreement		p-value
Circumferential	Apical SAX	Global	0.78	2.50	-4.09	5.66	0.35	1.49	3.01	-4.39	7.36	0.15
		Endo	0.82	3.89	-6.77	8.41	0.52	2.33	5.05	-7.52	12.19	0.18
		Epi	0.45	1.66	-2.78	3.68	0.42	0.61	2.63	-4.51	5.73	0.48
	Mid SAX	Global	1.45	2.63	-3.69	6.59	0.12	1.85	1.34	-0.77	4.47	0.002
		Endo	1.31	3.43	-5.37	7.99	0.26	3.05	1.55	0.03	6.07	0.000
		Epi	1.48	2.33	-3.06	6.02	0.08	0.81	1.82	-2.74	4.37	0.19
	Basal SAX	Global	1.02	1.29	-1.51	3.54	0.04	0.26	2.32	-4.25	4.78	0.73
		Endo	0.73	1.98	-3.13	4.58	0.27	1.59	2.92	-4.11	7.28	0.12
		Epi	1.10	1.52	-1.87	4.07	0.05	-0.74	2.12	-4.87	3.39	0.29
Radial	Apical SAX	Global	-1.84	4.42	-10.47	6.79	0.22	0.59	9.99	-18.91	20.09	0.86
		Endo	-0.09	10.14	-19.86	19.69	0.98	6.08	12.81	-18.89	31.06	0.19
		Epi	-3.78	8.86	-21.06	13.51	0.21	-3.51	13.56	-29.95	22.92	0.43
	Mid SAX	Global	-2.0	9.17	-19.89	15.89	0.51	2.39	8.34	-13.87	18.66	0.39
		Endo	-2.99	15.58	-33.37	27.38	0.46	3.07	8.24	-13.01	19.14	0.27
		Epi	-3.51	8.91	-20.89	13.87	0.25	1.59	9.72	-17.36	20.54	0.62
	Basal SAX	Global	-8.42	14.43	-36.55	19.72	0.09	-1.51	12.97	-26.79	23.77	0.72
		Endo	-8.00	18.65	-44.38	28.37	0.21	1.66	16.04	-29.61	32.93	0.75
		Epi	-11.92	32.35	-75.00	51.17	0.27	-2.91	13.09	-28.44	22.62	0.50
	2ch LAX	Global	1.08	14.02	-26.25	28.42	0.81					
		Endo	1.63	17.26	-32.03	35.28	0.77					
		Epi	1.90	12.87	-23.19	26.99	0.65					
	4ch LAX	Global	9.10	13.39	-17.01	35.21	0.06					
		Endo	10.97	17.02	-22.22	44.16	0.07					
		Epi	6.83	10.04	-12.74	26.40	0.06					
Longitudinal	2ch LAX	Global	0.63	3.81	-6.81	8.06	0.62					
		Endo	0.05	4.23	-8.19	8.30	0.97					
		Epi	1.37	3.63	-5.72	8.45	0.26					
	4ch LAX	Global	1.09	2.00	-2.81	4.99	0.12					
		Endo	1.49	2.84	-4.05	7.03	0.13					
		Epi	0.99	1.85	-2.61	4.60	0.12					

Endo = endocardial, Epi = epicardial, SAX = short axis, LAX= long axis, ch = chamber, SD = standard deviation.

The absolute global circumferential, radial and longitudinal strain means parameters measured by CVI42 were consistently higher in females than in males. However, CIMTag2D results showed that all radial strain mean parameters were higher in males than females, whereas the absolute circumferential and longitudinal strain means parameters were higher in females than males as shown in Table 6.6.

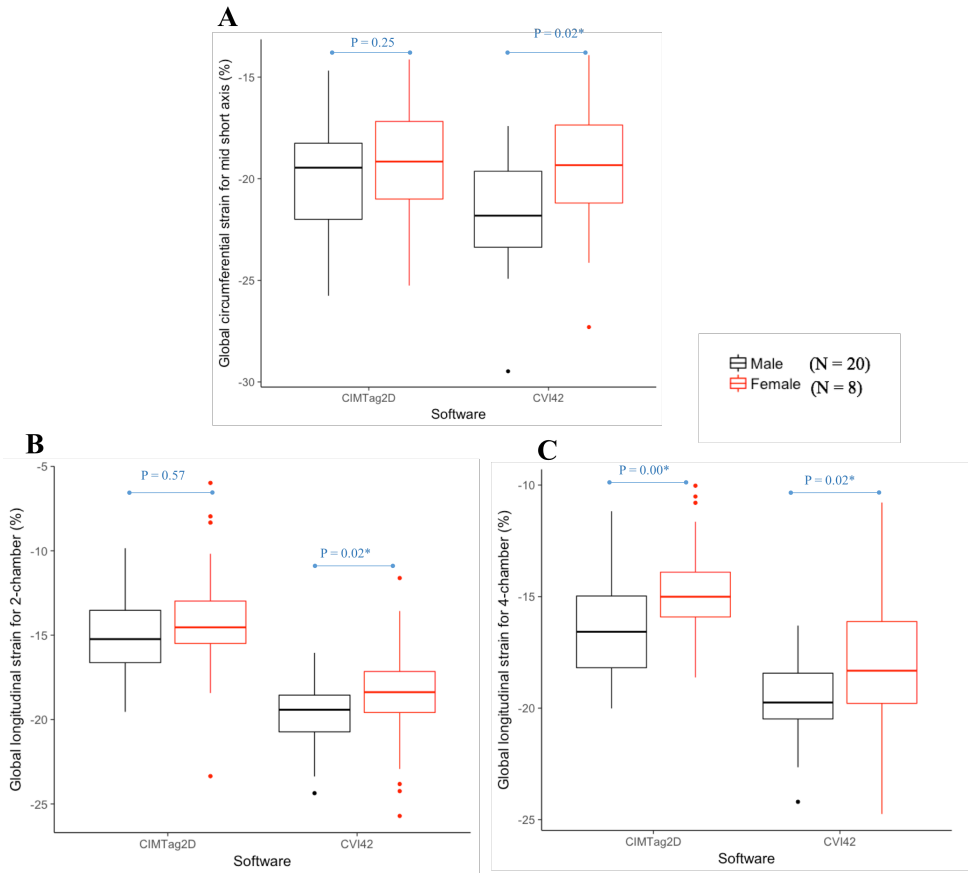

Figure 6.2: Box plots for male and female strain parameters derived by CVI42 and CIMTag2D. The blue p-value (P<0.05 considered as significant) shows any significant difference between healthy male and female subjects for CVI42 and CIMTag2D software packages. The significance level is unadjusted for multiple comparison.

There were significant differences between males and females for the measured global, endocardial, epicardial circumferential strain for mid ventricle short axis by CVI42 software. Epicardial radial strain for 2-chamber as well as global, endocardial and epicardial longitudinal strain for 2-chamber derived by CVI42 showed significant differences. Global, endocardial and epicardial longitudinal strain for 4-chamber generated from CVI42 showed significant difference between males and females. While,

in CIMTag2D results, epicardial radial strain for mid ventricle short axis and for 2-chamber showed significant differences. Global, endocardial and epicardial longitudinal strain for 4-chamber derived from CIMTag2D showed significant differences between males and females results.

Table 6.6: Summary of CVI42 and CIMTag2D strain parameters, for males (20) and females (8) in healthy subjects. Data is presented as mean ± standard deviation (SD). Red cell = significant difference ($p<0.05$).

Strain (%)			**CVI42**		**CIMTag2D**	
			Male	**Female**	**Male**	**Female**
Circumferential	**Mid SAX**	Global	-18.64 ±2.41	-21.29 ±2.29	-19.47 ±2.65	-20.49 ±1.74
		Endo	–20.05 ±2.47	–22.74 ±2.46	–24.49 ±3.49	–25.16 ±2.25
		Epi	–17.37 ±2.68	–19.66 ±1.90	–14.55 ±2.25	–15.82 ±1.62
Radial	**Mid SAX**	G	32.11 ±7.67	38.32 ±6.93	30.07 ±15.41	23.52 ±10.59
		Endo	36.24 ±8.49	43.15 ±8.09	26.82 ±25.17	26.27 ±23.56
		Epi	28.72 ±7.87	33.32 ±4.75	37.89 ±13.77	26.63 ±9.35
	2ch LAX	G	31.63 ±8.37	38.47 ±8.54	27.89 ±15.01	19.07 ±7.84
		Endo	31.93 ±9.67	38.93 ±9.80	30.77 ±18.11	21.81 ±10.53
		Epi	31.72 ±8.09	39.06 ±6.71	25.62 ±12.43	17.00 ±6.90
	4ch LAX	G	35.08 ±7.56	38.15 ±7.86	29.59 ±14.90	23.12 ±16.04
		Endo	36.11 ±8.16	39.54 ±10.22	35.36 ±18.82	28.22 ±19.41
		Epi	36.18 ±8.55	40.49 ±9.24	24.78 ±12.84	19.08 ±13.08
Longitudinal	**2ch LAX**	G	-17.38 ±1.99	-19.98 ±2.35	-14.42 ±4.84	-15.90 ±1.96
		Endo	–17.47 ±2.11	–19.94 ±2.42	–16.28 ±3.56	–16.53 ±3.03
		Epi	–17.59 ±2.17	–20.32 ±2.04	–14.28 ±3.54	–15.21 ±0.93
	4ch LAX	G	-17.99 ±2.23	-19.93 ±1.59	-15.26 ±2.07	-17.70 ±1.68
		Endo	–18.18 ±2.31	–20.14 ±1.89	–15.35 ±2.49	–17.92 ±2.15
		Epi	–18.65 ±2.51	–20.69 ±2.08	–15.03 ±2.02	–17.38 ±1.64

Endo = Endocardial, Epi = Epicardial, SAX = short axis, LAX= long axis, ch = chamber.

Global circumferential strain, global longitudinal strain from 2-chamber and global longitudinal strain from 4-chamber, female results were consistently higher in female for both CVI42 and CIMTag2D as can be seen in Figure 6.2. For CVI42, female results were significantly higher than male for all three parameters. For CIMTag2D, only the global longitudinal strain for 4-chamber result was significant."

6.3.2 Hypertensive patients

The global, endocardial and epicardial circumferential, radial, and longitudinal strain means and standard deviations for mid ventricle short axis, 2-chamber and 4-chamber long axis were measured by CVI42 and CIMTag2D software packages in hypertensive patients as shown in Table 6.3. There were significant differences between CVI42 and CIMTag2D in 13/18 parameters in hypertensive patients, including 4/6 global parameters. For epicardial regional parameters only one (radial strain from mid short axis) was in agreement. The other parameters in agreement were global circumferential strain from mid-ventricle short axis as well as epicardial radial strain from mid-ventricle short axis, endocardial radial strain and endocardial longitudinal strain from 4-chamber and global longitudinal strain from 2-chamber.

The maximum and minimum strain values for global, endocardial, epicardial circumferential strain for mid ventricle short axis were comparable between CVI42 and CIMTag2D as shown in Table 6.4. However, the maximum and minimum strain values for global, endocardial, epicardial longitudinal strain for 2-chamber and 4-chamber were consistently lower in CIMTag2D than CVI42. Likewise, the minimum strain values for global, endocardial, epicardial for radial strain parameters were consistently lower in CIMTag2D than CVI42.

Comparison between healthy subjects and hypertensive patients strain results derived by CVI42 and CIMTag2D are shown in Table 6.7. For CVI42, there was no statistical

differences between the two population groups; hypertensive patients exhibiting slightly higher absolute strain values for 13/18 parameters. For CIMTag2D, the hypertensive group had statistically lower absolute global and epicardial longitudinal strain from both 2 and 4-chamber views. The value was lower (but not statistically significant) for a further 8 parameters. Figure 6.3 shows the box plots comparing the two populations for the global parameters and comparing between CVI42 and CIMTag2D strain results in both groups.

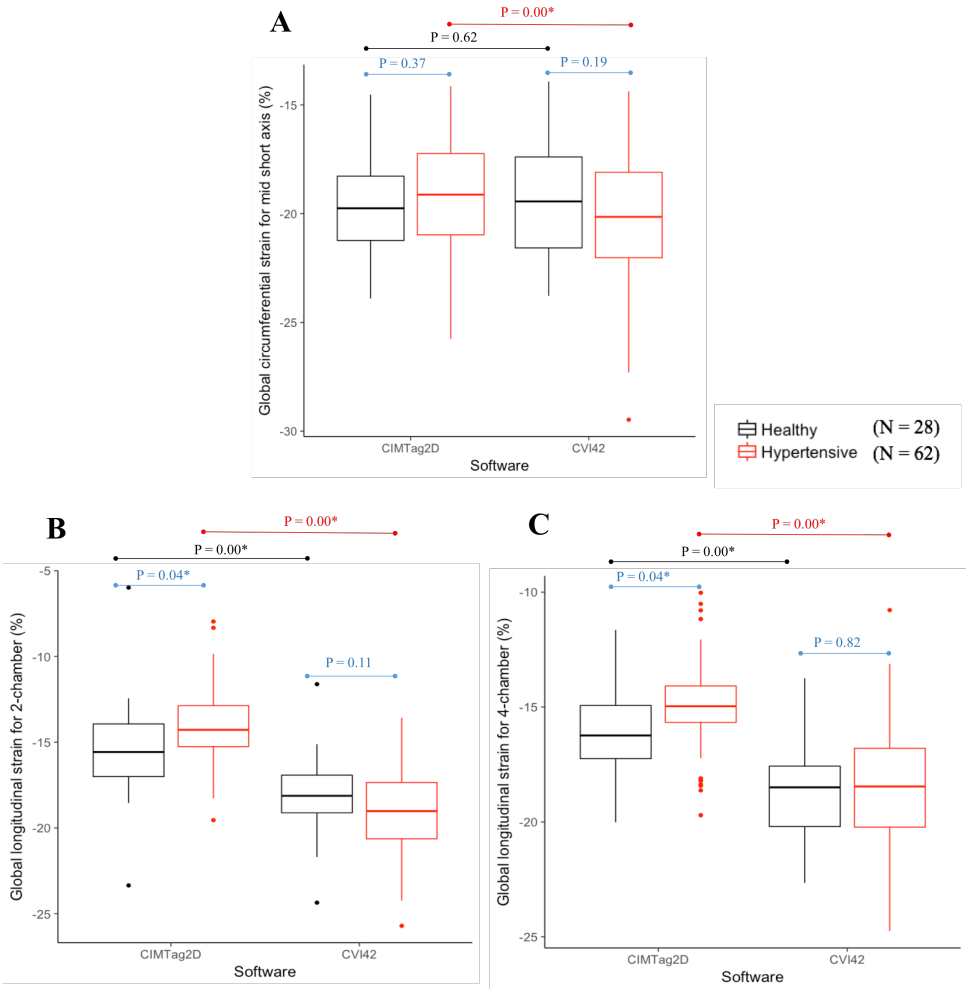

Figure 6.3: Box plots for healthy subjects and hypertensive patients global strain parameters derived by CVI42 and CIMTag2D. The blue p-value (P<0.05 considered as significant) shows any significant difference between healthy subjects and hypertensive patients for CVI42 and CIMTag2D software packages. The black p-value (P<0.05 considered as significant) shows any significant difference between CVI42 and CIMTag2D software packages for healthy subjects. The red p-value (P<0.05 considered as significant) shows any significant difference between CVI42 and CIMTag2D software packages for hypertensive patients. The significance level is unadjusted for multiple comparison.

Principal components analysis (PCA) was performed on the entire 90 subjects from the HAPPY London Study to reduce the number of variables, from the 72 original, generated by CVI42 software.

PCA was performed to reduce the number of variables to dimensions or components, so that the data can be more easily interpreted, and these components were treated as ordinary variables. PCA showed 9 variables loaded on four principal components called PC1, PC2, PC3, and PC4. The mid ventricle short axis radial strain and radial strain rate, the 2-chamber radial strain and radial strain rate, and the 4-chamber radial strain and radial strain rate and 4-chamber longitudinal strain rate explain 71.9 % of the total CVI42 software derived variables variance; the first component, PC1, explains 21.2 %, the second, PC2, explains 18.2 %, the third, PC3, explains 17.2 %, and the forth, PC4, explains 15.3 %.

Each component has a score which is the sum of its variables. Those variables plot against the component score to show the correlation coefficient for each variable for example the first component, the variable reverse peak for global radial strain rate for 4-chamber which showed highest correlation coefficient (-0.807) which has a negative correlation as shown in Table 6.8.

Table 6.7: Summary of CVI42 and CIMTag2D strain parameters. Data is presented as mean ± standard deviation (SD), red cells = significant difference ($p<0.05$).

Strain (%)			CVI42		CIMTag2D	
			Healthy	Hypertensive	Healthy	Hypertensive
Circumferential	**Mid SAX**	Global	-19.40 ±2.63	-20.22 ±2.94	-19.77 ±2.43	-19.25 ±2.67
		Endo	-20.82 ±2.72	-21.78 ±3.15	-24.69 ±3.15	-24.04 ±3.16
		Epi	-18.03 ±2.67	-18.6 4±2.69	-14.92 ±2.13	-14.59 ±2.48
Radial	**Mid SAX**	Global	33.88 ±7.87	37.79 ±10.01	28.13 ±14.28	30.56 ±8.45
		Endo	38.21 ±8.82	43.13 ±12.13	26.66 ±24.25	27.94 ±9.70
		Epi	30.03 ±7.34	32.76 ±8.09	34.56 ±13.49	36.05 ±11.19
	2ch LAX	Global	33.58 ±8.84	36.39 ±9.30	25.28 ±13.76	25.89 ±11.27
		Endo	33.93 ±10.05	36.47 ±9.96	28.11 ±16.56	26.93 ±13.39
		Epi	33.82 ±8.32	36.42 ±9.11	23.07 ±11.66	25.79 ±10.71
	4ch LAX	Global	35.96 ±7.63	36.08 ±9.59	27.74 ±15.23	26.19 ±11.58
		Endo	37.09 ±8.74	36.58 ±9.66	33.32 ±18.92	30.19 ±17.46
		Epi	37.41 ±8.80	36.67 ±10.75	23.15 ±12.93	23.53 ±9.36
Longitudinal	**2ch LAX**	Global	-18.12 ±2.38	-19.03 ±2.59	-15.48 ±3.00	-14.09 ±2.17
		Endo	-18.17 ±2.44	-18.95 ±2.78	-16.35 ±3.35	-15.17 ±2.60
		Epi	-18.38 ±2.44	-19.16 ±2.56	-14.55 ±3.01	-12.81 ±2.15
	4ch LAX	Global	-18.55 ±2.22	-18.42 ±2.62	-15.96 ±2.24	-14.92 ±2.03
		Endo	-18.74 ±2.34	-18.57 ±2.65	-16.08 ±2.64	-15.19 ±2.53
		Epi	-19.23 ±2.54	-18.53 ±2.81	-15.70 ±2.18	-14.08 ±2.06

Endo = Endocardial, Epi = Epicardial, SAX = short axis, LAX= long axis, ch = chamber.

There was no significant difference between systolic blood pressure and diastolic blood pressure with the components PC1, PC2, PC3 and PC4 as shown in Table 6.9. The relationships between the components PC1, PC2, PC3 and PC4 and categorical variables were examined by using independent samples t-tests, as shown in Table 6.10. PC2 score was significantly higher in hypertensive and those on hypertensive treatment than healthy or untreated subjects.

Table 6.8: Rotated component matrix including four components: each component has variables associated with each another.

Components variables	Component			
	PC1	PC2	PC3	PC4
SAM-Radial strain-peak-global		0.796		
SAM-Radial strain rate-reverse peak-global		-0.784		
2ch-Radial strain-peak-global			0.840	
2ch-Radial strain rate-peak-global			0.794	
4ch-Radial strain-peak-global	0.776			
4ch-Radial strain rate-peak-global	0.728			
4ch-Radial strain rate-reverse-peak-global	-0.807			
4ch-Longitudinal strain rate-peak-global				-0.901
4ch-Longitudinal strain rate-reverse peak-global		-0.441		0.652

SAM = mid short axis, 2ch = 2-chamber long axis and 4ch = 4-chamber long axis

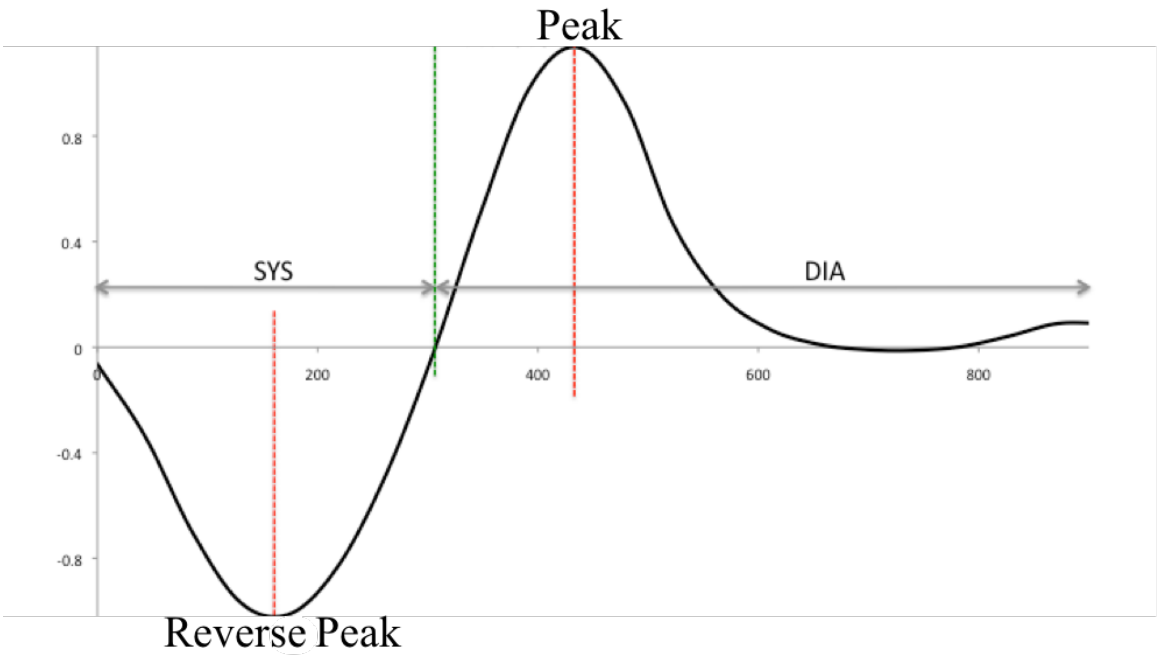

Figure 6.4: Example of a strain measurement (global, endocardial or epicardial) with one peak and reverse peak.

Figure 6.4 illustrates the negative strain curve for longitudinal strain parameters; the reverse peak represents the length of the left ventricle at the end-systolic phase compared to the length of left ventricle at the end-diastole phase. Negative strain (reverse peak) is caused by the shortening of the left ventricle. Strain (%) can be calculated as the

difference between the length at the end-systole and to the length at end-diastole. Epicardial longitudinal strain shows shortening in the end-systole (negative value) compared to the end-diastole.

Figure 6.5 showed the four variables that exhibited significant discrimination between hypertensive and healthy subjects in CIMTag2D, i.e. with a lower confidence interval being above 0.5 (an area of 0.5 would indicate no discrimination). The areas under the ROC curve ranged from 0.66 (95% (confidence Interval (CI)) CI: 0.53-0.80) to 0.75 (95% CI: 0.63-0.86) for these four variables indicating moderate discrimination. Figure 6.6 showed that no variables exhibited significant discrimination in CVI42 with the highest ROC areas ranged from 0.61 (95% CI: 0.49-0.74) to 0.62 (95% CI: 0.49-0.74) for both global and epicardial longitudinal strain for 2-chamber as well as for global and endocardial radial strain for mid ventricle short axis.

The lowest ROC area is 0.66 for CIMTag2D and the highest is 0.62 for CVI42 so all the CIMTag2D results are higher. The lower confidence intervals are all above 0.5 for CIMTag2D indicating significant discrimination. The lower confidence intervals are 0.49 for the CVI412 results, which are therefore not significant, as results with a confidence interval which includes 0.5 do not differ significantly from the diagonal line (black line, ROC area =0.5) where there is no discrimination between the two groups.

Table 6.9: Spearman's correlation between principle component analysis (PCA).

Parameters		**PC1**	**PC2**	**PC3**	**PC4**
Systolic-BP	**Correlation coefficient**	0.06	0.04	-0.01	-0.09
	p-value	0.56	0.72	0.93	0.39
Diastolic-BP	**Correlation coefficient**	0.01	-0.02	-0.17	-0.08
	p-value	0.96	0.84	0.12	0.49

Table 6.10: The results for independent samples tests between demographic categorical variables with principal component analysis: PC1, PC2, PC3, and PC4 for 90 healthy subjects and hypertensive patients. Red cell = statistical difference, SD = standard deviation.

Parameters	Gender		Hypertension		Hypertension treatment		Diabetes	
	Groups	Mean ±SD	Groups	Mean ±SD	Groups	Mean ±SD	Groups	Mean ±SD
PC1	Male	-0.08 ±0.84	Hypertensive	-0.004 ±1.06	Yes	0.13 ±1.08	Diabetic	0.004 ±1.13
	Female	0.22 ±1.33	Healthy	0.01 ±0.87	No	-0.16 ±0.88	Non-Diabetic	-0.001 ±0.98
PC2	Male	-0.11 ±0.91	Hypertensive	0.1 ±0.99	Yes	0.19 ±0.97	Diabetic	0.29 ±0.92
	Female	0.30 ±1.18	Healthy	-0.39 ±0.90	No	-0.23 ±1.00	Non-Diabetic	-0.72 ±1.01
PC3	Male	0.08 ±1.05	Hypertensive	0.09 ±1.06	Yes	0.17 ±1.12	Diabetic	0.17 ±0.99
	Female	-0.22 ±0.82	Healthy	-0.19 ±0.86	No	-0.19 ±0.79	Non-Diabetic	-0.04 ±1.01
PC4	Male	-0.07 ±0.95	Hypertensive	-0.12 ±0.98	Yes	-0.10 ±1.03	Diabetic	0.17 ±1.15
	Female	0.19 ±1.12	Healthy	0.26 ±1.01	No	0.12 ±0.96	Non-Diabetic	-0.04 ±0.97

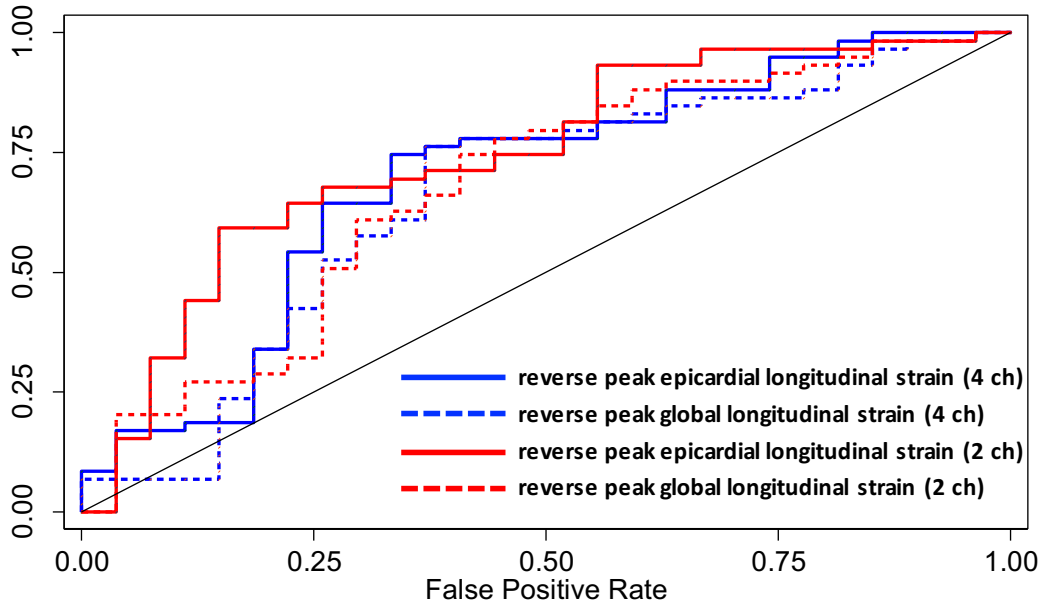

Figure 6.5: Area under curve for CIMTag2D deformation parameters to discriminate between hypertensive and healthy cardiac state.

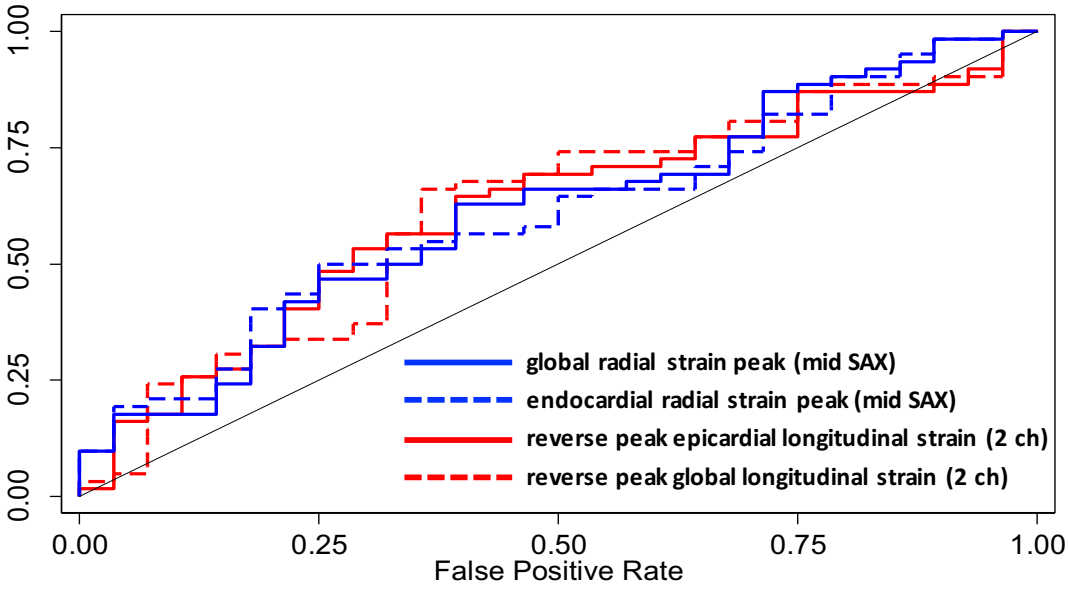

Figure 6.6: Area under curve for CVI42 deformation parameters to discriminate between hypertension and healthy cardiac state.

6.4 Discussion

This chapter compared FT to tagging, regarded as gold standard method (8), in both healthy subjects and large cohort of hypertensive patients. This chapter included the circumferential strain derived only from mid ventricle short axis level and longitudinal strain from 2-chamber and 4-chamber as those variables had a good agreement across all the three FT software packages in chapter 5. Chapter 5 showed that CVI42 had the highest reproducibility of the 3 FT software packages and consequently was the only one used for the FT analysis.

6.4.1 Reproducibility

Reproducibility for CIMTag2D showed better intra-observer compared to inter-observer agreement. The reproducibility for CVI42 for inter- and intra-observer showed to be better compared to CIMTag2D. In previous studies, FT and tagging technique results found that strain in radial direction showed wide limits of agreement with high variability

irrespective of the software technique used as shown in published articles (30)(45). Within this limit, circumferential and longitudinal strain showed the narrowest limit of agreement. So it is evident that circumferential strain results derived by FT and tagging showed low variability, and can thus be considered as a reliable parameter to consider in future research studies, as observed in previous studies (87)(30).

6.4.2 Comparison between techniques

There were significant differences between CVI42 and CIMTag2D in both groups, however, overall healthy subjects showed a better agreement. A number of factors might have influenced the observed differences including image quality, temporal and spatial resolution and other factors such as population size, age and gender (91)(92). It might be worth highlighting that slice positions of the SSFP and tagged images were similar but not identical.

A few parameters did not significantly vary between CIMTag2D and CVI42 in both groups in particular global circumferential strain and epicardial radial strain from the mid-ventricle short axis, and endocardial radial strain from the 4-chamber view. Circumferential strain for mid ventricle is considered to be the most reproducible parameters compared to apical and basal level in FT studies and tagging studies (8)(60)(62). Most published studies agreed that circumferential strain parameters are the most reliable irrespective of technique or software (8)(30)(67). A study comparing FT to CIMTag2D in 145 healthy subjects of which only 20 subjects with tagging images, noted a good agreement between techniques for circumferential strain while, FT overestimated radial and longitudinal strains, the subjects size was different between FT and tagging in this study (30). Another study in 35 healthy subjects, reported a good agreement for circumferential and longitudinal strain (45). In agreement with a previous study (8), global circumferential strain for mid ventricle short axis had a good correlation in healthy subjects. In this chapter, FT overestimated most parameters in both groups, which is in

line with previous study which noted that the radial strain results was overestimated by FT (30).

6.4.3 Normal Ranges

Normal range for strain parameters have been published in 2 meta-analysis. In the first one, based on echocardiography data, normal ranges were: global circumferential strain (GCS) [-20.9, -27.80]% (mean=-23.3%), global longitudinal strain (GLS) [-15.9, -22.1]% (mean=-19.7%), global radial strain (GRS) [35.10, 59] (mean=47.3%) (93). In the second, based on FT analysis, the minimum and maximum strain means for GCS were -17 to -25%, GLS -19 to -24%, GRS 15 to 51% (72). However, in this chapter the range values for GCS (-13.92 to -23.78%), GLS (-11.62 to -24.36%) and GRS (19.93 to 61.35%) by FT. However, the range values generated in this chapter for GCS (-14.53 to -23.90%) CLS (-5.98 to -23.36%) and GRS (9.81 to 74.42%) by tagging technique. Our healthy strain ranges showed that the maximum values for GRS were higher than the published ranges by echocardiography and FT, and published normal range vary also from echocardiography and published normal for FT derived from different articles (93)(72). The minimum value for GCS and GLS is much lower than the previous articles, whereas the maximum values of GCS and GLS were within the published range (93)(72). Considering those variations in normal values, researchers should be encouraged to include control subjects in their studies.

6.4.4 Gender comparison

Regarding gender, both software could differentiate between healthy male and female; epicardial radial strain for 2-chamber and global, endocardial and epicardial longitudinal strain for 4-chamber were significantly higher for female than male. This result could have been affected by the smaller female sample size. A previous study showed that radial velocity and radial displacement measured by CMR-FT were higher in males than

females, the study involved a larger population size (males=54, females=62) (30). Another study found that males showed a higher radial strain than female whereas the circumferential and longitudinal strains were lower in males (males=75, females=75) (91).

6.4.5 Differences between groups

In this chapter, FT did not show any significant difference between healthy subjects and hypertensive patients, but longitudinal strain measured using tagging could discriminate between groups. This is consistent with previous studies that reported reduction in longitudinal and circumferential strain (80), and reduction in longitudinal, circumferential and radial strain (81). Dysfunction of longitudinal contractility in hypertensive patients has also been previously reported (82). Several studies found that decreased longitudinal strain is a sensitive predictor for early detection of sub-clinical LV dysfunction than left ventricle ejection fraction (94)(95)(96). Longitudinal strain is considered to be a strong and independent predicator for heart failure admission and increased mortality (96). Longitudinal fibers are mainly subendocardial and subepicardial, hence the GLS was considered to be a useful strain parameter in echocardiography strain quantification (85).

With regards to systolic and diastolic blood pressures, results in this chapter showed a weak reverse correlation with radial strain and strain rate from mid-ventricle and 2-chamber and longitudinal strain rate for 4-chamber. A previous study in 272 patients also reported an inverse correlation of systolic blood pressure with global longitudinal strain demonstrated the reduction in strain with increased afterload (97). The inverse correlation noted in our study may be because hypertensive conditions induce a compensatory thickening of the ventricular wall in an attempt to normalize wall stress which result in decreases of the contractility of longitudinal fibers (21).

6.5 Conclusion

This chapter compared FT (CVI42) and tagging (CIMTag2D) analyses to calculate myocardial deformation parameters from CMR images in a large cohort of healthy subjects and hypertensive patients. In this chapter only the CVI42 FT software was used since it showed the best reproducibility among the three software (Tomtec, CVI42 and CIM-FT) in chapter 5. Most of the limitations of chapter 5 were removed (cohort size, imaging protocol, age match), however, the two populations were not matched in term of size and gender.

A number of important conclusions can be drawn from this chapter. Firstly, tagging analysis with CIMTag2D software (version 8.1.5) showed good inter- and intra- observer reproducibility with the best intra reader agreement for two-chamber endocardial longitudinal strain and the best inter-reader agreement for global circumferential strain for the basal short axis. However, FT, CVI42 software (release 5.1.1) showed the lowest bias and standard deviation for circumferential, radial and longitudinal strain parameters in comparison to CIMTag2D for intra-agreement. CVI42 had the best inter-agreement for circumferential and radial strain parameters for short axes in comparison to CIMTag2D.

Secondly, there were significant differences for most measured parameters obtained between healthy subjects and hypertensive patients for both FT (CVI42) and tagging (CIMTag2D). The only parameters not to exhibit statistically significant differences in both groups were global circumferential strain for mid ventricle short axis, epicardial radial strain for mid ventricle short axis and endocardial radial strain for 4-chamber.

Thirdly, both FT (CVI42) and tagging (CIMTag2D) could differentiate between healthy male and female subjects; 2-chamber epicardial radial strain and 4-chamber global, endocardial and epicardial longitudinal strain were significantly higher in females for both techniques apart from epicardial radial strain for 2-chamber by CIMTag2D which

was significantly higher in male than female.

Finally, there were significant differences in longitudinal strain calculated from tagged images; it was lower in hypertensive patients. No significant differences could be found for individual parameters calculated with FT (CVI42), however when FT parameters were analysed using PCA. A component combining mid ventricle short axis radial strain parameters and 4-chamber longitudinal strain rate parameters showed a significant difference between hypertensive and non-hypertensive patients. Giving the low agreement between both software packages noted in this study, determining a reproducible reference cut off for a single or group of parameters remains challenging at this stage. At present, in the absence of standardisation, it might be recommendable for each group to obtain healthy reference values for their set-up (specific combination of imaging protocol and analysis method).

Alternatively, a numerical phantom, as explored in the next chapter, could be used to compare values between software packages to facilitate comparison between sites/studies.

Chapter 7: Development of Numerical Phantoms for FT Validation

7.1 Introduction

Feature tracking was evaluated by comparing three software packages in chapter 5. Furthermore, in chapter 6, the most reproducible software was compared to MR-tagging, an established method to assess cardiac deformation (87), and applied to a larger cohort. The results showed great variability, and significant differences, in most strain parameters derived from the three FT software packages, as well as between FT and tagging. However, in chapter 5, there were a good agreement for mid-ventricle short axis circumferential strain and to a lesser extend for longitudinal strain. In chapter 6, the best agreement between FT and tagging was for mid-ventricle global circumferential strain followed by 2-chamber global longitudinal strain.

As discussed in chapter (review), other research studies have demonstrated the potential usefulness of FT tracking parameters to differentiate between healthy subjects and CVD patients (50)(98)(51). However, there are no publications reporting the clinical implementation and reliability of measured deformation parameters obtained from the FT. The variability observed in the previous chapters clearly highlights the difficulties of using those parameters in the clinic. The only reliable way to establish why observed parameters vary between software would be to use a gold standard numerical model (3)(99). This need is further compelled by the fact that FT commercial software packages algorithms are not readily available to understand the sources of potential differences.

The aim of this chapter was to design simplified numerical simulation where all motion

and deformation parameters are known and can be calculated analytically; this will serve as a gold standard for FT techniques validation. The gold standard validation is to use a numerical model to verify accuracy of the deformation measurements derived by FT software against the known motion of that numerical simulation calculated from mathematical equations.

The theoretical motion and strain values of the numerical phantom were compared to the experimental results measured using the FT software packages. In order to achieve this goal, several numerical simulations of left ventricle short axis and long axis simulation models of gradual complexity were implemented.

7.2 Method

All numerical simulation images were carried out with the Matlab programming language (MathWorks, Natick, MA, USA). Series of synthetic DICOM images mimicking a simplified left-ventricular (LV) motion model were generated and saved for subsequent FT analysis. A radial movement in the short axis view, and radial and longitudinal movements in the long axis model view were modelled. The numerical simulations consisted of short axis and long axis cine frames generated using different myocardial intensity patterns, i.e. uniform, radial, and circular checkerboard.

The short axis endocardial and epicardial borders were generated by plotting two concentric circles, resulting in an annulus representing the myocardium. The endocardial border is represented by a circle C_{endo} (equation 1) where its radius $r_{radial}^{endo}(t)$ varies through the cardiac cycle following a cosine function (equation 2). The epicardial border is represented by a circle C_{epi} (equation 3) where its radius $r_{radial}^{epi}(t)$ varies through the cardiac cycle following a cosine function (equation 4). Radii (mm) are expressed as a function of time t (ms), where t takes the values 1, 2…T, with T the heartbeat period. T

was set to 1000 ms (heartrate of 60 bpm) in the simulations.

$$C_{endo}: \sqrt{(x - x_0)^2 + (y - y_0)^2} = r_{radial}^{endo}(t) \quad (1)$$

$$r_{radial}^{endo}(t) = -\left(\left(\frac{(r_{max}^{endo} + r_{min}^{endo})}{2}\right) + \left(\frac{(r_{max}^{endo} - r_{min}^{endo})}{2}\right) \times \cos\left(\frac{2\pi t}{T}\right)\right) \quad (2)$$

$$C_{epi}: \sqrt{(x - x_0)^2 + (y - y_0)^2} = r_{radial}^{epi}(t) \quad (3)$$

$$r_{radial}^{epi}(t) = -\left(\left(\frac{(r_{max}^{epi} + r_{min}^{epi})}{2}\right) + \left(\frac{(r_{max}^{epi} - r_{min}^{epi})}{2}\right) \times \cos\left(\frac{2\pi t}{T}\right)\right) \quad (4)$$

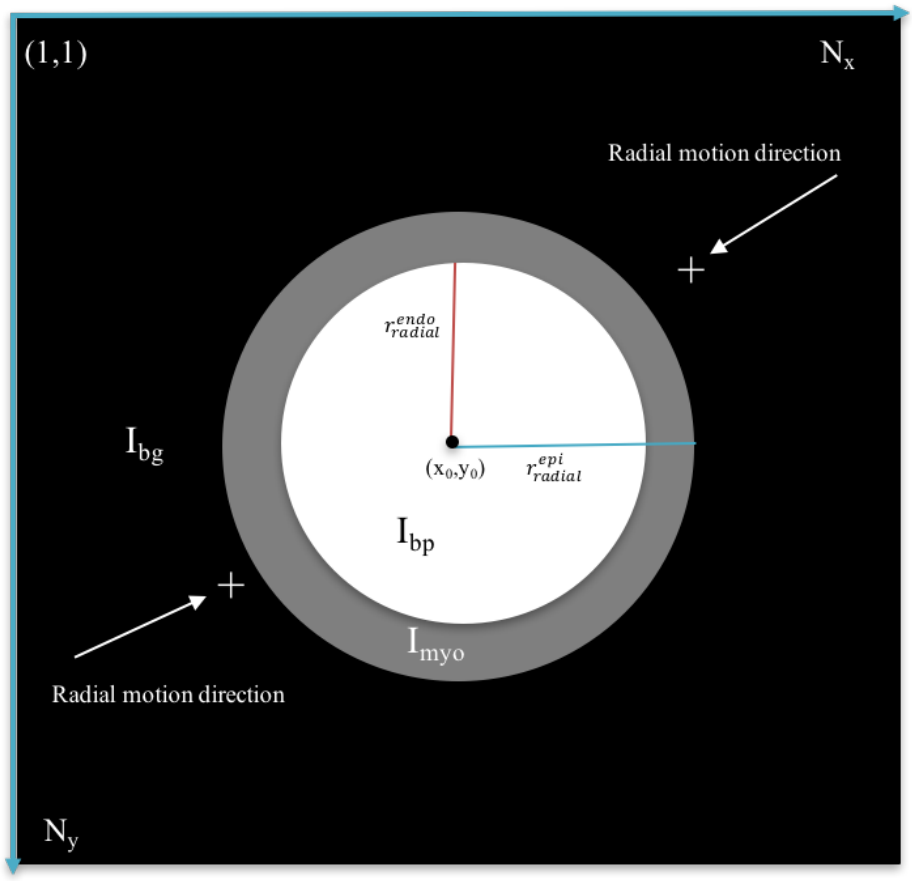

Figure 7.1: The short axis simulation model with endocardial border with r_{radial}^{endo} radius and epicardial border with r_{radial}^{epi} radius inside a matrix of ($N_x \times N_y$). I_{bg}, I_{myo} and I_{bp} represent the image signal intensities of background, myocardium and blood pool regions respectively.

Circles are concentric with centre image coordinates of x_0 and y_0. The x and y coordinate can vary from 1 to $N_{x,y}$ with N_x and N_y equals to the image matrix size (Figure 7.1). The maximum and minimum values represent the endocardial and epicardial radial and longitudinal radii expansion and contraction at end-diastole and end-systole respectively. The endocardial and epicardial radial and longitudinal motions are controlled by a set of

parameters given in Table 7.1 while the other image parameters are given in Table 7.2.

Equations 2 and 4 give $r_{radial}^{endo}(t)$ and $r_{radial}^{epi}(t)$ as a function of time, expressed as a cosine function. There is a continuous variation in the radii of both circles and by using the parameters in Table 7.1, the displacement for $r_{radial}^{endo}(t)$ and $r_{radial}^{epi}(t)$ can be expressed as:

$$d_{radial}^{endo}(t) = -\left[\left(\left(\frac{(r_{max}^{endo} + r_{min}^{endo})}{2}\right) + \left(\frac{(r_{max}^{endo} - r_{min}^{endo})}{2}\right) \times \cos\left(\frac{2\pi t}{T}\right)\right) - \left(\left(\frac{(r_{max}^{endo} + r_{min}^{endo})}{2}\right) + \left(\frac{(r_{max}^{endo} - r_{min}^{endo})}{2}\right) \times \cos\left(\frac{2\pi 0}{T}\right)\right)\right] \quad (5)$$

$$d_{radial}^{epi}(t) = -\left[\left(\left(\frac{(r_{max}^{epi} + r_{min}^{epi})}{2}\right) + \left(\frac{(r_{max}^{epi} - r_{min}^{epi})}{2}\right) \times \cos\left(\frac{2\pi t}{T}\right)\right) - \left(\left(\frac{(r_{max}^{epi} + r_{min}^{epi})}{2}\right) + \left(\frac{(r_{max}^{epi} - r_{min}^{epi})}{2}\right) \times \cos\left(\frac{2\pi 0}{T}\right)\right)\right] \quad (6)$$

The analytical radial displacement values from equations 5 and 6 are negative and the positive direction of motion was selected as shown in Figure 7.1 and 7.2, in order to match the direction of motion used by the FT software packages (100).

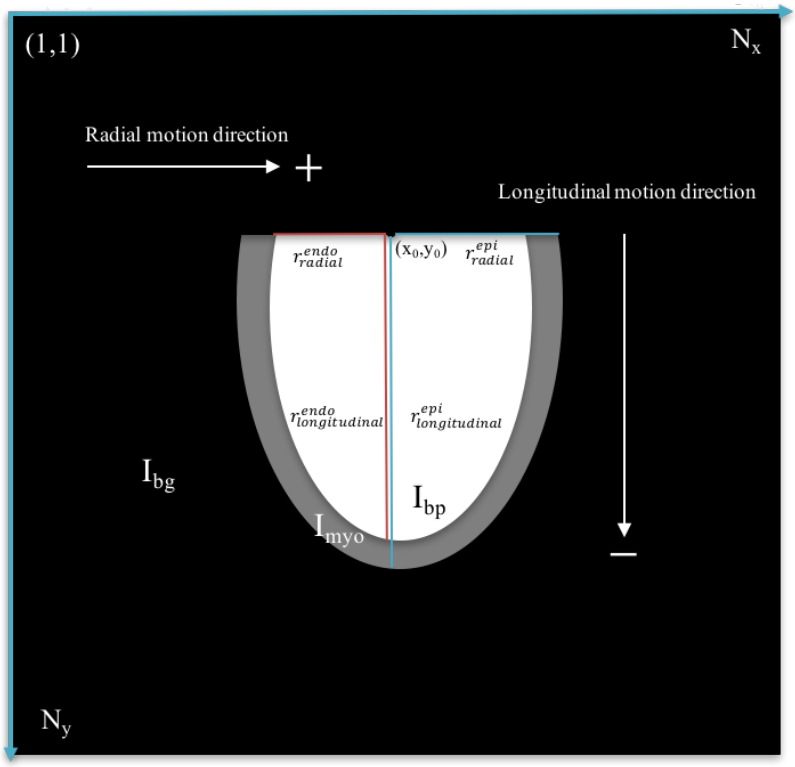

Figure 7.2: Long axis simulation model endocardial border with r_{radial}^{endo} and $r_{longitudinal}^{endo}$ radii and epicardial border with r_{radial}^{epi} and $r_{longitudinal}^{epi}$ radii inside a matrix of (N_x × N_y). I_{bg}, I_{myo} and I_{bp} represent the image signal intensities of background, myocardium and blood pool regions respectively.

Table 7.1: Parameters used to define the simulation short and long axis; the maximum and minimum values for endocardial and epicardial, radial and longitudinal radii represents the radii at end-diastole and end-systole. The parameters values measured from images of a healthy patient.

Parameters		**Short axis model**	**Long axis model**
Time (ms)	Max	950	950
	Min	0	0
r_{radial}^{endo}(t) (mm)	Max	25	55
	Min	15	48
r_{radial}^{epi}(t) (mm)	Max	30	68
	Min	27	60
$r_{longitudinal}^{endo}(t)$ (mm)	Max	NA	100
	Min	NA	84
$r_{longitudinal}^{epi}(t)$ (mm)	Max	NA	105
	Min	NA	90

The endocardial and epicardial borders of long axis model were generated by plotting two concentric semi-ellipses; LAX1 and LAX2 (Figure 7.2). The variations of those two semi-ellipses through the cardiac cycles are given by the following set of equations:

$$\text{LAX1}: \frac{(\text{x}-\text{x0})^2}{r_{radial}^{endo}(t)^2} + \frac{(\text{y}-\text{y0})^2}{r_{longitudinal}^{endo}(t)^2} = \tag{7}$$

$$r_{radial}^{endo}(\text{t}) = -\left(\left(\frac{(r_{max}^{endo} + r_{min}^{endo})}{2}\right) + \left(\frac{(r_{max}^{endo} - r_{min}^{endo})}{2}\right) \times \cos\left(\frac{2\pi t}{T}\right)\right) \tag{8}$$

$$r_{longitudinal}^{endo}(t) = \left(\left(\frac{(r_{max}^{endo} + r_{min}^{endo})}{2}\right) + \left(\frac{(r_{max}^{endo} - r_{min}^{endo})}{2}\right) \times \cos\left(\frac{2\pi t}{T}\right)\right) \tag{9}$$

$$\text{LAX2}: \frac{(\text{x} - \text{x0})^2}{r_{radial}^{epi}(t)^2} + \frac{(\text{y} - \text{y0})^2}{r_{longitudinal}^{epi}(t)^2} = 1 \tag{10}$$

$$r_{radial}^{epi}(\text{t}) = -\left(\left(\frac{(r_{max}^{epi} + r_{min}^{epi})}{2}\right) + \left(\frac{(r_{max}^{epi} - r_{min}^{epi})}{2}\right) \times \cos\left(\frac{2\pi t}{T}\right)\right) \tag{11}$$

$$r_{longitudinal}^{epi}(t) = \left(\left(\frac{(r_{max}^{epi} + r_{min}^{epi})}{2}\right) + \left(\frac{(r_{max}^{epi} - r_{min}^{epi})}{2}\right) \times \cos\left(\frac{2\pi t}{T}\right)\right) \tag{12}$$

The endocardial and epicardial radial and longitudinal motions for the long axis model are controlled by a set of parameters given in Table 7.1.

Table 7.2: Image parameters for the short and long axis simulations.

Parameters	Short axis and long axis images
N_x	360
N_y	360
Spatial resolution (mm)	1
Temporal resolution (ms)	50
Number of cardiac phases	20

The endocardial and epicardial radial and longitudinal displacements follow the form of equations 5 and 6.

In the short axis model, the derived endocardial and epicardial radial motion parameters are the displacement and velocity, while the radial deformation parameters, strain and strain rate, are derived from the endocardial and epicardial radial radii $r_{radial}^{endo}(\mathrm{t})$ and $r_{radial}^{epi}(\mathrm{t})$ in equations 2 and 4 shown as analytical values in Table 7.3. The results include endocardial and epicardial displacement measured in mm, velocity measured in mm/s, strain in % and strain rate in %/s. The endocardial and epicardial radial velocities $v_{radial}^{endo}(t)$ and $v_{radial}^{epi}(t)$ in equations 13 and 14, are the derivatives of $r_{radial}^{endo}(\mathrm{t})$ and $r_{radial}^{epi}(\mathrm{t})$, respectively, with respect to time measured in (mm/s) (3).

$$v_{radial}^{endo}(t) = \frac{dr_{radial}^{endo}(\mathrm{t})}{dt} = 10\pi \ \sin(\frac{2\pi t}{T}) \tag{13}$$

$$v_{radial}^{epi}(t) \ = \frac{dr_{radial}^{epi}(\mathrm{t})}{dt} = 3\pi \ \sin(\frac{2\pi t}{T}) \tag{14}$$

The endocardial and epicardial radial strain are calculated from equations 15 and 16 and expressed in %.

$$\mathrm{S}_{radial}^{endo}(\mathrm{t}) = 100\times \frac{\left(r_{radial}^{endo}(\mathrm{t}) - r_{radial}^{endo}(0)\right)}{r_{radial}^{endo}(0)} \tag{15}$$

$$\mathrm{S}_{radial}^{epi}(\mathrm{t}) = 100\times \frac{\left((r_{radial}^{epi}(\mathrm{t}) - r_{radial}^{epi}(0)\right)}{r_{radial}^{epi}(0)} \tag{16}$$

The endocardial and epicardial radial strain rate equations, $Sr_{radial}^{endo}(t)$ and $Sr_{radial}^{epi}(t)$, respectively, are measured in %/s as follow (3):

$$Sr_{radial}^{endo}(t) = 100\times \frac{v_{radial}^{endo}(t)}{r_{radial}^{endo}(\mathrm{t})} \quad (17)$$

$$Sr_{radial}^{epi}(t) = 100\times \frac{v_{radial}^{epi}(t)}{r_{radial}^{epi}(\mathrm{t})} \quad (18)$$

In the long axis model, the endocardial and epicardial radial and longitudinal motion and deformation parameters are derived from $r_{radial}^{endo}(\mathrm{t})$, $r_{longitudinal}^{endo}(t)$, $r_{radial}^{epi}(\mathrm{t})$, $r_{longitudinal}^{epi}(t)$. The endocardial and epicardial radial velocities $v_{radial}^{endo}(t)$ and $v_{radial}^{epi}(t)$ (equations 19 and 20) are the derivatives of $r_{radial}^{endo}(\mathrm{t})$ and $r_{radial}^{epi}(\mathrm{t})$ with respect to time and measured in mm/s (3), the endocardial and epicardial radial strain are shown in equations 21 and 22.

$$v_{radial}^{endo}(\mathrm{t}) = \frac{dr_{radial}^{endo}(\mathrm{t})}{dt} = 7\pi \sin\left(\frac{2\pi t}{T}\right) \quad (19)$$

$$v_{radial}^{epi}(\mathrm{t}) = \frac{dr_{radial}^{epi}(\mathrm{t})}{dt} = 8\pi \sin\left(\frac{2\pi t}{T}\right) \quad (20)$$

$$Sr_{radial}^{endo}(\mathrm{t}) = 100\times \frac{v_{radial}^{endo}(\mathrm{t})}{r_{radial}^{endo}(\mathrm{t})} \quad (21)$$

$$Sr_{radial}^{epi}(\mathrm{t}) = 100\times \frac{v_{radial}^{epi}(\mathrm{t})}{r_{radial}^{epi}(\mathrm{t})} \quad (22)$$

The endocardial longitudinal velocity is calculated from equation 23, while the epicardial longitudinal velocity is calculated from equation 24 and measured in mm/s:

$$v_{longitudinal}^{endo}(t) = \frac{dr_{longitudinal}^{endo}(t)}{dt} = -16\,\pi \sin(\frac{2\pi t}{T}) \quad (23)$$

$$v_{longitudinal}^{epi}(t) = \frac{dr_{longitudinal}^{epi}(t)}{dt} = -15\,\pi \sin(\frac{2\pi t}{T}) \quad (24)$$

The endocardial and epicardial longitudinal strain are calculated from equations 25 and 26 and measured in %.

$$\mathrm{S}_{radial\ longitudinal}^{endo}(\mathrm{t}) = 100\times \frac{\left(r_{longitudinal}^{endo}(t) - r_{longitudinal}^{endo}(0)\right)}{r_{longitudinal}^{endo}(0)} \quad (25)$$

$$\mathrm{S}_{longitudinal}^{epi}(\mathrm{t}) = 100\times \frac{\left(r_{longitudinal}^{epi}(t) - r_{longitudinal}^{epi}(0)\right)}{r_{longitudinal}^{epi}(0)} \quad (26)$$

Finally, the endocardial and epicardial longitudinal strain rates are calculated from equations 31 and 32, respectively, and measured in %/s.

$$Sr^{endo}_{longitudinal}(t) = 100\times \frac{v^{endo}_{longitudinal}(t)}{r^{endo}_{longitudinal}(t)} \quad (31)$$

$$Sr^{epi}_{longitudinal}(t) = 100\times \frac{v^{epi}_{longitudinal}(t)}{r^{epi}_{longitudinal}(t)} \quad (32)$$

For all models, analytical values, calculated from the motion equations, were compared to the experimental results from the FT software packages. Errors (%) were calculated as the root mean square of the difference between the analytical and the experimental values:

$$\varepsilon = 100\times \left[\frac{\sum(S(t) - S_0(t))^2}{\sum(St_0(t))^2}\right]^{\frac{1}{2}} \quad (33)$$

Where S_0(t) is the analytical value of a variable of interest (such as displacement, strain, or strain rate), and $S(t)$ is the corresponding measured value (101)(102).

However, the analytical circumferential parameters were zero and consequently, the errors for circumferential parameters were calculated from equation 34.

$$\varepsilon_{circumferential} = [\sum(S(t) - S_0(t))^2]^{\frac{1}{2}} \quad (34)$$

The first major contribution is I have extended the simulation model to include a long axis model to validate feature tracking which has not been done before to the best of our knowledge. The difference between the equations for short axis model used to validate the Tomtec software (3), and the modified equations are the inclusion of a new long-axis phantom model and the use of more realistic radii parameters to represent the real dimensions of the human heart in both the short-axis and long axis views. These real dimensions of the human heart are essential for development of software in short axis and long axis models. The introduction of endocardial and epicardial radii from real images as shown in Table 7.1, is to give the FT software a more human-like model to import into the FT software and analyse. The second major contribution is the introduction of different complex patterns of myocardial tissue which has not been explored previously (3)(99). These patterns were used to assess the accuracy of the derived results from FT

software packages with increasing levels of patterns complexity, and compare them to the uniform models in section 7.3.

7.3 Uniform Model

Figure 7.3: Example images from the uniform short axis model, the end-diastole on (left-hand side), and the end-systole on (right-hand side).

The first model was created with uniform intensity and no pattern in the myocardium. For this model, both short and long axis images were generated and analysed with two FT packages, Tomtec and CVI42.

7.3.1 Method

The images were created following the methodology developed in section 7.2.

Figure 7.4: Example images from the uniform long axis model, the end-diastole on (left-hand side), and the end-systole on (right-hand side).

The images for both, short axis and long axis models were composed of three intensity

defining three regions. First, the background intensity I_{bg} was set to zero. Second, the intensity in the annulus, representing the myocardial tissue was I_{myo} >0. The intensity appears as grey on the images. Finally, the blood pools were set to I_{bp}> I_{myo} and appears bright to mimic *in vivo* bSSFP images (Figure 7.1 and 7.2). The images were loaded in the software and analysed following the method described in Chapter 4. Example images of the with CVI42 analysis are displayed in Figure 7.5. Statistical analysis is described in Chapter 4 section.

7.3.2 Results and Discussion

The uniform short axis and long axis models results, derived from Tomtec and CVI42, as well as the errors between the peak values and overall curves are shown in Table 7.3 and Table 7.4; an error <10% can be considered to be acceptable (3). Example plots of the global parameters throughout the cardiac cycle for the short and long axis models are given in Figure 7.6.

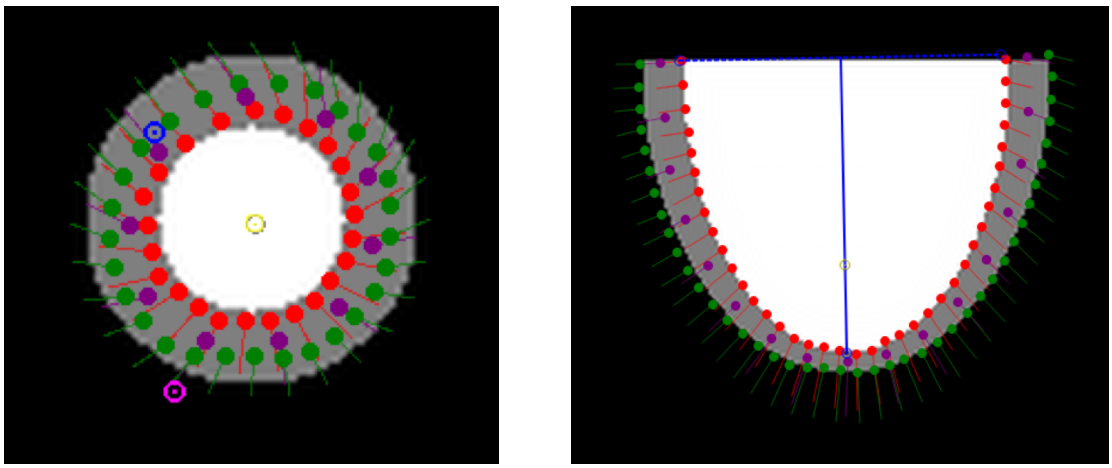

Figure 7.5: CVI42 FT tracking of the uniform short-axis (left-hand side) and long axis model (right-hand side) at frame 11 (systole). The green points show the tracking trajectory for the epicardial contour, whereas the red points show the tracking trajectory for the endocardial contour. A non-modelled circumferential motion (rotation) can be observed in the sort axis view.

The parameters to consider predominantly for comparison are displacement and strain. As velocity and strain rate are the derivatives of those two measurements, their errors will be amplified and higher than the errors for displacement and strain (3).

Overall, both software performed poorly when analysing the uniform models and were

ever hardly in agreement between them for global measurements; the only time was for circumferential strain but they were both incorrect.

Displacement:

Tomtec was the most accurate for radial displacement and was within 10% of the expected peak value for both models. The overall error was also within 10% for the short axis model and the curves were closely matched throughout the cardiac cycle (see Figure 7. 6A). Thanks to this good performance in measuring radial displacement, Tomtec was also accurate in assessing radial velocity in the short axis model. Although, CVI42 produced radial displacement curves with a more accurate overall appearance, especially on the long axis model, this software overestimated displacement by 16.9% for the short axis model and 24% for the long axis.

Table 7.3: Experimental and analytical values for global, endocardial and epicardial parameters using the uniform short axis model. Errors expressed in percentage (%) except for the circumferential parameters were the errors have corresponding units. Green cells = FT in agreement with analytical value (less than or equal to10% difference in peak value or less than or equal to 10% in error), yellow cells = 10% or less in difference in peak value between software.

Parameters			**Experimental results**		**Analytical values**	**Difference in peak value (%)**		**Errors**	
			Tomtec	**CVI42**		**Tomtec**	**CVI42**	**Tomtec**	**CVI42**
Radial displacement (mm)	Endo	P	6.8	7.9	10.0	-32.0	-21.0	31.3	21.3
	Epi	P	5.8	7.1	3.0	93.3	136.7	99.4	137.2
	G	P	6.3	7.6	6.5	-3.1	16.9	2.4	16.4
Radial velocity (mm/s)	Endo	P	23.1	31.2	31.0	-25.5	0.6	30.3	26.2
		RP	-20.9	-31.2	-31.0	32.6	-0.6		
	Epi	P	19.3	28.1	9.0	114.4	212.2	104.0	150.6
		RP	-20.2	-28.1	-9.0	-124.4	-212.2		
	G	P	21.2	29.8	20.0	6.0	49.0	8.3	166.2
		RP	-20.5	-29.8	-20.0	-2.5	-49.0		
Radial strain (%)	Endo	P	NA	51.9	40.0	NA	29.8	NA	22.8
	Epi	P	NA	38.4	10.0	NA	284.0	NA	259.5
	G	P	20.4	45.5	25.0	-18.4	82.0	33.3	69.1
Radial strain rate (%/s)	Endo	P	NA	195.7	127.0	NA	54.1	NA	53.8
		RP	NA	-195.7	-127.0	NA	-54.1		
	Epi	P	NA	139.0	31.5	NA	341.3	NA	308.5
		RP	NA	-139.0	-31.5	NA	-341.3		
	G	P	65.1	170.5	79.0	-17.6	115.8	58.6	102.4
		RP	-77.0	-170.5	-79.0	2.5	-115.8		
Circumferential displacement (deg)	Endo	RP	-0.1	-0.5	0	ND	ND	7.2	1.3
	Epi	RP	-0.1	-0.5	0	ND	ND	26.6	1.2
	G	RP	-0.1	-0.5	0	ND	ND	15.9	1.2
Circumferential velocity (deg/s)	Endo	P	26.1	4.2	0	ND	ND	61.6	12.5
		RP	-20.9	-10.5	0	ND	ND		
	Epi	P	38.5	4.1	0	ND	ND	112.9	11.9
		RP	-57.4	-10.1	0	ND	ND		
	G	P	23.1	4.1	0	ND	ND	65.7	12.1
		RP	-31.6	-10.2	0	ND	ND		
Circumferential strain (%)	Endo	RP	-26.0	-25.4	0	ND	ND	72.0	71.2
	Epi	RP	-18.3	-21.7	0	ND	ND	52.1	60.8
	G	RP	-22.2	-23.7	0	ND	ND	62.0	66.3

Endo = endocardial, Epi = epicardial, G = global, P = peak, RP = reverse peak, NA = not available, ND = not defined.

Table 7.4: Experimental and analytical values for global, endocardial and epicardial parameters using the uniform long axis model. Errors expressed in percentage (%). Green cells = FT in agreement with analytical value (less than or equal to10% difference in peak value or less than or equal to 10% in error), yellow cells = 10% or less in difference in peak value between software.

Parameters			Experimental results		Analytical values	Difference in peak value (%)		Error (%)	
			Tomtec	CVI42		Tomtec	CVI42	Tomtec	CVI42
Radial displacement (mm)	Endo	P	6.3	9.5	7.0	-10.0	35.7	15.1	34.2
	Epi	P	9.3	9.1	8.0	16.3	13.8	23.9	12.6
	G	P	7.8	9.3	7.5	4.0	24.0	17.0	23.1
Radial velocity (mm/s)	Endo	P	33.7	29.2	22.0	53.2	32.7	60.7	39.9
		RP	-31.4	-29.2	-22.0	-42.7	-32.7		
	Epi	P	37.5	28.5	25.0	50.0	14.0	41.7	21.8
		RP	-36.3	-28.5	-25.0	-45.2	-14.0		
	G	P	35.6	28.9	24.0	48.3	20.4	47.4	30.0
		RP	-32.7	-28.9	-24.0	-36.3	-20.4		
Radial strain (%)	Endo	P	NA	11.9	12.7	NA	-6.3	NA	17.2
	Epi	P	NA	10.1	11.8	NA	-14.4	NA	19.8
	G	P	-19.9	11.0	12.2	-263.1	-9.8	219.3	16.9
Radial strain rate (%/s)	Endo	P	NA	47.3	43.0	NA	10.0	NA	30.2
		RP	NA	-47.3	-43.0	NA	-10.0		
	Epi	P	NA	43.1	39.0	NA	10.5	NA	24.7
		RP	NA	-43.1	-39.0	NA	-10.5		
	G	P	138.0	45.5	41.0	236.6	11.0	314.0	26.6
		RP	-144.0	-45.5	-41.0	-251.2	-11.0		
Longitudinal displacement (mm)	Endo	RP	-9.8	-1.6	-16.0	38.8	90.0	66.6	90.8
	Epi	RP	-6.6	-1.8	-15.0	56.0	88.0	72.1	92.0
	G	RP	-8.2	-1.7	-15.5	47.1	89.0	68.9	91.4
Longitudinal velocity (mm/s)	Endo	P	81.9	7.9	50.0	63.8	-84.2	102.5	91.5
		RP	-80.2	-7.0	-50.0	-60.4	86.0		
	Epi	P	55.0	7.2	47.0	17.0	-84.7	90.1	92.6
		RP	-59.9	-7.2	-47.0	-27.4	84.7		
	G	P	66.4	7.5	49.0	35.5	-84.7	95.0	92.1
		RP	-69.9	-7.5	-49.0	-42.7	84.7		
Longitudinal strain (%)	Endo	RP	-11.4	-9.4	-16.0	28.8	41.3	103.1	45.7
	Epi	RP	-15.0	-8.3	-14.3	-4.9	42.0	11.5	101.6
	G	RP	-12.2	-9.0	-15.1	19.2	40.4	52.1	44.4
Longitudinal strain rate (%/s)	Endo	P	201.0	32.0	55.0	265.5	-41.8	190.4	47.1
		RP	-164.0	-32.0	-55.0	-198.2	41.8		
	Epi	P	263.0	29.7	48.0	447.9	-38.1	246.5	45.0
		RP	-217.0	-29.7	-48.0	-352.1	38.1		
	G	P	158.0	30.8	51.0	209.8	-39.6	133.2	45.4
		RP	-162.0	-30.8	-51.0	-217.6	39.6		

Endo = endocardial, Epi = epicardial, G = global, P = peak, RP = reverse peak, NA = not available.

Both software introduced a small circumferential displacement in the short axis model, although the overall error was still acceptable for CVI42.

Finally, the two software were inadequate in estimating longitudinal displacement, CVI42 could hardly pick any changes while Tomtec computed both positive and negative displacement when only the latter existed (Figure 7.6C).

Strain:

Both software packages were particularly poor at computing strain values from the simulated images. Only the global radial peak strain calculated by CVI 42 from the long axis model was within the 10% acceptable range. However, its overall error was nearing 17%. Although the values were incorrect, the overall shapes of the strain curves produced by CVI42 were realistic. This was not the case for Tomtec especially for the long axis model (Figure 7.6 E-F).

Both FT software packages measured non-zero circumferential parameters even though no circumferential motion was simulated, *i.e*. there was no in-plane rotation. These errors could be related to; i) intrinsic algorithm errors (small scale errors) or ii) model factors (larger scale errors). For instance, the modelled uniform myocardium signal intensity might have lacked sufficient features for FT software packages to correctly track the moving contours. This could also explain why a circumferential motion was measured by both software as a uniform disk area (the myocardium) has an infinite rotational symmetry. In order to add features to the myocardium a radial pattern was simulated; this is discussed in the next section.

7.4 Radial model

FT techniques rely on variation in signal intensities, changes in texture and patterns, as well as the endocardial and epicardial edges to compute displacement and strain.

Therefore, in this section, to improve on some of the limitations of the previous uniform numerical phantom, a textured pattern was used in the myocardial tissue for both the short axis and long axis models. In this case, a radial pattern of varying signal intensities was created. Simulated images were then analysed with both FT software packages and the results compared to the analytical motion parameters.

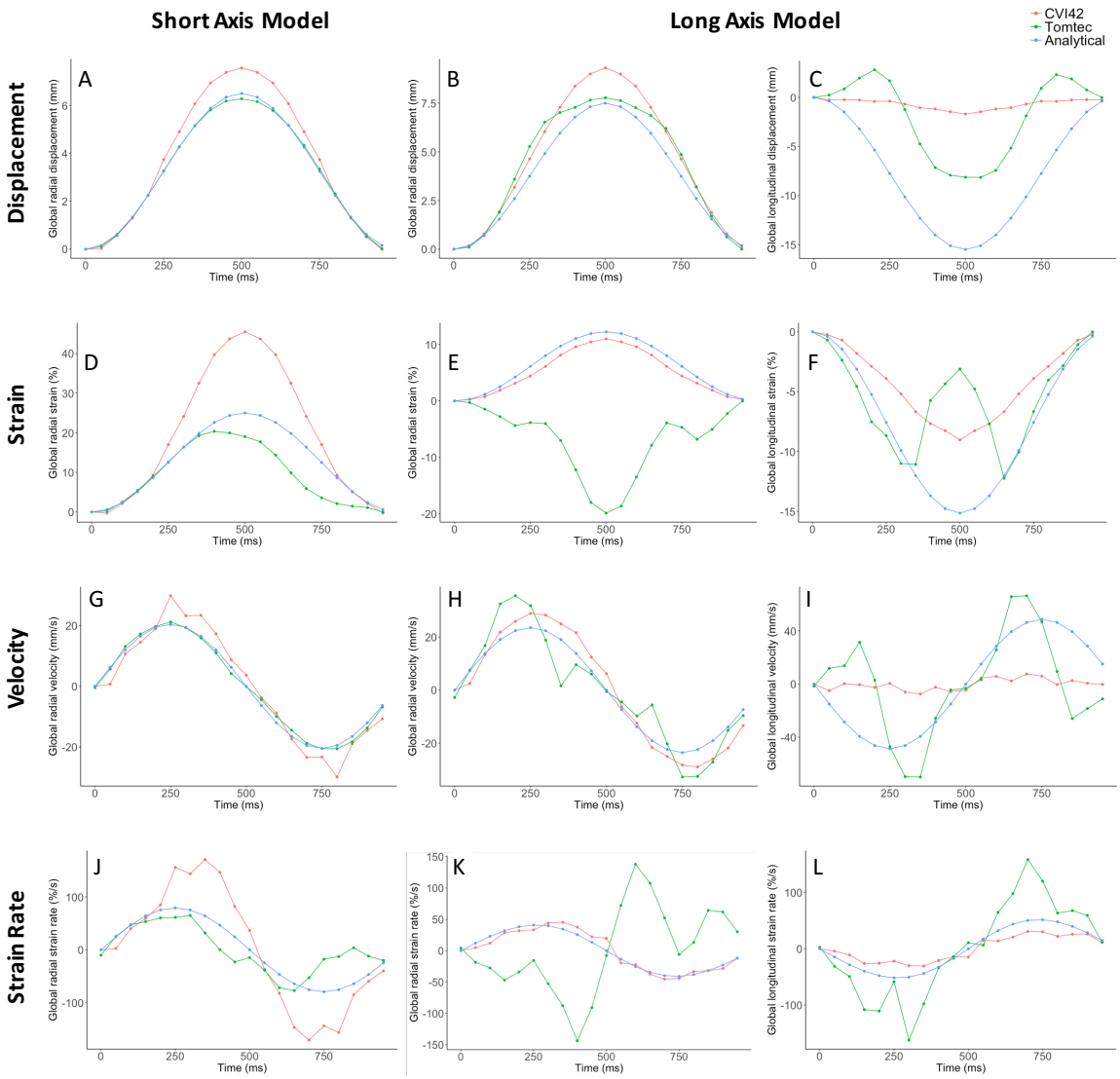

Figure 7.6: Experimental and analytical plots for global parameters for the short and long axis uniform models. (A-C) displacement, (D-F) strain, (G-I) velocity radial and (J-L) strain rate.

7.4.1 Method

The main aim of using a simple radial pattern as the myocardial tissue signal intensity was to investigate whether these features were able to better constrain and reduce the

measured circumferential motion (rotation), which was modelled as zero. Additionally, could the pattern improve the overall tracking in both radial and longitudinal directions. As an initial step, the radial patterns were modelled to contract without any circumferential motion (rotation).

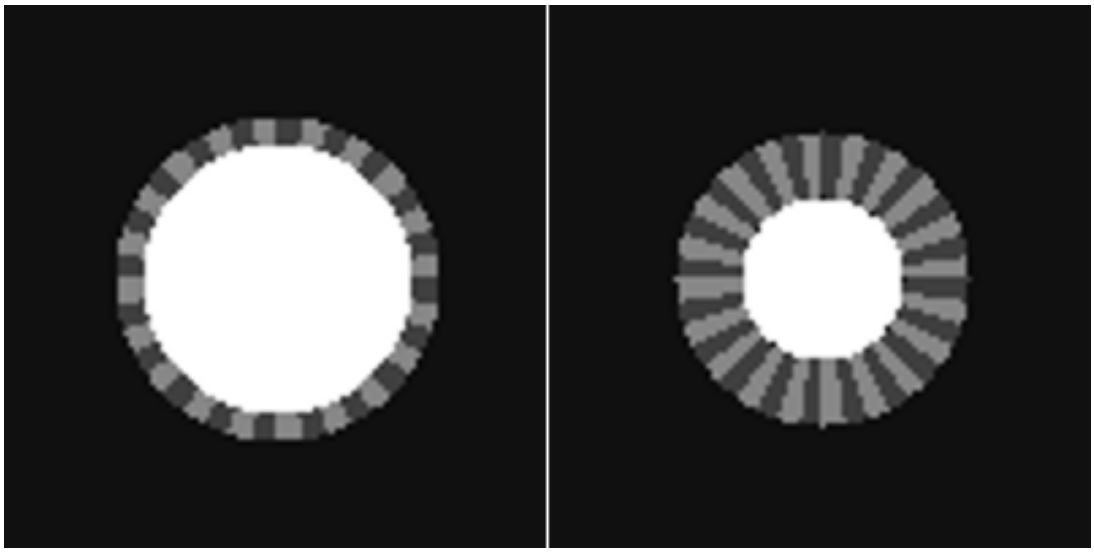

Figure 7.7: Example images from the radial short-axis model for σ = 1 and N_{spokes} = 40. The end-diastole (left-hand side), and end-systole (right-hand side) images are shown.

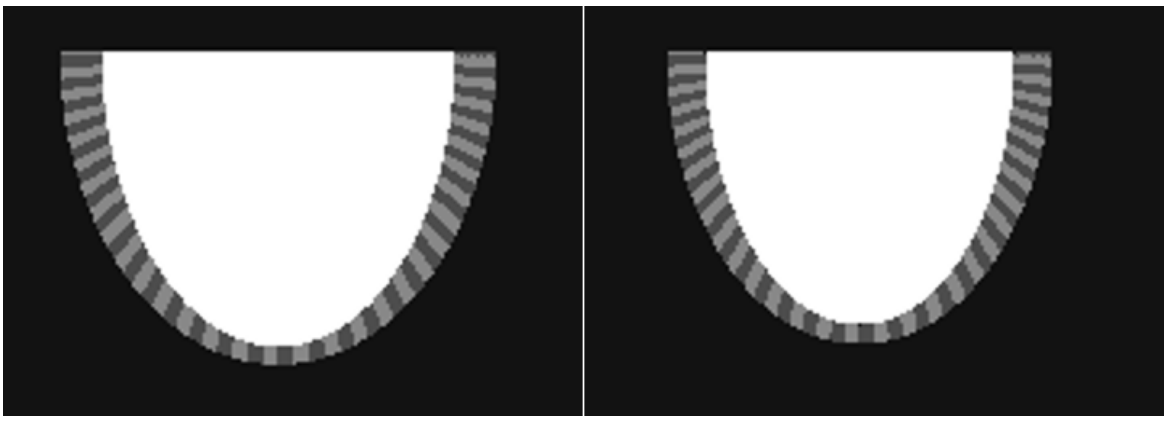

Figure 7.8: Example images from the radial long axis model for σ = 1 and N_{spokes} = 60. The end-diastole (left-hand side), and the end-systole (right-hand side) images are shown.

The radial patterns were modelled to deform radially with the endocardial and epicardial contours during one complete motion cycle representing one RR interval. Mathematically speaking, the patterns can be generated as a multiplication of two sine functions (equations 35 and 36). The first function depends on the radius (*r)* and the number of selected radial rings (σ), while the second equation is a function of the angle (θ) and the number of radial spokes (N_{spokes}) or lines.

$$f_1(\mathrm{r}) = \sin(r * \sigma) \quad (35)$$

$$f_2(\theta) = \sin(\theta * N_{spokes}) \quad (36)$$

The variables σ and N_{spokes} control the pattern appearance as shown in Figures 7.7 and 7.8 for the short and long axes models, respectively. For the short axis (Figure 7.7), both variables were set to σ =1, and N_{spokes} = 40 spokes to cover the entire myocardium. While for the long axis (Figure 7.10), contained σ =1, and N_{spokes} = 60 radial spokes to cover the entire semi-ellipse. In both models, the signal intensity of myocardium tissue ($\boldsymbol{r}_{\boldsymbol{radial}}^{\boldsymbol{endo}}(\mathbf{t}) < \boldsymbol{r}(\boldsymbol{t}) < \boldsymbol{r}_{\boldsymbol{radial}}^{\boldsymbol{epi}}(\mathbf{t})$) I_{myo} varied circumferentially, whereas the intensity is the same radially. The same background (I_{bg}) and blood pool signal (I_{bp}) signal intensities as the uniform model were used and the radial short-axis is still modelled to contract radially only, while the radial long axis is modelled to contract radially and longitudinally.

7.4.2 Results and discussion

The radial short axis and long axis models results derived from FT software packages as well the errors between the peak values and overall curves are given in Table 7.5 for the short axis and Table 7.6 for the long axis model. Example frames from the analysis of the short and long axis using CVI42 is shown in Figure 7.9 while plots for global displacements and global strains throughout the cardiac cycle are displayed in Figure 7.10.

Overall, both software performed poorly especially for the long axis model with no agreement with the analytical values. In terms of global measurements, both software only agreed on three parameters all calculated from the short axis model: radial displacement, radial reverse peak velocity and radial strain. However, out of those three parameters only CVI42 agreed with the analytical peak value for displacement but none had an acceptable overall error. As in the uniform model, both software computed non-

zero circumferential parameters when no rotation was simulated.

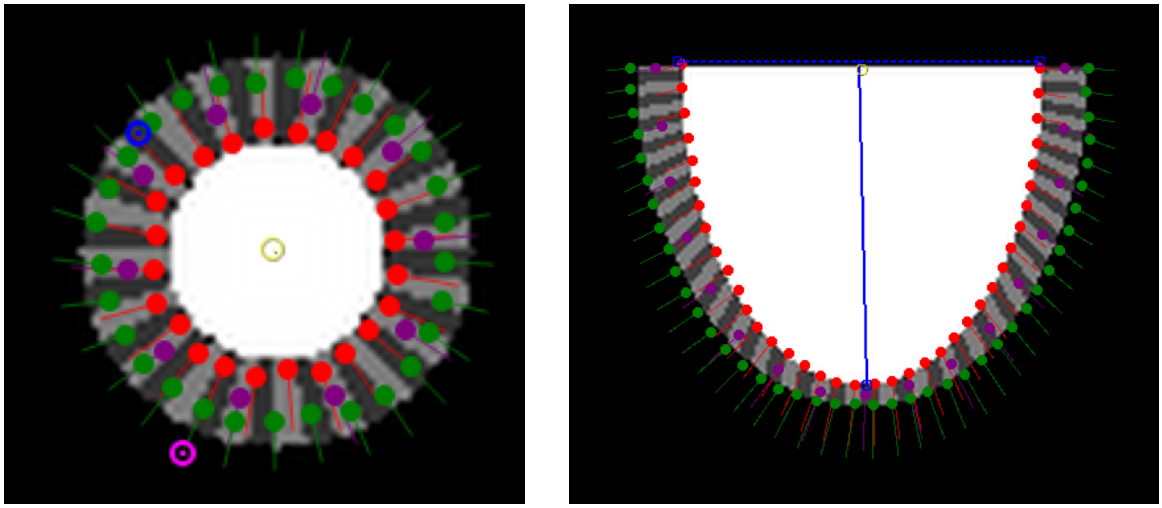

Figure 7.9: CVI42 FT tracking of the radial short-axis (left-hand side) and long axis model (right-hand side) at frame 11 (systole). The green points show the tracking trajectory for the epicardial contour, whereas the red points show the tracking trajectory for the endocardial contour. A small non-modelled circumferential motion (rotation) can still be observed in the sort axis view.

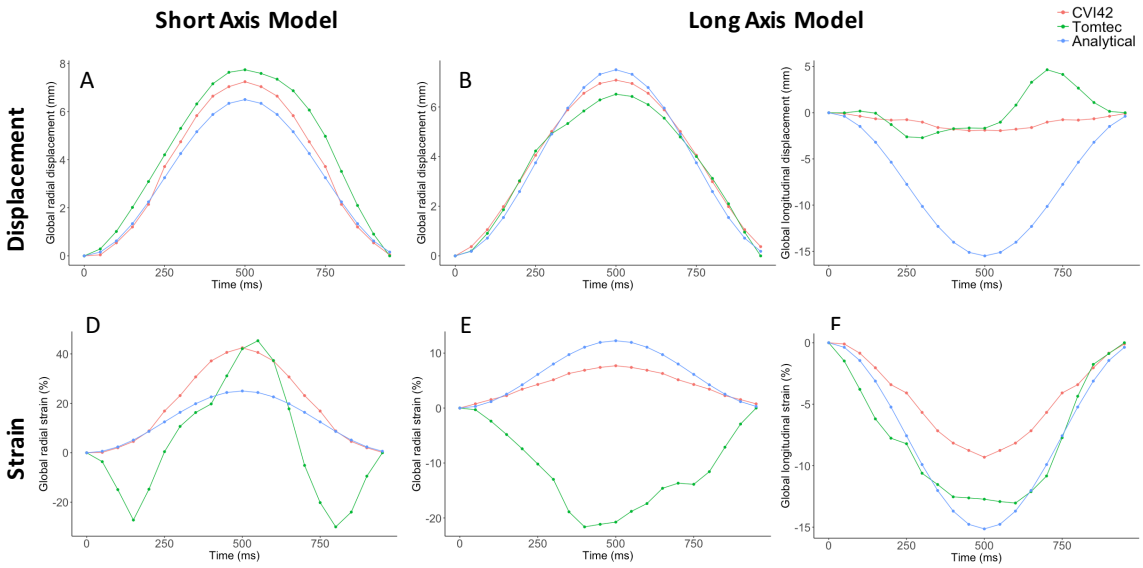

Figure 7.10: Experimental and analytical plots for global displacement (A-C) and global strain (D-F) for the short and long axis radial models.

Displacement:

Both software produced realistic radial displacement curves for the two models (Figures

7.10A and 7.10B). However, the peak values were overestimated in the short axis and underestimated in the long axis. In both cases, CVI42 performed better for both short and long axis models and the error in peak value (10.8%) and the overall error (12%) were just outside the acceptable rage. Similarly to the uniform model, both software struggled with longitudinal displacement; CVI42 grossly underestimated it, and once more calculated near zero displacement throughout the cardiac cycle while Tomtec produced unrealistic tracking plots (Figure 7.10C). Finally, both software introduced a circumferential displacement, although this was once again acceptable for CVI42 (2.5%).

Strain:

The introduction of the radial pattern did not lead to a better agreement when measuring radial strain with the short axis model with both software generating unacceptable errors. However, for the long axis model errors improved and for CVI42 the difference in peak value was acceptable (-1.6%) and the overall error slightly above the acceptable range (11.7%).

Overall, the addition of the radial pattern did little to improve the performance of the software. Once more both software performed best for radial displacement with CVI42 outperforming Tomtec and also producing acceptable values for long axis radial strain. All the other strain measurements were inadequate and once more, both software introduced a rotational component to the movement and the value associated with it did not improved compared to the uniform model. In the next section, the complexity of the simulations was further increased by introducing two sets of perpendicular lines forming a checkerboard pattern in the myocardium.

Table 7.5: Experimental and analytical values for global, endocardial and epicardial parameters using the radial short axis model. Errors expressed in percentage (%) circumferential parameters were the errors have corresponding units. Green cells = FT in agreement with analytical value (less than or equal to10% difference in peak value or less than or equal to 10% in error), yellow cells = 10% or less in difference in peak value between software.

Parameters			**Experimental results**		**Analytical values**	**Difference in peak value (%)**		**Error (%)**	
			Tomtec	**CVI42**		**Tomtec**	**CVI42**	**Tomtec**	**CVI42**
Radial displacement (mm)	Endo	P	8.5	7.6	10.0	-15.0	-24.0	15.5	24.4
	Epi	P	7.0	6.8	3.0	133.3	126.7	169.8	128.3
	G	P	7.7	7.2	6.5	18.5	10.8	27.9	12.0
Radial velocity (mm/s)	Endo	P	27.3	32.9	31.0	-11.9	6.1	14.8	29.9
		RP	-31.8	-32.9	-31.0	-2.6	-6.1		
	Epi	P	23.1	29.7	9.0	156.7	230.0	186.8	144.6
		RP	-34.2	-29.7	-9.0	-280.0	-230.0		
	G	P	23.4	31.4	20.0	17.0	57.0	38.2	31.8
		RP	-31.8	-31.4	-20.0	-59.0	-57.0		
Radial strain (%)	Endo	P	NA	48.4	40.0	NA	21.0	NA	16.5
	Epi	P	NA	36.2	10.0	NA	262.0	NA	240.1
	G	P	45.3	42.5	25.0	81.2	70.0	123.2	58.8
Radial strain rate (%/s)	Endo	P	NA	180.1	127.0	NA	41.8	NA	46.3
		RP	NA	-180.1	-127.0	NA	-41.8		
	Epi	P	NA	141.8	31.5	NA	350.2	NA	285.7
		RP	NA	-141.8	-31.5	NA	-350.2		
	G	P	361.4	162.2	79.0	357.5	105.3	386.4	89.8
		RP	-482.0	-162.2	-79.0	-510.1	-105.3		
Circumferential displacement (deg)	Endo	RP	-0.9	-0.7	0	ND	ND	28.4	2.5
	Epi	RP	-4.2	-0.7	0	ND	ND	17.7	2.5
	G	RP	-2.1	-0.7	0	ND	ND	22.5	2.5
Circumferential velocity (deg/s)	Endo	P	123.9	7.2	0	ND	ND	220.8	12.9
		RP	-77.1	-7.2	0	ND	ND		
	Epi	P	62.7	7.3	0	ND	ND	132.0	13.1
		RP	-48.8	-7.3	0	ND	ND		
	G	P	93.3	7.2	0	ND	ND	167.3	12.9
		RP	-62.9	-7.2	0	ND	ND		
Circumferential strain (%)	Endo	RP	-33.1	-24.6	0	ND	ND	88.1	68.9
	Epi	RP	-24.5	-20.9	0	ND	ND	71.9	58.8
	G	RP	-27.8	-22.8	0	ND	ND	79.7	64.1

Endo = endocardial, Epi = epicardial, G = global, P = peak, RP = reverse peak, NA = not available. ND = not defined.

Table 7.6: Experimental and analytical values for global, endocardial and epicardial parameters using the radial long axis model. Errors expressed in percentage (%). Green cells = FT in agreement with analytical value (less than or equal to10% difference in peak value or less than or equal to 10% in error), yellow cells = 10% or less in difference in peak value between software.

Parameters			**Experimental results**		**Analytical values**	**Difference in peak value (%)**		**Error (%)**	
			Tomtec	**CVI42**		**Tomtec**	**CVI42**	**Tomtec**	**CVI42**
Radial displacement (mm)	Endo	P	10.6	9.4	7.0	51.4	34.3	54.3	33.8
	Epi	P	10.3	8.9	8.0	28.8	11.3	29.9	11.3
	G	P	10.5	9.2	7.5	40.0	22.7	41.1	21.8
Radial velocity (mm/s)	Endo	P RP	41.3 -38.2	29.0 -29.0	22.0 -22.0	87.7 -73.6	31.8 -31.8	73.1	39.5
	Epi	P RP	38.4 -32.6	28.1 -28.1	25.0 -25.0	53.6 -30.4	12.4 -12.4	43.9	20.8
	G	P RP	39.8 -35.4	28.5 -28.5	24.0 -24.0	65.8 -47.5	18.8 -18.8	56.5	28.8
Radial strain (%)	Endo	P	NA	13.1	12.7	NA	3.1	NA	10.9
	Epi	P	NA	11.0	11.8	NA	-6.8	NA	13.3
	G	P	9.5	12.1	12.3	-22.8	-1.6	47.8	11.7
Radial strain rate (%/s)	Endo	P RP	NA NA	49.2 -49.2	43.0 -43.0	NA NA	14.4 -14.4	NA	27.8
	Epi	P RP	NA NA	43.3 -43.3	39.0 -39.0	NA NA	11.0 -11.0	NA	24.5
	G	P RP	85.0 -59.0	46.3 -46.3	41.0 -41.0	107.3 -43.9	12.9 -12.9	97.9	25. 6
Longitudinal displacement (mm)	Endo	RP	-2.8	-2.0	-16.0	82.5	87.5	94.7	87.4
	Epi	RP	-2.7	-1.8	-15.0	82.0	88.0	108.6	87.9
	G	RP	-2.8	-1.9	-15.5	81.9	87.7	101.3	87.6
Longitudinal velocity (mm/s)	Endo	P RP	49.9 -46.6	11.9 -11.9	50.0 -50.0	-0.2 6.8	-76.2 76.2	105.2	88.9
	Epi	P RP	50.4 -43.8	11.6 -11.6	47.0 -47.0	7.2 6.8	-75.3 75.3	126.5	89.5
	G	P RP	50.2 -35.7	11.8 -11.8	49.0 -49.0	2.4 27.1	-75.9 75.9	114.4	89.2
Longitudinal strain (%)	Endo	RP	-15.5	-9.9	-16.0	3.1	38.1	19.1	41.5
	Epi	RP	-10.9	-8.7	-14.3	23.8	39.2	24.2	43.4
	G	RP	-13.0	-9.3	-15.1	13.9	38.4	15.9	40.7
Longitudinal strain rate (%)	Endo	RP P	16.7 -18.9	33.9 -33.9	55.0 -55.0	-69.6 65.6	-38.4 38.4	202.6	41.0
	Epi	RP P	93.0 -67.0	31.0 -31.0	48.0 -48.0	93.8 -39.6	-35.4 35.4	69.1	43.7
	G	RP P	87.0 -128.0	32.4 -32.4	51.0 -51.0	70.6 150.9	-36.5 36.5	122.2	43.8

Endo = endocardial, Epi = epicardial, G = global, P = peak, RP = reverse peak, and NA = not available.

7.5 Checkerboard Short Axis Model

In the radial pattern model, intensities varied only circumferentially, however, in this section the aim was to create a more structured patterns or texture where the intensities varied circumferentially as well as radially. As the motion of a checkerboard pattern is complex to generate for a long axis only a short axis numerical phantom was created in this section.

7.5.1 Method

A short axis model using a checkerboard pattern was modelled to contract radially and to deform with the endocardial and epicardial contours. A Checkerboard pattern can be generated by using the same equations (35 and 36) introduced in the previous model (section 7.4.1). Obtaining a checkerboard pattern can easily be done by using a $\sigma > 1$ value, i.e. having more than one concentric rings within the myocardial area. The number of radial spokes (N_{spokes}) variable still determines the number of total radial sectors. Myocardial signal intensities were varied both radially and circumferentially to create the final checkerboard pattern (see Figure 7.12). Two signal intensities were chosen I^1_{myo} and I^2_{myo}, with $I_{bg} < I^1_{myo} < I^2_{myo} < I_{bp}$. Although the pattern varies circumferentially, there is no circumferential movement like in the previous two models.

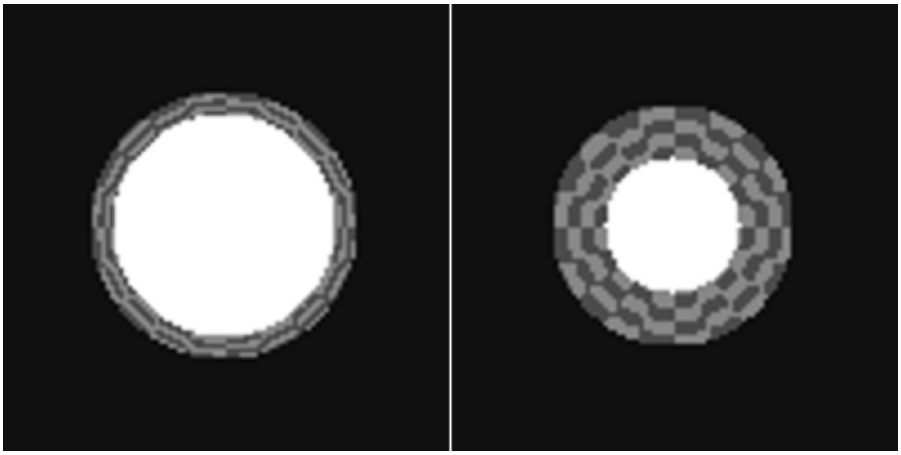

Figure 7.11: Example images from the checkerboard short-axis model for $\sigma = 4$ and $N_{spokes} = 20$. The end-diastolic phase (left-hand side), and the end-systolic phase (right-hand side) are shown.

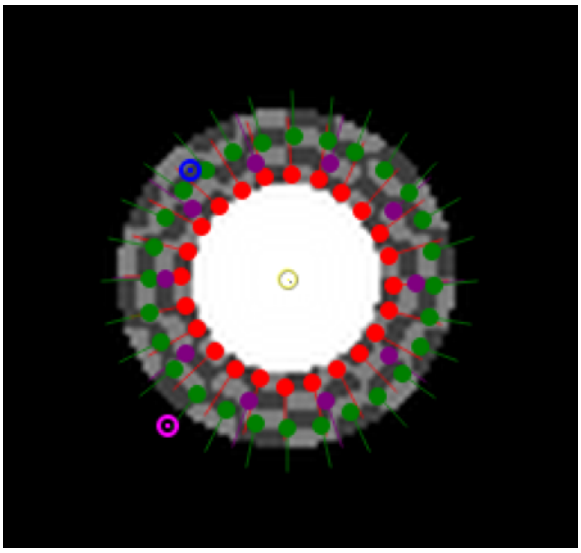

Figure 7.12: CVI42 FT tracking of the uniform short-axis (left) and long axis model (right) at frame 11 (systole). The green points show the tracking trajectory for the epicardial contour, whereas the red points show the tracking trajectory for the endocardial contour. A small non-modelled circumferential motion (rotation) is observed in the sort-axis view.

7.5.2 Results and discussion

The checkerboard short axis model results, derived from Tomtec and CVI42, as well as the errors between the peak values and the overall curves are displayed in Table 7.7. Curves for all four global parameters are displayed in Figure 7.13.

As for the previous two models, there was little agreement between software. In this case, they did not agree on a single global measurement.

Displacement:

Both software produced realistic displacement curves, however, CVI42 overestimated displacement by approximately 18% while Tomtec underestimated it by approximately 55%. In the case of CVI42, this was similar to the uniform model (16.9% peak error, 16.4% overall) but worth than the radial model (10.8% peak error, 12.0% overall). In the case of Tomtec, the checkboard pattern gave worth displacement results than the radial pattern that in turn was worth than the uniform model (overall errors of 55.7, 27.9 and 2.4% respectively).

Table 7.7: Experimental and analytical values for global, endocardial and epicardial parameters using checkerboard short axis model. Errors expressed in percentage (%) except for the circumferential parameters were the errors have corresponding units. Green cells = FT in agreement with analytical value (less than or equal to10% difference in peak value or less than or equal to 10% in error), yellow cells = 10% or less in difference in peak value between software.

Parameters			**Experimental results**		**Analytical values**	**Difference in peak value (%)**		**Errors (%)**	
			Tomtec	**CVI42**		**Tomtec**	**CVI42**	**Tomtec**	**CVI42**
Radial displacement (mm)	Endo	P	2.9	8.0	10.0	-71.0	-20.0	69.1	20.4
	Epi	P	2.7	7.2	3.0	-10.0	140.0	12.0	140.2
	G	P	2.9	7.7	6.5	-55.4	18.5	55.7	17.5
Radial velocity (mm/s)	Endo	P	10.3	30.2	31.0	-66.8	-2.6	69.4	25.3
		RP	-11.1	-30.2	-31.0	64.2	2.6		
	Epi	P	8.9	27.5	9.0	-1.1	205.6	22.5	149.1
		RP	-8.9	-27.5	-9.0	1.1	-205.6		
	G	P	9.6	28.9	20.0	-52.0	44.5	55.7	29.5
		RP	-8.4	-28.9	-20.0	58.0	-44.5		
Radial strain (%)	Endo	P	NA	52.9	40.0	NA	32.3	NA	24.2
	Epi	P	NA	39.6	10.0	NA	296.0	NA	268.9
	G	P	14.8	46.6	25.0	-40.8	86.4	53.1	72.3
Radial strain rate (%/s)	Endo	P	NA	177.8	127.0	NA	40.0	NA	54.6
		RP	NA	-177.8	-127.0	NA	-40.0		
	Epi	P	NA	133.8	31.5	NA	324.8	NA	314.7
		RP	NA	-133.8	-31.5	NA	-324.8		
	G	P	45.4	158.3	79.0	-42.5	100.4	90.3	104.2
		RP	-77.9	-158.3	-79.0	1.4	-100.4		
Circumferential displacement (deg)	Endo	P	-2.8	-2.0	0	ND	ND	6.9	3.9
	Epi	P	-1.9	-1.9	0	ND	ND	5.4	3.9
	G	P	-2.5	-1.9	0	ND	ND	5.9	3.9
Circumferential velocity (deg/s)	Endo	P	38.1	27. 8	0	ND	ND	92.5	56.7
		RP	-40.4	-40.1	0	ND	ND		
	Epi	P	20.3	27.4	0	ND	ND	49.1	56.2
		RP	-21.8	-39.9	0	ND	ND		
	G	P	27.3	27.6	0	ND	ND	66.6	56.4
		RP	-31.1	-39.9	0	ND	ND		
Circumferential strain (%)	Endo	RP	-12.9	-25.7	0	ND	ND	37.4	71.9
	Epi	RP	-9.3	-22.1	0	ND	ND	25.1	61.9
	G	RP	-11.1	-23.9	0	ND	ND	31.2	67.2

Endo = endocardial, Epi = epicardial, G = global, P = peak, RP = reverse peak, NA = not available, ND = not defined.

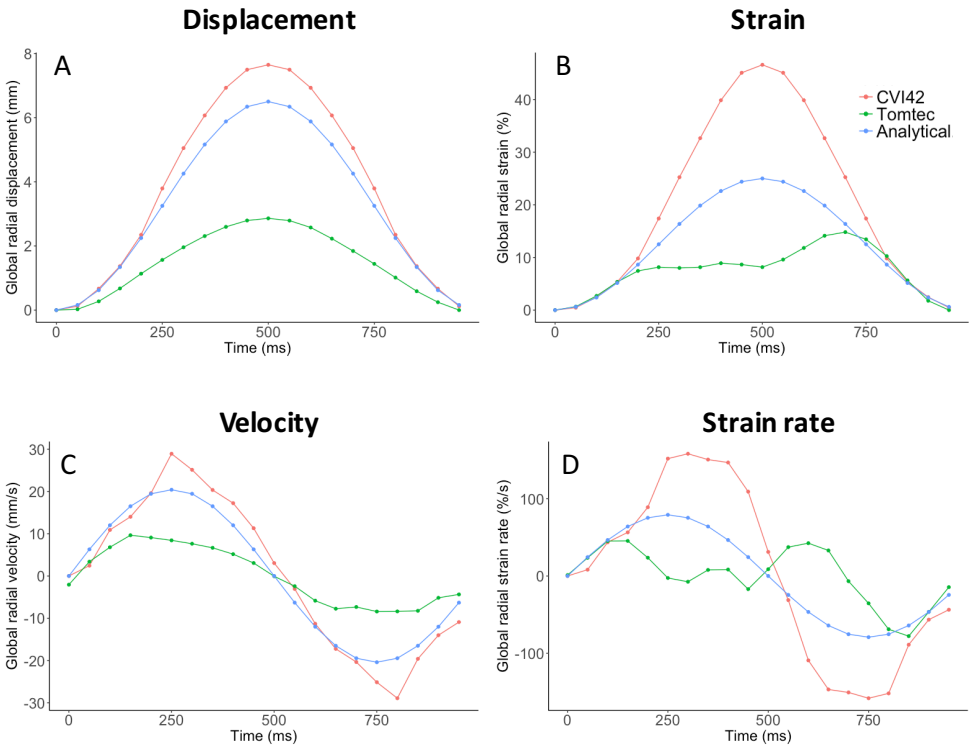

Figure 7.13: Experimental and analytical plots for global parameters for the short axis checkerboard model; (A) displacement, (B) strain, (C) velocity radial and (D) strain rate.

As with previous models, both software detected a small circumferential displacement in the checkerboard short axis model. However, this time the error was acceptable for both software as opposed to only acceptable for CVI42 in the previous two models.

Strain:

Both software packages gave inadequate results for circumferential strain. Although the curve produced by CVI42 was once more realistic in terms of appearance the peak value was grossly overestimated (86.4%) leading to an overall error of 72.3%. Tomtec produced an unrealistic curve, underestimated the peak value by 40.8% and had an overall error of 53.1%.

As with the uniform and radial pattern models, both software calculated a non-zero circumferential strain when no rotation had been simulated. For CVI42, the calculated strain was almost identical to the previous two models, however, the error was halved for Tomtec when compared to the uniform model; 31.2% for the checkerboard compared to 62% for the uniform model (see also figure 7.14C & D).

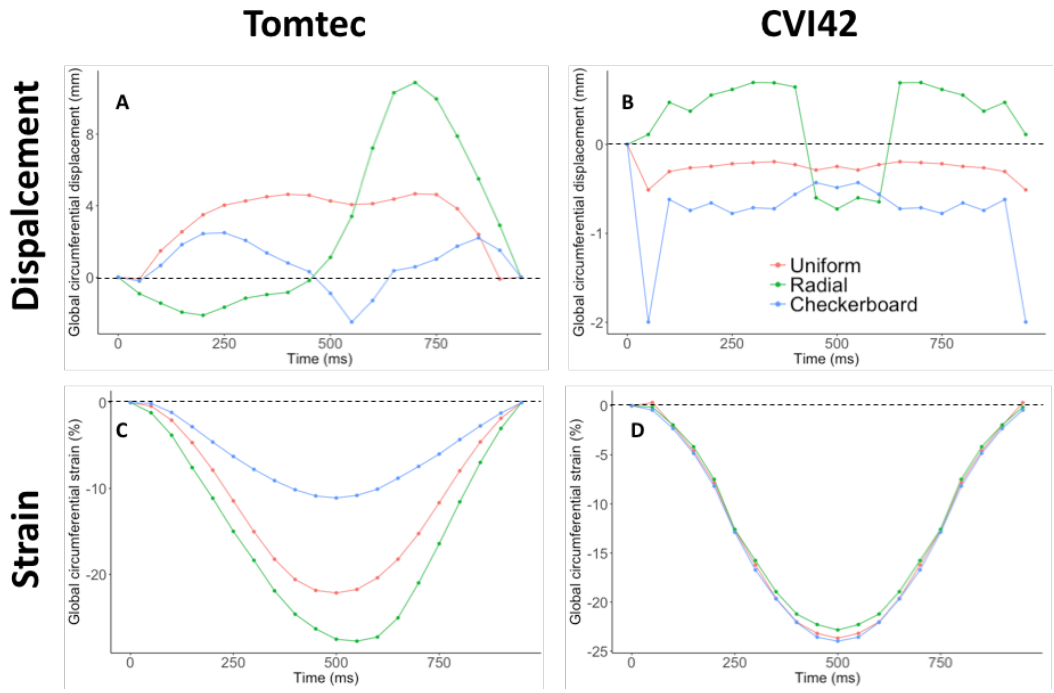

Figure 7.14: Circumferential displacement and circumferential strain computed by both software for the different numerical models. For all simulation, rotation was set to zero and consequently, displacement and strain should have been equal to zero throughout the cardiac cycle (dashed line).

7.6 General Discussion

Prior knowledge of the exact motion and deformation parameters acting as a ground truth is essential for the development of FT software packages validation to assess precision and accuracy. A similar approach was used in the ongoing standardisation efforts and validation processes to reduce inter-vendor variability of the measurements across software packages for 2D speckle tracking echocardiography based on synthetic ultrasound data (99). However, only one study so far, used numerical simulations to validate a commercial FT software (Tomtec) (3).In this case, a range of uniform short axis models contracting only radially were generated to investigate the effects of varying spatial resolution, frame rate and the number of points used to track the endocardium. To build on this work, this chapter compared the deformation parameters measured by Tomtec and CVI42 software packages (experimental results) to the analytical values (gold-standard) of five different numerical motion models; uniform myocardial intensity

and radial pattern models for a short and a long axis view and a short-axis checkerboard myocardial pattern numerical phantom. Unlike the previous published work (3), my primary interest was not to investigate the effect of specific image parameters but to gradually work towards a realistic model with fixed image parameters for the different simulations.

Although, the different model results in sections 7.3.2, 7.4.2. and 7.5.2 focussed on global displacements and strains for their respective models, this general discussion looks more specifically at trends with the increasing model complexity and touches on some of the other parameters.

It is fair to say that both software struggled to analyse the models and the experimental values hardly ever agreed with the analytical values (Tables 7.3 to 7.7). This was not only the case for the global parameters but also for the epi and endocardial borders. This, at first, can look unexpected as those are such well-defined borders in terms of intensity transitions, however, it is possible that the tracking algorithms expect more anatomical features and not such smooth edges. One could think of making edges more realistic and adding papillary muscles to the model to test this hypothesis.

Although both software packages were inaccurate for most calculations, it is worth highlighting that CVI42 always produced realistic parameter curves whereas, except for the short axis displacements, Tomtec generated unrealistic curves that often lacked the expected symmetry.

Disagreement between numerical simulations and values calculated from commercial software have also been observed for 2D speckle tracking echocardiography (99). In this study, comparing global longitudinal strain between 9 vendors, some underestimated it compared to the analytical values, while others overestimated it. Like in the results observed in this chapter, it can be challenging to know if software packages are purely and simply inaccurate or if the models are not realistic enough for the algorithm to

function correctly. A clear demonstration of this is the presence of non-zero circumferential parameters for all short axis models in the results of both software when no rotation was simulated. Interestingly, the circumferential strain curves produced by both software models are very similar and physiologically realistic (Figure 7.14 C-D). The introduction of geometric patterns to the simulated myocardium has no effect on the strain output of CVI42 (Figure 7.14D) while the error reduces greatly with the use of a checkerboard pattern for Tomtec (Figure 7.14C). This seem to indicate that both software expect a rotational component and in its absence revert to a "physiological" output. One can speculate that the starting point of the algorithm is that physiological output that is altered to represent the actual displacement and strain. It is hard to estimate the effect of the absence of rotational component has on the correct calculation of the other parameters as we have no details on the algorithm used. However, it is clear from those results that a model should include this motion component in order to correctly assess the current FT commercial software packages.

7.7 Conclusion

Numerical simulation models with known motion and deformation parameters were developed in this chapter in order to create a true gold standard to test and validate FT software packages. The models of increasing complexity were analysed with two commonly used software packages, CVI42 and Tomtec, and the outputs compared to the analytical values.

Overall, CVI42 generated the most realistic parameter curves but the values were inaccurate for the majority of parameters. Increasing the complexity of the model had little effect on the errors.

Undoubtedly, both short and long axes simulations did not represent realistic clinical

images: the images were generated with simple non-physiological contraction, and did not containe detailed anatomical structures. The lack of rotational motion clearly created problems. Based on the results, I would strongly recommend including a rotational motion when refining those models and adding more anatomical features..

Despite these limitations, simulation models remain useful and essential since they can report the exact values for the motion and deformation parameters, however, this chapter experimental results coupled with highlighted limitations, clearly indicate that the model complexity needs to be further improved and refined, taking into account the varying texture across the myocardial tissue, the surrounding cardiac chambers and additional imaging factors, such as acquired spatial and temporal resolutions and effects of noise on image tracking quality. Additionally, there was lack of complete description of in plane myocardial contraction in short-axis models. Thus, the circumferential motion needs to be added to short-axis models thus potentially improving the outcomes. Short and long axes models at different spatial and temporal resolutions could then be compared for optimisation of scanning parameters, then implemented *in vivo*.

Finally, only two commercial FT software packages were used in this chapter, however it is desirable to include more commercial and research analysis tools in this developmental and standardisation process. As with speckle tracking echocardiography, cardiovascular imaging societies and related organizations could help bring different vendors to provide information on algorithms used within their software (103), so researchers and clinicians can interpret their experimental results. FT software packages manufacturers should be encouraged to take an active role in the standardisation of FT methodology. This will help to reach a consensus on the best method of analysis, similarly to the standardisation processes actually carried out in echocardiographic studies. Standardising MRI acquisition parameters, in particular taking into account the spatial and temporal resolution, is also crucial and should be put into consideration if FT is to be accepted in

routine clinical practice.

Chapter 8: Conclusions and future work

The main focus of this thesis was to validate the use of feature tracking to derive global and regional deformation parameters to assess myocardial function. The technique has already shown promising results as an early predictor of several sub-clinical cardiovascular diseases (4)(5)(87).

The experimental work in this PhD thesis is a direct follow-up of the findings of the review chapter (chapter 3). To guide unfamiliar readers, the thesis includes a chapter that covers CMR imaging and provides some details on cardiac function and hypertension (chapter 2). In order to lighten the experimental chapters (chapter 5, 6 and 7), the common methodologies, including detailed information on the different software packages and statistics are including in chapter 4.

The remainder of this chapter resumes the key findings of the literature review and experimental chapters, discusses the limitations of this work, makes recommendations based on the results and suggest possible further research.

8.1 Summary of findings

This section summarises the key findings from the literature review and the three experimental chapters and discusses some of the limitations of the work carried out.

8.1.1 Literature review (Chapter 3)

The literature review chapter summarised all the studies, published until mid-2017, that used FT. Particular attention was paid to validation studies comparing FT to other techniques, CMR- tagging and echocardiographic speckle tracking, or models/numerical phantoms.

Previous studies have highlighted the potential effectiveness of FT in a clinical setting by

demonstrating the technique can discriminate between healthy heart state and some diseases (50)(51)(98). However, other researcher have highlighted the variability of FT and the differences in output when compared to echocardiography (67)(68). The main variabilities were found in regional deformation parameters compared to global measurement (6)(68), and when measuring radial strain parameters (30). Circumferential strain was the most reproducible parameter, followed by longitudinal strain (6)(67). This reported variability and the lack of absolute agreement between FT and established techniques (30)(67) remains an obstacle to its clinical use.

The chapter highlighted the key findings and limitations of all reviewed articles, however, no meta-analysis was carried out. This could have been useful to obtain normal values and cut-off points to discriminate between healthy populations and the studied pathologies. Nevertheless, the results clearly justified the work carried out in the following three experimental chapters.

8.1.2 Comparison between FT software (Chapter 5)

This chapter compared three FT software packages (Tomtec, CVI42 and CIM-FT) in a hypertensive population and a group of healthy subjects. Significant differences were found and few parameters were in agreement. For global measurements, software packages were only in agreement for the 2-chamber longitudinal strain.

ICC analysis demonstrated that global circumferential strain calculated from a mid-ventricle short axis slice and longitudinal strain were the most consistent parameters across software packages. Overall, global measurements displayed higher reproducibility than regional measurements for the three software. CVI42 was the software with the lowest inter- and intra- observer variability.

When interpreting the results of this chapter, readers should bear in mind that the analysis was carried out on a small sample size (28 size subjects and 26 hypertensive patients). Another confounding factor was the imaging protocol that was different for the healthy

subjects and the hypertensive patients. This may have accounted for a certain percentage of the variability and bias in this study. However, CVI42 was clearly more consistent and consequently was chosen to compare FT to CMR tagging.

8.1.3 Comparison between FT and Tagging (Chapter 6)

In this chapter, the most reproducible FT software from chapter 5 was compared to the established method of CMR tagging (8); CIMTag2D was used for the tagging analysis. Once more a group of healthy subjects and hypertensive patients were used but the hypertensive cohort was larger (n=62) and the imaging protocol identical for each group.

Significant differences between software were found in both groups and only a few parameters were in agreement. Those were global circumferential, global, endocardial and epicardial radial strain calculated from the mid-ventricle short axis slice and the endocardial radial strain calculated from the for 4-chamber view.

Significant differences were found between healthy males and females with both techniques; global and endocardial longitudinal strain from 4-chamber were significantly higher in female for both techniques, while the epicardial radial strain from 2-chamber was significantly higher in males for tagging only.

When comparing healthy subjects and hypertensive patients, CVI42 could not find any differences, however, global radial strain from the mid-ventricle short axis and 4-chamber global longitudinal strain rate were significantly higher in hypertensive patients using the tagging technique. When interpreting those results, it is worth keeping in mind that the two groups were heterogeneous in the term of size, age and gender.

8.1.4 Numerical simulations (Chapter 7)

Numerical simulations in the long and short axes, with increasing myocardial pattern complexity, were created and analysed with two FT software packages (Tomtec and CVI42). Both software struggled to analyse the models correctly, disagreeing between

them and with the analytical values for most parameters. Overall, CVI42 did produce realistic parameters curves (but with wrong values) while Tomtec mainly generated unrealistic asymmetric curves. None of the models used rotational motion and this might have strongly influenced the results as both software calculated non-zero circumferential parameters. Although, the introduction of more complex pattern helped reducing this issue for Tomtec but had no effect on the CVI42 results.

8.2 Implications of study and recommendations

8.2.1 Choice of software and strain parameters

More and more FT software are becoming available commercially or through research agreements. High variability between software has been clearly highlighted in this thesis and by previous authors, and consequently, until a gold standard is established to test the various software packages, it is hard to recommend one software based on accuracy. However, based on its better inter and intra-observer-variability and its more reasonable analysis of simulations, it might be preferable to use CVI42 if available.

Radial strain results showed the highest variability *in vivo* and until this is understood and fixed, it is preferable to avoid drawing clinical conclusions from them. The most consistent parameters across the three software by ICC agreement were mid-ventricle short axis circumferential strain and to a lesser extend longitudinal strain. It would therefore be advisable to privilege those parameters for analysis.

8.2.2 Standardization efforts

It is clear from the thesis and all published data, that efforts to standardise FT need to be undertaken. This process was carried out for 2D speckle tracking echocardiography with the European Association of Cardiovascular Imaging (EACVI) and the American Society

of Echocardiography (ASE) (70). A standardization task force was established with manufacturers to standardize deformation imaging parameters, providing definitions, abbreviations, formulas, and procedures for calculation of physical quantities derived from speckle tracking technology (70). The process involved the creation of synthetic ultrasound images for quality insurance process, and to compare global longitudinal strain in nine vendors (99). A related study, looked at global longitudinal strain in healthy subject with seven software (69). Following this work, guidelines were published in 2015 (85). It is obvious that the CMR community will need to come up with a similar plan for FT, involving societies and vendors. A reliable numerical phantom would play an essential role in this process.

8.3 Areas of further study

In a relatively new field avenues for further research are numerous and the suggestions in this section are far from exhaustive. They are however areas that could have been explored as the continuation of the work described in this thesis.

8.3.1 Normal values and cut-offs

There is an obvious lack of reliable normal range(s) and in the absence of standardization it might be interesting to establish them for the different software in healthy volunteers. The effect of imaging parameters could also be studied in a sub-set at the same time. This work could then be extended to different patient groups, thus leading to the establishment of cut-off values that could be used for diagnostic purposes.

Currently, there is a lack of data on segmental and torsion parameters in particular when comparing software. This would be of particular clinical relevance as those particular parameters appear to be valuable when looking at the presence of scar tissues (50)(51).

8.3.2 Improving numerical simulations

As demonstrated with speckle tracking (99), numerical phantoms will play a key role in the FT standardization process, it is therefore crucial to increase research efforts in this area. The results of chapter 7 demonstrate that it is essential to include rotational motion for the software to operate correctly. Consequently, this should be the first step in improving the models. Introducing more realistic anatomy and feature patterns would be the next step. This could be achieved by segmenting the relevant anatomical features from high resolution scans to create an initial image. Cine series would then be generated by deforming the first image using realistic values. Adding anatomical structure such as papillary muscles, right ventricle and the upper and lower insertion points would allow for segmental assessment.

Finally adding controllable parameters, in particular spatial and temporal resolutions, and noise level, would then help defining standard acquisition protocols.

References

1. Harrild DM, Han Y, Geva T, Zhou J, Marcus E, Powell AJ. Comparison of cardiac MRI tissue tracking and myocardial tagging for assessment of regional ventricular strain. Int J Cardiovasc Imaging. 2012;28(8):2009–18.
2. Onishi T, Saha SK, Ludwig DR, Onishi T, Marek JJ, Cavalcante JL, et al. Feature tracking measurement of dyssynchrony from cardiovascular magnetic resonance cine acquisitions: comparison with echocardiographic speckle tracking. J Cardiovasc Magn Reson. 2013;15:95.
3. Hor KN, Baumann R, Pedrizzetti G, Tonti G, Gottliebson WM, Taylor M, et al. Magnetic Resonance Derived Myocardial Strain Assessment Using Feature Tracking. J Vis Exp. 2011;(48):2356.
4. Kowallick JT, Kutty S, Edelmann F, Chiribiri A, Villa A, Steinmetz M, et al. Quantification of left atrial strain and strain rate using Cardiovascular Magnetic Resonance myocardial feature tracking: a feasibility study. J Cardiovasc Magn Reson. 2014/09/10. 2014;16(1):60.
5. Taylor RJ, Umar F, Moody WE, Meyyappan C, Stegemann B, Townend JN, et al. Feature-tracking cardiovascular magnetic resonance as a novel technique for the assessment of mechanical dyssynchrony. Int J Cardiol. 2014/05/24. 2014;175(1):120–5.
6. Morton G, Schuster A, Jogiya R, Kutty S, Beerbaum P, Nagel E. Inter-study reproducibility of cardiovascular magnetic resonance myocardial feature tracking. J Cardiovasc Magn Reson. 2012;14(1):43.
7. Schuster A, Kutty S, Padiyath A, Parish V, Gribben P, Danford DA, et al. Cardiovascular magnetic resonance myocardial feature tracking detects quantitative wall motion during dobutamine stress. J Cardiovasc Magn Reson.

2011;13:58.

8. Hor KN, Gottliebson WM, Carson C, Wash E, Cnota J, Fleck R. Comparison of Magnetic Resonance Feature Tracking for Strain Calculation With Harmonic Phase Imaging Analysis. JACC Cardiovasc Imaging. 2010;3.
9. Khanji MY. Clinical Effectiveness of Tailored E-coaching in Reducing Cardiovascular Risk Assessed Using Cardiovascular Imaging and Functional Assessment - A Primary Prevention Trial in Moderate to High Risk Individuals. Queen Mary University of London; 2017.
10. Biglands JD, Radjenovic A, Ridgway JP. Cardiovascular magnetic resonance physics for clinicians: part I. J Cardiovasc Magn Reson [Internet]. 2012;14(1):66. Available from: http://jcmr-online.biomedcentral.com/articles/10.1186/1532-429X-14-66
11. Biglands JD, Radjenovic A, Ridgway JP. Cardiovascular magnetic resonance physics for clinicians: part II. J Cardiovasc Magn Reson [Internet]. 2012;14(1):66. Available from: http://jcmr-online.biomedcentral.com/articles/10.1186/1532-429X-14-66
12. Biglands • John D, And • Aleksandra Radjenovic, Ridgway JP, editors. Cardiovascular MR Manual. 2nd ed. Springer International Publishing; 2015. 487 p.
13. Keith L. Moore AFD& AMRA. Clinically Oriented Anatomy. LWW, 2013;
14. Berkovitz HGSSEBKB. Gray's anatomy : the anatomical basis of clinical practice. New York: Elsevier Churchill Livingstone,; 2005.
15. Hurst J, Logue R, Schlant R, Wenger N. The Heart. 1974;83.
16. Heart Anatomy.
17. Cecie Starr, Christine Evers LS. Biology Today and Tomorrow with Physiology. 3rd ed. Cengage Learning, 2009;

18. Anatomy and Physiology II, Cardiac Cycle. Available from:https://courses.lumenlearning.com/ap2/chapter/cardiac-cycle/. :2–7.

19. Pokharel P, Bella J. Regression of left ventricular hypertrophy: Lessons from clinical trials. OA Evidence-Based Med [Internet]. 2013;1(2):1–8. Available from: http://www.oapublishinglondon.com/article/1110

20. Patricia M Kearney, Megan Whelton, Kristi Reynolds, Paul Muntner, Paul K Whelton, He J. Global burden of hypertension--analysis of worldwide data. Lancet. 2005;365:217–23.

21. Mayet J, Hughes A. PATHOPHYSIOLOGY IN HYPERTENSION. 2003;

22. Trenkwalder P, Hendricks P, Schoniger R, Rossberg J, Lydtin H, Hense HW, et al. Hypertension as a risk factor for cardiovascular morbidity and mortality in an elderly German population; the prospective STEPHY II study. Starnberg Study on Epidemiology of Parkinsonism and Hypertension in the Elderly. Eur Heart J [Internet]. 1999;20(23):1752–6. Available from: http://ovidsp.ovid.com/ovidweb.cgi?T=JS&PAGE=reference&D=emed4&NEWS=N&AN=1999407495%5Cnhttp://ovidsp.ovid.com/ovidweb.cgi?T=JS&PAGE=reference&D=med4&NEWS=N&AN=10562484

23. Williams H. Hypertension: Pathophysiology and diagnosis. Clin Pharm. 2015;7(1):11–4.

24. Gaasch WH. Left ventricular radius to wall thickness ratio. Am J Cardiol. 1979;43(6):1189–94.

25. Bogaet J, Al-Saadi N, Dymarkowski S, Taylor AM. Clinical Cardiac MRI. Springer Verlag, Berlin Heidelberg; 2005.

26. M. Christopher P. Cannon, Annemarie M. Armani M. Cardiovascular Magnetic Resonance Imaging. Contemporary Cardiology. Totowa, New Jersey: Humana Press Inc;

27. Ginat DT, Fong MW, Tuttle DJ, Hobbs SK, Vyas RC. Cardiac imaging: Part 1, MR pulse sequences, imaging planes, and basic anatomy. Am J Roentgenol. 2011;197(4):808–15.

28. Wahl A, Paetsch I, Gollesch A, Roethemeyer S, Foell D, Gebker R, et al. Safety and feasibility of high-dose dobutamine-atropine stress cardiovascular magnetic resonance for diagnosis of myocardial ischaemia: Experience in 1000 consecutive cases. Eur Heart J. 2004;25(14):1230–6.

29. Nagel E, Lehmkuhl HB, Bocksch W, Klein C, Vogel U, Frantz E, et al. Noninvasive diagnosis of ischemia-induced wall motion abnormalities with the use of high-dose dobutamine stress MRI: comparison with dobutamine stress echocardiography. Circulation [Internet]. 1999;99(6):763–70. Available from: http://www.ncbi.nlm.nih.gov/pubmed/9989961

30. Augustine D, Lewandowski AJ, Lazdam M, Rai A, Francis J, Myerson S, et al. Global and regional left ventricular myocardial deformation measures by magnetic resonance feature tracking in healthy volunteers: comparison with tagging and relevance of gender. J Cardiovasc Magn Reson. 2013;15:8.

31. van de Weijer T, van Ewijk PA, Zandbergen HR, Slenter JM, Kessels AG, Wildberger JE, et al. Geometrical models for cardiac MRI in rodents: comparison of quantification of left ventricular volumes and function by various geometrical models with a full-volume MRI data set in rodents. AJP Hear Circ Physiol [Internet]. 2012;302(3):H709–15. Available from: http://ajpheart.physiology.org/content/ajpheart/302/3/H709.full.pdf

32. Garcia MJ. Noninvasive cardiovascular imaging: a multimodality approach. Philadelphia: Wollters Kluwer/Lippincott Williams &Wilkins; 2010.

33. Chavhan GB, Babyn PS, Jankharia BG, Cheng H-LM, Shroff MM. Steady-State MR Imaging Sequences: Physics, Classification, and Clinical Applications.

RadioGraphics [Internet]. 2008;28(4):1147–60. Available from: http://pubs.rsna.org/doi/10.1148/rg.284075031

34. Haacke EM, Tkach JA. Fast MR imaging: techniques and clinical applications. AJR Am J Roentgenol [Internet]. 1990;155(5):951–64. Available from: http://www.ncbi.nlm.nih.gov/entrez/query.fcgi?cmd=Retrieve&db=PubMed&dopt=Citation&list_uids=2120964

35. Zerhouni EA, Parish DM, Rogers WJ, Yang A, Shapiro EP. Human heart: tagging with MR imaging--a method for noninvasive assessment of myocardial motion. Radiology [Internet]. 1988;169(1):59–63. Available from: http://pubs.rsna.org/doi/10.1148/radiology.169.1.3420283

36. Axel L, Dougherty L. MR imaging of motion with spatial modulation of magnetization. Radiology [Internet]. 1989;171(3):841–5. Available from: http://www.pubmedcentral.nih.gov/articlerender.fcgi?artid=2490799&tool=pmcentrez&rendertype=abstract

37. Ibrahim E-SH. Myocardial tagging by Cardiovascular Magnetic Resonance: evolution of techniques--pulse sequences, analysis algorithms, and applications. J Cardiovasc Magn Reson [Internet]. 2011;13(1):36. Available from: http://jcmr-online.biomedcentral.com/articles/10.1186/1532-429X-13-36

38. Schuster A, Hor KN, Kowallick JT, Beerbaum P, Kutty S. Cardiovascular Magnetic Resonance Myocardial Feature Tracking: Concepts and Clinical Applications. Circ Cardiovasc Imaging. 2016;9(4):1–10.

39. Pedrizzetti G, Claus P, Kilner PJ, Nagel E. Principles of cardiovascular magnetic resonance feature tracking and echocardiographic speckle tracking for informed clinical use. J Cardiovasc Magn Reson. 2016;18(1):51.

40. Rahman ZU, Sethi P, Murtaza G, Virk HUH, Rai A, Mahmod M, et al. Feature tracking cardiac magnetic resonance imaging: A review of a novel non-invasive

cardiac imaging technique. World J Cardiol [Internet]. 2017;9(4):312. Available from: http://www.wjgnet.com/1949-8462/full/v9/i4/312.htm

41. Fischer SE, McKinnon GC, Maier SE, Boesiger P. Improved myocardial tagging contrast. Magn Reson Med. 1993/08/01. 1993;30(2):191–200.

42. Osman NF, Kerwin WS, McVeigh ER, Prince JL. Cardiac motion tracking using CINE harmonic phase (HARP) magnetic resonance imaging. Magn Reson Med. 1999;42.

43. Kraitchman DL, Young AA, Chang CN, Axel L. Semi-automatic tracking of myocardial motion in MR tagged images. IEEE Trans Med Imaging. 1995;14.

44. Lorca MCN, Haraldsson H, Ordovas KG. Ventricular Mechanics. Magn Reson Imaging Clin. 23(1):7–13.

45. Moody WE, Taylor RJ, Edwards NC, Chue CD, Umar F, Taylor TJ, et al. Comparison of magnetic resonance feature tracking for systolic and diastolic strain and strain rate calculation with spatial modulation of magnetization imaging analysis. J Magn Reson Imaging. 2014/03/29. 2015;41(4):1000–12.

46. Axel L, Dougherty L. MR imaging of motion with spatial modulation of magnetization. Radiology. 1989;171.

47. Mosher TJ, Smith MB. A DANTE tagging sequence for the evaluation of translational sample motion. Magn Reson Med. 1990;15.

48. Young AA, Axel L, Dougherty LKBD, Parenteau C. Validation of tagging with MR imaging to estimate material deformation. Radiology. 1993;188.

49. Edvardsen T, Gerber BL, Garot J, Bluemke DA, Lima JA, Smiseth OA. Quantitative assessment of intrinsic regional myocardial deformation by Doppler strain rate echocardiography in humans: validation against three-dimensional tagged magnetic resonance imaging. Circulation. 2002/07/03. 2002;106(1):50–6.

50. Maret E, Todt T, Brudin L, Nylander E, Swahn E, Ohlsson JL, et al. Functional

measurements based on feature tracking of cine magnetic resonance images identify left ventricular segments with myocardial scar. Cardiovasc Ultrasound. 2009;7:53.

51. Schuster A, Paul M, Bettencourt N, Morton G, Chiribiri A, Ishida M, et al. Cardiovascular magnetic resonance myocardial feature tracking for quantitative viability assessment in ischemic cardiomyopathy. Int J Cardiol. 2013;166(2):413–20.

52. Abraham TP, Dimaano VL, Liang HY. Role of tissue Doppler and strain echocardiography in current clinical practice. Circulation. 2007/11/28. 2007;116(22):2597–609.

53. Dandel M, Lehmkuhl H, Knosalla C, Suramelashvili N, Hetzer R. Strain and Strain Rate Imaging by Echocardiography - Basic Concepts and Clinical Applicability. Curr Cardiol Rev [Internet]. 2009;5(2):133–48. Available from: http://www.eurekaselect.com/openurl/content.php?genre=article&issn=1573-403X&volume=5&issue=2&spage=133

54. Blessberger H, Binder T. Two dimensional speckle tracking echocardiography: basic principles. Heart [Internet]. 2010;96(9):716–22. Available from: http://heart.bmj.com/cgi/doi/10.1136/hrt.2007.141002

55. Kutty S, Rangamani S, Venkataraman J, Li L, Schuster A, Fletcher SE, et al. Reduced global longitudinal and radial strain with normal left ventricular ejection fraction late after effective repair of aortic coarctation: a CMR feature tracking study. Int J Cardiovasc Imaging. 2013;29(1):141–50.

56. Almutairi HM, Zemrak F, Treibel TA, Sado D, Boubertakh R, Miquel ME, et al. A comparison of cardiac motion analysis software packages: application to left ventricular deformation analysis in hypertensive patients. J Cardiovasc Magn Reson. 2015;17(1):P57.

57. Lossnitzer D, Bellsham-Revell H, Bell A, Schuster A, Hussain T, Botnar RM, et al. Speckle tracking for cardiac MRI in patients pre and post dilation and stent implantation of aortic coarctation. J Cardiovasc Magn Reson. 2012;14(Suppl 1):P125.

58. Swoboda PP, Larghat A, Zaman A, Fairbairn TA, Motwani M, Greenwood JP, et al. Reproducibility of myocardial strain and left ventricular twist measured using complementary spatial modulation of magnetization. J Magn Reson Imaging. 2013/09/06. 2014;39(4):887–94.

59. Donal E, Mascle S, Brunet A, Thebault C, Corbineau H, Laurent M, et al. Prediction of left ventricular ejection fraction 6 months after surgical correction of organic mitral regurgitation: the value of exercise echocardiography and deformation imaging. Eur Heart J Cardiovasc Imaging. 2012;13(11):922–30.

60. Shehata ML, Cheng S, Osman NF, Bluemke DA, Lima JA. Myocardial tissue tagging with cardiovascular magnetic resonance. In: J Cardiovasc Magn Reson. 2009.

61. Wu L, Germans T, Guclu A, Heymans MW, Allaart CP, van Rossum AC. Feature tracking compared with tissue tagging measurements of segmental strain by cardiovascular magnetic resonance. J Cardiovasc Magn Reson. 2014/01/24. 2014;16:10.

62. Singh A, Steadman CD, Khan JN, Horsfield MA, Bekele S, Nazir SA, et al. Intertechnique agreement and interstudy reproducibility of strain and diastolic strain rate at 1.5 and 3 tesla: A comparison of feature-tracking and tagging in patients with aortic stenosis. J Magn Reson Imaging. 2015;41(4):1129–37.

63. Petitjean C, Rougon N, Cluzel P. Assessment of myocardial function: a review of quantification methods and results using tagged MRI. J Cardiovasc Magn Reson. 2005;7.

64. Moore CC, Lugo-Olivieri CH, McVeigh ER, Zerhouni EA. Three-dimensional systolic strain patterns in the normal human left ventricle: characterization with tagged MR imaging. Radiology. 2000;214.

65. Amundsen BH, Helle-Valle T, Edvardsen T, Torp H, Crosby J, Lyseggen E. Noninvasive myocardial strain measurement by speckle tracking echocardiography: Validation against sonomicrometry and tagged magnetic resonance imaging. J Am Coll Cardiol. 2006;47.

66. Orwat S, Kempny A, Diller GP, Bauerschmitz P, Bunck Ac, Maintz D, et al. Cardiac magnetic resonance feature tracking: a novel method to assess myocardial strain. Comparison with echocardiographic speckle tracking in healthy volunteers and in patients with left ventricular hypertrophy. Kardiol Pol. 2014;72(4):363–71.

67. Padiyath A, Gribben P, Abraham JR, Li L, Rangamani S, Schuster A, et al. Echocardiography and cardiac magnetic resonance-based feature tracking in the assessment of myocardial mechanics in tetralogy of Fallot: an intermodality comparison. Echocardiography. 2013;30(2):203–10.

68. Kempny A, Fernandez-Jimenez R, Orwat S, Schuler P, Bunck AC, Maintz D, et al. Quantification of biventricular myocardial function using cardiac magnetic resonance feature tracking, endocardial border delineation and echocardiographic speckle tracking in patients with repaired tetralogy of fallot and healthy controls. J Cardiovasc Magn Reson. 2012;14.

69. Farsalinos KE, Daraban AM, Ünlü S, Thomas JD, Badano LP, Voigt JU. Head-to-Head Comparison of Global Longitudinal Strain Measurements among Nine Different Vendors. J Am Soc Echocardiogr. 2015;28.

70. Voigt JU, Pedrizzetti G, Lysyansky P, Marwick TH, Houle H, Baumann R. Definitions for a common standard for 2D speckle tracking echocardiography: consensus document of the EACVI/ASE/Industry Task Force to standardize

deformation imaging. Eur Hear J Cardiovasc Imaging. 2015;16.

71. Kramer CM, Barkhausen J, Flamm SD, Kim RJ, Nagel E. Standardized cardiovascular magnetic resonance (CMR) protocols 2013 update. J Cardiovasc Magn Reson. 2013;15(1):1–10.

72. Claus P, Omar AMS, Pedrizzetti G, Sengupta PP, Nagel E. Tissue Tracking Technology for Assessing Cardiac MechanicsPrinciples, Normal Values, and Clinical Applications. JACC Cardiovasc Imaging. 2015;8.

73. Schuster A, Stahnke VC, Unterberg-Buchwald C, Kowallick JT, Lamata P, Steinmetz M, et al. Cardiovascular magnetic resonance feature-tracking assessment of myocardial mechanics: Intervendor agreement and considerations regarding reproducibility. Clin Radiol [Internet]. 2015;70(9):989–98. Available from: http://dx.doi.org/10.1016/j.crad.2015.05.006

74. Statistics M. A Comparison of Alternative Tests of Significance for the Problem of m Rankings Author (s): Milton Friedman Source : The Annals of Mathematical Statistics , Vol . 11 , No . 1 (Mar ., 1940), pp . 86-92 Published by : Institute of Mathematical Statistic. 2017;11(1):86–92.

75. Armstrong RA. When to use the Bonferroni correction. 2014;34:502–8.

76. Martin Bland J, Altman D. STATISTICAL METHODS FOR ASSESSING AGREEMENT BETWEEN TWO METHODS OF CLINICAL MEASUREMENT. Lancet. 2017 May;327(8476):307–10.

77. Shrout PE, Fleiss JL. Intraclass Correlations : Uses in Assessing Rater Reliability. 1979;86(2):420–8.

78. Dunk NM, Lalonde J, Callaghan JP. I MPLICATIONS FOR THE U SE OF P OSTURAL A NALYSIS AS A. (Cv):386–92.

79. Ibrahim E-SH. Heart Mechanics: Magnetic Resonance Imaging, Mathematical Modeling, Pluse Sequences, and Image Analysis. New York; 2017. 366-367 p.

80. Ahmed MI, Desai R V., Gaddam KK, Venkatesh BA, Agarwal S, Inusah S, et al. Relation of torsion and myocardial strains to LV ejection fraction in hypertension. JACC Cardiovasc Imaging [Internet]. 2012;5(3):273–81. Available from: http://dx.doi.org/10.1016/j.jcmg.2011.11.013

81. Mizuguchi Y, Oishi Y, Miyoshi H, Iuchi A, Nagase N, Oki T. Concentric left ventricular hypertrophy brings deterioration of systolic longitudinal, circumferential, and radial myocardial deformation in hypertensive patients with preserved left ventricular pump function. J Cardiol. 2010;55(1):23–33.

82. Koulouris SN, Kostopoulos KG, Triantafyllou K a, Karabinos I, Bouki TP, Karvounis HI, et al. Impaired systolic dysfunction of left ventricular longitudinal fibers: a sign of early hypertensive cardiomyopathy. Clin Cardiol [Internet]. 2005;28(6):282–6. Available from: http://www.ncbi.nlm.nih.gov/pubmed/16028462

83. Bourfiss M, Vigneault DM, Ghasebeh MA, Murray B, James CA, Tichnell C, et al. Feature tracking CMR reveals abnormal strain in preclinical arrhythmogenic right ventricular dysplasia / cardiomyopathy : a multisoftware feasibility and clinical implementation study. 2017;1–13.

84. Nagata Y, Takeuchi M, Mizukoshi K, Wu VC. LEFT VENTRICULAR STRAIN MECHANICS : REPRODUCIBILITY Intervendor Variability of Two-Dimensional Strain Using Vendor-Specific and Vendor-Independent Software.

85. Lang RM, Badano LP, Mor-Avi V, Afilalo J, Armstrong A, Ernande L. Recommendations for cardiac chamber quantification by echocardiography in adults: an update from the American Society of Echocardiography and the European Association of Cardiovascular Imaging. J Am Soc Echocardiogr. 2015;28.

86. Shehata ML, Cheng S, Osman NF, Bluemke DA, Lima JA. Myocardial tissue

tagging with cardiovascular magnetic resonance. J Cardiovasc Magn Reson [Internet]. 2009;11(1):55. Available from: http://jcmr-online.biomedcentral.com/articles/10.1186/1532-429X-11-55

87. Hor KN, Gottliebson WM, Carson C, Wash E, Cnota J, Fleck R, et al. Comparison of magnetic resonance feature tracking for strain calculation with harmonic phase imaging analysis. JACC Cardiovasc Imaging. 2010;3(2):144–51.

88. Kempny A, Fernández-Jiménez R, Orwat S, Schuler P, Bunck AC, Maintz D, et al. Quantification of biventricular myocardial function using cardiac magnetic resonance feature tracking, endocardial border delineation and echocardiographic speckle tracking in patients with repaired tetralogy of fallot and healthy controls. J Cardiovasc Magn Reson [Internet]. 2012;14(1):32. Available from: http://jcmr-online.biomedcentral.com/articles/10.1186/1532-429X-14-32

89. Wold S, Esbensen K, Geladi P. Principal component analysis. Chemom Intell Lab Syst. 1987;2(1):37–52.

90. Hanley AJ, McNeil JB. The Meaning and Use of the Area under a Receiver Operating Characteristic (ROC) Curve. Radiology [Internet]. 1982;143:29–36. Available from: http://radiology.rsna.org/content/143/1/29.full.pdf

91. Andre F, Steen H, Matheis P, Westkott M, Breuninger K, Sander Y, et al. Age- and gender-related normal left ventricular deformation assessed by cardiovascular magnetic resonance feature tracking. J Cardiovasc Magn Reson [Internet]. 2015;17(1):25. Available from: http://jcmr-online.com/content/17/1/25

92. Kleijn SA, Pandian NG, Thomas JD, De Isla LP, Kamp O, Zuber M, et al. Normal reference values of left ventricular strain using three-dimensional speckle tracking echocardiography: Results from amulticentre study. Eur Heart J Cardiovasc Imaging. 2015;16(4):410–6.

93. Yingchoncharoen T, Agarwal S, Popovic ZB, Marwick TH. Normal ranges of left

ventricular strain: a meta-analysis. J Am Soc Echocardiogr. 2013;26(2):185–91.

94. Smiseth OA, Torp H, Opdahl A, Haugaa KH, Urheim S. Myocardial strain imaging: How useful is it in clinical decision making? Eur Heart J. 2016;37(15):1196–1207b.

95. Szymanski C, Lévy F, Tribouilloy C. Should LVEF be replaced by global longitudinal strain ? 2014;100(21):2013–5.

96. Kansal MM, Mansour IN, Ismail S, Bress A, Wu G, Mirza O, et al. Left ventricular global longitudinal strain predicts mortality and heart failure admissions in African American patients. Clin Cardiol. 2017;40(5):314–21.

97. Rhea IB, Rehman S, Jarori U, Choudhry MW, Feigenbaum H, Sawada SG. Prognostic utility of blood pressure-adjusted global and basal systolic longitudinal strain. Echo Res Pract [Internet]. 2016;3(1):17–24. Available from: http://www.echorespract.com/lookup/doi/10.1530/ERP-15-0037

98. Bratis K, Hackmann P, Child N, Mavrogeni S, Krasemann T, Hussain T, et al. CMR feature tracking in Kawasaki Disease convalescence. J Cardiovasc Magn Reson. 2015;17(Suppl 1):1–2.

99. D'hooge J, Barbosa D, Gao H, Claus P, Prater D, Hamilton J, et al. Two-dimensional speckle tracking echocardiography: Standardization efforts based on synthetic ultrasound data. Eur Heart J Cardiovasc Imaging. 2016;17(6):693–701.

100. Moore CC, McVeigh ER, Zerhouni EA. Quantitative tagged magnetic resonance imaging of the normal human left ventricle. Top Magn Reson Imaging [Internet]. 2000;11(6):359–71. Available from: http://www.pubmedcentral.nih.gov/articlerender.fcgi?artid=2396311&tool=pmcentrez&rendertype=abstract

101. Moriasi DN, Arnold JG, Liew MW Van, Bingner RL, Harmel RD, Veith TL. M e g s q a w s. 2007;50(3):885–900.

102. D. N. Moriasi, J. G. Arnold, M. W. Van Liew, R. L. Bingner, R. D. Harmel, T. L. Veith. Model Evaluation Guidelines for Systematic Quantification of Accuracy in Watershed Simulations. Trans ASABE [Internet]. 2007;50(3):885–900. Available from: http://elibrary.asabe.org/abstract.asp??JID=3&AID=23153&CID=t2007&v=50&i=3&T=1

103. Voigt JU, Pedrizzetti G, Lysyansky P, Marwick TH, Houle H, Baumann R, et al. Definitions for a common standard for 2D speckle tracking echocardiography: consensus document of the EACVI/ASE/Industry Task Force to standardize deformation imaging. Eur Hear J Cardiovasc Imaging. 2014/12/20. 2015;16(1):1–11.